Analysis and Mitigation of the Effect of Magnetic Field Inhomogeneities and Undersampling Artifacts on Magnetic Resonance Fingerprinting

Der Naturwissenschaftlichen Fakultät
der Friedrich-Alexander-Universität
Erlangen-Nürnberg

zur

Erlangung des Doktorgrades Dr. rer. nat.

Vorgelegt von
Gregor Körzdörfer

Als Dissertation genehmigt von der Naturwissenschaftlichen Fakultät der Friedrich-Alexander-Universität Erlangen-Nürnberg

Tag der mündlichen Prüfung: 27.05.2020

Vorsitzende/r des Promotionsorgans: Prof. Dr. Georg Kreimer

Gutachter/in: Prof. Dr. Bernhard Hensel
Prof. Dr. Jürgen Reichenbach

Abstract

Magnetic resonance imaging (MRI) is largely limited to producing qualitative contrast images instead of quantitative maps of tissue characteristics. A novel framework for quantitative MRI termed Magnetic Resonance Fingerprinting (MRF) to map tissue parameters such as the relaxation times T_1 and T_2 has recently been introduced. In MRF, tissue signals are generated by applying a pseudo-randomly varying MRI acquisition, acquired using highly undersampled trajectories and matched to a database of simulated tissue signals. The aim of this thesis is to investigate hypotheses underlying MRF regarding its susceptibility to undersampling artifacts and magnetic field inhomogeneities and develop countermeasures. Since MRF can be implemented in various ways, one of the most popular implementations based on the FISP (Fast Imaging with Steady State Precession) sequence was chosen for analysis and as a basis for further developments.
The single shot spiral trajectories employed lead to substantial undersampling artifacts. In this work, the temporal variation of the spiral sampling patterns was examined and optimized. The results show that the originally proposed temporal order yields artifacts of similar frequencies as the signal responses from tissues, which leads to spatially dependent misestimations of parameters. To resolve those, an optimized temporal order was developed in simulations and proven in in-vivo experiments. The following chapter is dedicated to the influence of magnetic field inhomogeneities on MRF. Here it is shown that different local amplitudes of the radio frequency (RF) field B_1^+ can lead to misestimations of parameters by up to 50%, which can be resolved by measuring a B_1^+ map and integrating the information in the pattern match. Another newly developed strategy in this work is to mitigate the influence of B_1^+ by the introduction of acquisition segments that are particularly sensitive to B_1^+. Two approaches were developed and evaluated, one including FLASH (Fast Low-Angle Shot) and one using two 90° phase shifted pulses. Here, tissue parameter maps and B_1^+ maps were simultaneously generated, thereby resolving interdependencies. Furthermore, in this work it was found that the static magnetic field B_0 can also have an impact on FISP-MRF. The dependency was analyzed and related to the relative phase difference between spin ensembles and RF pulses. A technique to mitigate the dependency by additionally dephasing spins before RF pulses was developed. The chapter is concluded with the presentation of the novel development of MRFF (Magnetic Resonance Field Fingerprinting). By replacing some FISP segments with TrueFISP and FLASH segments, B_0 and B_1^+ dependent information was added, which enabled the simultaneous generation of T_1, T_2, B_0, B_1^+ and intravoxel phase dispersion maps. In the last chapter, the in-vivo reproducibility of FISP-MRF with the newly developed improvements described in the previous chapters was evaluated by scanning ten volunteers on ten scanners. T_1 and T_2 values varied less than 8.0% in brain compartments across scanners.

Zusammenfassung

Die Magnetresonanztomographie (MRT) beschränkt sich weitgehend auf die Erzeugung qualitativer Kontrastbilder anstelle von quantitativen Karten von Gewebeeigenschaften. Kürzlich wurde ein neuartiges Framework für quantitative MRT, Magnetic Resonance Fingerprinting (MRF) zur direkten Abbildung von Gewebeparametern wie der Relaxationszeiten T_1 und T_2 präsentiert. Bei MRF werden Gewebesignale mittels einer pseudozufällig variierenden MRT-Sequenz generiert, die unter Verwendung stark unterabgetasteter Trajektorien aufgenommen werden und daraufhin mit einer Datenbank simulierter Gewebesignale zum Zweck der Identifikation von Gewebeparametern verglichen werden. Ziel dieser Arbeit ist es, die Anfälligkeit von MRF für Unterabtastungsartefakte und Magnetfeldinhomogenitäten zu untersuchen und entsprechende Gegenmaßnahmen zu entwickeln. Da MRF auf verschiedene Arten implementiert werden kann, wurde die bis dato am häufigsten verwendete Implementierung basierend auf der FISP (Fast Imaging with Steady State Precession) Sequenz zur Analyse und als Grundlage für weitere Entwicklungen ausgewählt.
Die in FISP-MRF verwendeten Einzelschuss-Spiraltrajektorien führen zu erheblichen Unterabtastungsartefakten im Bildraum. In dieser Arbeit wird deren zeitliche Variation untersucht und optimiert. Die Resultate zeigen, dass die ursprünglich vorgeschlagene Abfolge Artefakte mit ähnlichen Frequenzen wie die der Signalantworten von Geweben ergibt, was zu ortsabhängigen Parameterfehlern führt. Eine optimierte Abfolge wurde in Simulationen gefunden, die in in-vivo Experimenten bestätigt wurde. Das folgende Kapitel befasst sich mit dem Einfluss von Magnetfeldinhomogenitäten auf FISP-MRF. Hier wird gezeigt, dass variierende lokale Amplituden des HF-Feldes B_1^+ zu Parameterfehlern von bis zu 50% führen können, die sich durch die Messung einer B_1^+ Karte und Integrieren der Informationen in den Musterabgleich beheben lassen können. Eine weitere in dieser Arbeit entwickelte Strategie ist die Einführung von Akquisitionssegmenten, die gegenüber B_1^+ besonders sensitiv sind. Zwei Ansätze, einer mit FLASH (Fast Low-Angle Shot) und einer mit zwei um 90° phasenverschobenen Hochfrequenz-Pulsen pro TR wurden in dieser Arbeit entwickelt. Hier werden gleichzeitig Gewebeparameter- und B_1^+-Karten erzeugt, wodurch gegenseitige Abhängigkeiten aufgelöst werden. In dieser Arbeit wurde auch gezeigt, dass Inhomogenitäten des statischen Magnetfelds B_0 sich auf FISP-MRF auswirken können. Diese Abhängigkeit wurde analysiert und mit der relativen Phasendifferenz zwischen Spin-Ensembles und HF-Pulsen in Beziehung gesetzt. Wie in dieser Arbeit gezeigt, kann durch zusätzliches Dephasieren von Spin-Ensembles vor einem HF-Impuls der Einfluss von B_0 stark vermindert werden. Im letzten Abschnitt dieses Kapitels wird die neue eigene Entwicklung MRFF (Magnetic Resonance Field Fingerprinting) präsentiert. Durch Ersetzen einiger FISP-Segmente durch TrueFISP- und FLASH-Segmente werden B_0 und B_1^+ abhängige Informationen hinzugefügt,

wodurch die gleichzeitige Erzeugung von T_1, T_2, B_0, B_1^+ sowie Suszeptibilitätskarten möglich wird. Im fünften Kapitel wurde die in-vivo Reproduzierbarkeit und Wiederholbarkeit von FISP-MRF mit den in den vorhergehenden Kapiteln beschriebenen Verbesserungen durch Messungen von zehn Probanden auf insgesamt zehn Scannern evaluiert. Die T_1- und T_2-Werte variierten zwischen den Scannern in den Gehirnkompartimenten um weniger als 8,0%.

CONTENTS

1. INTRODUCTION

Advances in the ability to describe physical phenomena have aided the development of medicine since the earliest times. Around 400 BC for example, Hippocrates described a method for measurement of body temperature by observing the drying of an earth-soaked cloth covering a person's thorax [Ots97]. A rather recent example is the medical science radiology that was initiated by a finding in the field of physics, the discovery of X-Rays in 1895 by Wilhelm Conrad Röntgen [RÖN96]. Radiology uses non-invasive imaging to study the inside of living organisms. Besides imaging using X-rays, another major sub-specialty of radiology is Magnetic Resonance Imaging (MRI). Similarly to X-Rays, MRI is also based on a physical phenomenon, nuclear magnetic resonance (NMR). It was discovered by Isidor Isaac Rabi who first measured magnetic properties of atomic nuclei in 1938 [Rab38]. The method was separately extended by Felix Bloch [Blo46] and Edward Mills Purcell [Pur46] to magnetic resonance spectroscopy in the 1940s. Their method enabled the measurement of a specimen's NMR spectrum. Later on, Paul Lauterbur [Lau73] and Peter Mansfield [Man73] further developed the method to acquire spatially resolved images. The technique was quickly applied in living organisms and to date it is indispensable in modern medicine. MRI has several advantages over other imaging modalities. Firstly, MRI is capable of producing images with good soft tissue contrast at submillimeter resolution. Secondly, non-ionizing radiation is utilized which minimizes potential harm to an organism being examined.

Nuclear spins exhibit different behavior with respect to their surroundings which can be utilized to distinguish tissues through the application of magnetic fields. Nuclear spins align with the direction of a strong static external magnetic field and precess with high frequency around its axis. When applying another magnetic field with the same frequency as the nuclear spins, the spins are tipped and the current that the precessing nuclear spins induce in a coil can be measured. Several techniques how to apply magnetic fields to generate images that reflect the distribution of nuclear spins have been developed. Not only the distribution and density can be translated into images, but also specific decay rates of the generated magnetization which is caused by the precessing nuclear spins can be used as a contrast mechanism. Those decay rates are called relaxation times T_1 and T_2 and differ from tissue to tissue. In today's clinical routine, images with contrasts that reflect different relaxation times in tissues are standard. These images show morphological

structures where pathological tissue can be described as hyper- or hypointense compared to normal appearing tissue. It should be noted that due to the high proportion of hydrogen in human tissue, it is commonly used in clinical MRI and in this work, although other other elements like phosphor or fluorine can also be used. With MRI, other tissue dependent information such as diffusion, perfusion or susceptibility can be translated into images. However, most MR images only indirectly visualize quantitative information, and are therefore called weighted images. Diagnosis in routine MRI is mostly based on this morphological and relative intensity information which makes the reports subjective and pathologies that alter tissue characteristics on a global or diffuse scale may be missed [Pie10]. These shortcomings could be overcome by directly measuring tissue parameters quantitatively. Concrete clinical questions where quantitative MRI could help are e.g. identifying physiologic changes in liver [Pan18] and cardiac fibrosis [HC17] that might remain undetected by qualitative MRI. More specific information for characterizing pathologies such as multiple sclerosis [Mac09] or brain tumors [Bad17] can be provided with quantitative MRI. Furthermore, it can be used to assess the response to treatment [Liu16] and in cases where no internal referencing can be performed such as in hippocampal sclerosis [Lia18]. Diseases can be detected before gross morphological alterations occur that would be detectable with qualitative MRI e.g. in cartilage [Rec98] and repair processes can be monitored [Wel08].
Several techniques to directly measure tissue parameters in MRI have been proposed over time, but no truly quantitative method has found widespread clinical application. This is due to a variety of reasons, including the long measurement time of such techniques and their rather poor precision [Mar12]. One would also assume that ground truth values for relaxation times in healthy tissues of a homogeneous population would exist. However when looking at published values acquired with different techniques, differences by more than a factor of two can be found [Boj17].
Magnetic Resonance Fingerprinting (MRF) [Ma13] tries to overcome the limitations of current quantitative MR methods. MRF is a framework that generates unique signal responses from different tissues by strongly varying MRI acquisition parameters during the acquisition. Those signals - called fingerprints - are compared to a set of signals with known parameters - a dictionary - which is normally created by simulating the MR signal. Through the comparison process of the measured fingerprints in all imaged voxels with the dictionary, parameter maps are generated. The signals can be acquired in a very fast manner, by collecting only varying portions of image information at every time point throughout the acquisition. One major hypothesis underlying MRF is that the comparison process of the signals is not influenced by the high level of artifacts that are caused by acquiring too little image information at every time point. Many different variants of MRF have been published that quantify relaxation parameters and other parameters

influencing MRI experiments. In this work, one of the most frequently used MRF implementations - FISP-MRF [Jia15] - that measures T_1 and T_2 relaxation times is investigated.
Chapter two of this thesis presents an overview about MRI and techniques for quantitative MRI. In chapter three, the influence of undersampling artifacts on FISP-MRF is investigated. Since FISP-MRF uses a spiral sampling pattern that is rotated at each time point, artifact patterns can be altered by varying the temporal order of the spiral sampling patterns. The originally proposed temporal ordering was tested in numerical simulations and experiments. To mitigate potential influences of undersampling artifacts, the temporal ordering was then optimized and successfully applied in experiments. Chapter four is dedicated to the influence of magnetic field inhomogeneneities on FISP-MRF. The dependency of parameter estimations from FISP-MRF to inhomogeneities of the static magnetic field B_0 and the radiofrequency transmit field B_1^+ was analyzed. Methods were developed that include B_0 and B_1^+ in the signal model and subsequently in the dictionary. For B_1^+, a technique that relies on an additional measurement of a B_1^+ map which can be used to constrain the search space in the dictionary in B_1^+ dimension for FISP-MRF was developed. Another strategy that was employed in this thesis is to desensitize the signals to inhomogeneities of B_0. In contrast to that, methods were developed in this thesis that deliberately make the signals sensitive to B_0 and B_1^+ and map these parameters simultaneously with T_1 and T_2. In chapter five, a study that was performed to estimate the repeatability and reproducibility of a FISP-MRF implementation based on several improvements found in the preceding chapters is presented. Ten volunteers' brains were scanned on ten scanners at different sites and the deviation of parameter values in different brain regions were calculated. In the sixth chapter the main results and findings in this work are briefly summarized and potential directions for further developments of MRF are outlined.

2. BASICS

This chapter summarizes the basics of nuclear magnetic resonance (NMR) and magnetic resonance imaging (MRI). It aims to provide a brief overview about the fundamental discoveries and descriptions of nuclear spin effects in the last 100 years. All its content is taken from books [Bro14, Sli79, Ber04, Dem05b, Vla03, Dem05a] if no explicit other citation is given.

2.1 Nuclear Magnetic Resonance

Nuclei in a strong constant magnetic field can be perturbed by weak oscillating magnetic fields and thereby produce electromagnetic signals. This phenomenon is called nuclear magnetic resonance (NMR). In the following section a brief summary and description of the effect is provided. It begins with the Stern-Gerlach experiment in which the existence of a quantized intrinsic angular momentum of particles was discovered and is followed by a brief quantum mechanical and semiclassical description of NMR.

2.1.1 Quantum Mechanical Description

It was experimentally observed that the path of neutral silver atoms passing through a perpendicular oriented magnetic field is split up in two pathways (Stern-Gerlach experiment). It was concluded, that a force F is exerted on an atom passing through the inhomogeneous magnetic field $\boldsymbol{B} = (0, 0, B_z)$. An explanation for this experimental finding is the existence of a quantized magnetic moment $\boldsymbol{\mu}$ of the atoms. The force F is described by:

$$F = \boldsymbol{\nabla}(\boldsymbol{\mu} \cdot \boldsymbol{B}) = \mu_z \frac{\partial B_z}{\partial z} = \mu_z G_z. \tag{2.1}$$

The orbital angular moment of the ground state of the silver atoms used in this experiment is zero. Therefore, the magnetic moment must be arising from an intrinsic magnetic moment of its one electron in the valence shell. The magnetic moments of the other electrons compensate to zero. The electron's intrinsic magnetic moment is called spin $\boldsymbol{S}$ and related to its magnetic moment via a gyromagnetic ratio γ:

$$\boldsymbol{\mu} = \gamma \cdot \boldsymbol{S}. \tag{2.2}$$

When assuming that the spin suffices the angular momentum rules in quantum mechanics its magnitude is

$$\boldsymbol{S}^2 = s(s+1)\hbar^2 \tag{2.3}$$

with the spin quantum number $s = \frac{n}{2}$ (with n any non-negative integer). Projected onto an arbitrary axis z the spin z-projection is

$$S_z = m_s\hbar \tag{2.4}$$

with m_s element of -s, -s+1,..., +s. Since two different pathways of neutral silver atoms were found in the above mentioned experiment it could be concluded that the spin quantum number of the electron is $\frac{1}{2}$ and possible configurations are $m_s \pm \frac{1}{2}$.

Nuclear Spin

Similarly, atomic nuclei have a nuclear spin $\boldsymbol{I}$ that consists of the sum of the spins $\boldsymbol{S}_i$ and angular orbital momentums $\boldsymbol{L}_i$ of the nucleons:

$$\boldsymbol{I} = \sum_i (\boldsymbol{S}_i + \boldsymbol{L}_i). \tag{2.5}$$

The nuclear spin quantum number I is linked to the nuclear spin $\boldsymbol{I}$ as follows:

$$\boldsymbol{I} = I(I+1)\hbar^2. \tag{2.6}$$

The magnetic moment $\boldsymbol{\mu}_l$ of a nucleus is linked to the nuclear spin $\boldsymbol{I}$ via the gyromagnetic ratio γ:

$$\gamma = \frac{|\boldsymbol{\mu}_l|}{|\boldsymbol{I}|}. \tag{2.7}$$

Atomic nuclei with an impair number of nucleons have a half-integer nuclear spin quantum number, whereas atoms with a pair number of nucleons have an integer nuclear magnetic quantum number. The case of a pair number of nucleons can be differentiated in impair number of both protons and neutrons and pair number of both protons and neutrons. In the first case most nuclei

have a $I \neq 0$ in the ground state whereas in the second case only nuclei in excited states have a $I \neq 0$. $2I + 1$ states exist for an atomic nucleus that are denoted by the magnetic quantum spin number $m_l \in -I, -I + 1, \ldots + I$.

Proton

Since only proton MRI was performed in this thesis, only hydrogen is considered in the rest of this thesis. The hydrogen atom consists of a sole proton, that has an orbital angular quantum number of 0 and spin quantum number of $\frac{1}{2}$. The quantum mechanical spin operator's matrix representation is

$$\boldsymbol{S} = \frac{\hbar}{2}\boldsymbol{\sigma} \tag{2.8}$$

for spin $\frac{1}{2}$ observables with $\boldsymbol{\sigma}$ the Pauli Matrices:

$$\sigma_x = \begin{pmatrix} 0 & 1 \\ 1 & 0 \end{pmatrix}, \sigma_y = \begin{pmatrix} 0 & -i \\ i & 0 \end{pmatrix}, \sigma_z = \begin{pmatrix} 1 & 0 \\ 0 & -1 \end{pmatrix}. \tag{2.9}$$

A proton inside a constant magnetic field $\boldsymbol{B} = B_0 \cdot \hat{z}$ will have a potential energy of

$$U = -\boldsymbol{\mu} \cdot \boldsymbol{B} = -\gamma S_{\hat{z}} B_0. \tag{2.10}$$

For a stationary proton, the Hamiltonian becomes

$$H = -\gamma S_z B_0 = \begin{pmatrix} -\frac{1}{2}\hbar\omega_0 & 0 \\ 0 & +\frac{1}{2}\hbar\omega_0 \end{pmatrix} \tag{2.11}$$

with $\omega_0 = B_0\gamma$. The two solutions of the time-independent Schrödinger equation $H\Psi = E\Psi$ are

$$\psi_{+1/2} = \begin{pmatrix} 1 \\ 0 \end{pmatrix} \psi_{-1/2} = \begin{pmatrix} 0 \\ 1 \end{pmatrix} \tag{2.12}$$

with $E_\pm = \mp\frac{1}{2}\hbar\omega_0$.

The wave function of the proton is

$$\Psi(t) = \sum_{m=\pm\frac{1}{2}} C_m \psi_m e^{-\frac{i}{\hbar}E_m t}. \tag{2.13}$$

The normalization condition $< \Psi|\Psi > \equiv 1$ demands that $V \sum_m |C_m|^2 = 1$ (the factor V arises

from the integration over the volume containing the proton), since $\psi_{+1/2}$ and $\psi_{-1/2}$ are orthogonal. The expectation value of the magnetic moment as a function of time $\boldsymbol{\mu}(t)$ can be calculated as

$$< \Psi|\boldsymbol{\mu}|\Psi >\equiv \int \Psi^\dagger \boldsymbol{\mu}\Psi dV = \Psi^\dagger \boldsymbol{\mu}\Psi V = \gamma V \sum_m \sum_{m'} C_{m'} C_m \psi^\dagger_{m'} \frac{\hbar}{2}\boldsymbol{\sigma}\psi_m e^{-\frac{i}{\hbar}(E_{m'}-E_m)t}. \quad (2.14)$$

With

$$\psi^\dagger_{m'}\boldsymbol{\sigma}\psi_m = \hat{x}\delta_{m',-m} + 2mi\hat{y}\delta_{m',-m} + 2m\hat{z}\delta_{m',m}, \quad (2.15)$$

the spatial components can be calculated to:

$$< \mu_x > = \frac{1}{2}\hbar\gamma V(C^*_{+\frac{1}{2}}C_{-\frac{1}{2}}e^{i\omega_0 t} + C^*_{-\frac{1}{2}}C_{+\frac{1}{2}}e^{-i\omega_0 t}) \quad (2.16)$$

$$< \mu_y > = \frac{1}{2}\hbar\gamma V(-iC^*_{+\frac{1}{2}}C_{-\frac{1}{2}}e^{-i\omega_0 t} + iC^*_{-\frac{1}{2}}C_{+\frac{1}{2}}e^{+i\omega_0 t}) \quad (2.17)$$

$$< \mu_z > = \frac{1}{2}\hbar\gamma V(C^*_{+\frac{1}{2}}C_{+\frac{1}{2}} - C^*_{-\frac{1}{2}}C_{-\frac{1}{2}}). \quad (2.18)$$

Writing the coefficients in complex exponential notation: $C_{+\frac{1}{2}} = a_{+\frac{1}{2}}e^{i\alpha_{+\frac{1}{2}}}$ and $C_{-\frac{1}{2}} = a_{-\frac{1}{2}}e^{i\alpha_{-\frac{1}{2}}}$ the normalization condition demands $V(a^2_{+\frac{1}{2}} + a^2_{-\frac{1}{2}}) = 1$, which is satisfied by $a_{+\frac{1}{2}} \equiv \frac{1}{\sqrt{V}}\cos(\frac{\theta}{2})$ and $a_{-\frac{1}{2}} \equiv \frac{1}{\sqrt{V}}\sin(\frac{\theta}{2})$. Introducing $\varphi_0 \equiv \alpha_{-\frac{1}{2}} - \alpha_{+\frac{1}{2}}$ leads to:

$$< \mu_x > = \frac{1}{2}\hbar\gamma\sin(\theta)\cos(\varphi_0 - \omega_0 t) \quad (2.19)$$

$$< \mu_y > = \frac{1}{2}\hbar\gamma\sin(\theta)\sin(\varphi_0 - \omega_0 t) \quad (2.20)$$

$$< \mu_z > = \frac{1}{2}\hbar\gamma\cos(\theta). \quad (2.21)$$

Thus, the expectation value of the magnetic moment rotates around the z-axis with the frequency ω_0.

Radiofrequency pulse

If another left circularly polarized magnetic field $\boldsymbol{B}_1(t) = B_1(\hat{x}\cos(\omega_0 t) - \hat{y}\sin(\omega_0 t))$ is applied, the Hamiltonian of the proton becomes:

$$H(t) = -\boldsymbol{\mu}\boldsymbol{B}(t) = -\frac{\gamma\hbar}{2}(\sigma_z B_0 + (\sigma_x\cos(\omega_0 t) - \sigma_y\sin(\omega_0 t))B_1). \quad (2.22)$$

The $\boldsymbol{B}_1(t)$ is applied "on resonance", which means that its frequency equals the precession

frequency of the nuclear spins. The Schrödinger equation is then

$$\frac{i\hbar\partial\Psi}{\partial t} = H(t)\Psi = -\frac{\hbar}{2}\begin{pmatrix} \omega_0 & \omega_1 e^{i\omega_0 t} \\ \omega_1 e^{-i\omega_0 t} & -\omega_0 \end{pmatrix}\Psi \tag{2.23}$$

with $\omega_1 = \gamma B_1$. The general form of the wave function is

$$\Psi = \begin{pmatrix} \psi_1^{'}(t)e^{\frac{i\omega_0 t}{2}} \\ \psi_2^{'}(t)e^{-\frac{i\omega_0 t}{2}} \end{pmatrix} \tag{2.24}$$

and its time derivative a coupled system:

$$\begin{aligned} \frac{d\psi_1^{'}}{dt} &= \frac{i}{2}\omega_1\psi_2^{'} \\ \frac{d\psi_2^{'}}{dt} &= \frac{i}{2}\omega_1\psi_1^{'}. \end{aligned} \tag{2.25}$$

The second time derivatives are

$$\frac{d^2\psi_{1,2}^{'}}{dt^2} = -\frac{1}{4}\omega_1^2\psi_{1,2}^{'} \tag{2.26}$$

with the general solutions:

$$\psi_1^{'}(t) = c_1\cos(\frac{\omega_1 t}{2}) + c_2\sin(\frac{\omega_1 t}{2}) \tag{2.27}$$

$$\psi_2^{'}(t) = c_3\cos(\frac{\omega_1 t}{2}) + c_4\sin(\frac{\omega_1 t}{2}) \tag{2.28}$$

$$c_3 = -ic_2 \tag{2.29}$$

$$c_4 = ic_1. \tag{2.30}$$

The expectation value of $\boldsymbol{\mu}$ are then

$$< \mu_{x'} > = \hbar\gamma V Re(\psi_1^{'}\psi_2^{'}) \tag{2.31}$$

$$< \mu_{y'} > = \hbar\gamma V Im(\psi_1^{'}\psi_2^{'}) \tag{2.32}$$

$$< \mu_z > = \frac{1}{2}\hbar\gamma V(|\psi_1^{'}|^2 - |\psi_2^{'}|^2). \tag{2.33}$$

The normalization implies that $V = (|c_1|^2 + |c_2|^2) = 1$, with the general solutions $c_1 = \frac{1}{\sqrt{V}}\cos(\frac{\theta}{2})e^{-i\varphi_1}$ and $c_2 = \frac{1}{\sqrt{V}}\sin(\frac{\theta}{2})e^{-i\varphi_2}$. This leads to:

$$< \mu_{x'}(t) > = \frac{\hbar\gamma}{2} \sin\theta \cos\varphi \tag{2.34}$$

$$< \mu_{y'}(t) > = \frac{\hbar\gamma}{2} (\cos\theta \sin\omega_1 t + \sin\theta \cos\omega_1 t \sin\varphi) \tag{2.35}$$

$$< \mu_z(t) > = \frac{\hbar\gamma}{2} (\cos\theta \cos\omega_1 t - \sin\theta \sin\omega_1 t \sin\varphi) \tag{2.36}$$

with $\theta = \varphi_1 - \varphi_2 - \frac{\pi}{2}$. At t = 0 the expectation values of the different components of the magnetic moment vector are

$$< \mu_{x'}(0) > = \frac{\hbar\gamma}{2} \sin\theta \cos\varphi \tag{2.37}$$

$$< \mu_{y'}(0) > = \frac{\hbar\gamma}{2} \sin\theta \sin\varphi \tag{2.38}$$

$$< \mu_z(0) > = \frac{\hbar\gamma}{2} \cos\theta. \tag{2.39}$$

The temporal evolution can then be rewritten to

$$< \mu_{x'}(t) > =< \mu_{x'}(0) > \tag{2.40}$$

$$< \mu_{y'}(t) > =< \mu_{y'}(0) > \cos\omega_1 t + < \mu_z(0) > \sin\omega_1 t \tag{2.41}$$

$$< \mu_z(t) > = - < \mu_{y'}(0) > \sin\omega_1 t + < \mu_z(0) > \cos\omega_1 t. \tag{2.42}$$

The expectation value of the magnetic moment vector precesses around the axis $x^{'}$ of the applied $\boldsymbol{B}_1$ field with the frequency ω_1.

Thermal equilibrium

A system of N spins s with magnetic quantum number $m_s \equiv m$ in an external magnetic field $\boldsymbol{B} = B_0 \cdot z$ that are in thermal contact with each other at a temperature T is observed. The thermal equilibrium value M_0 of the magnetization in z direction M_z, can be calculated as the average of the total magnetic moment of the N spins. With $\rho_0 = \frac{N}{V}$, the thermal average of the z component of the magnetization is

$$M_0 = \rho_0 \sum_{m=-s}^{s} P(\varepsilon(m)) \mu_z(m). \tag{2.43}$$

With the energy $\varepsilon = -m\hbar\omega_0$ and $P = \frac{e^{-\frac{\varepsilon}{kT}}}{\sum_\varepsilon e^{-\frac{\varepsilon}{kT}}}$ the probability that the system has energy ε while in contact with a much larger system at temperature T.

With $\mu_z = m\gamma\hbar$ and $u = \frac{\hbar\omega_0}{kT}$, M_0 becomes:

$$M_0 = \frac{N\gamma\hbar \sum_{m=-s}^{s} m e^{mu}}{V \sum_{m=-s}^{s} e^{mu}}. \tag{2.44}$$

For the proton, where two spin states ($\pm\frac{1}{2}$) exist:

$$P_{\pm} = \frac{e^{\pm\frac{u}{2}}}{e^{\frac{u}{2}} + e^{\frac{-u}{2}}}. \tag{2.45}$$

The difference between the probabilities of the two states is

$$\frac{e^{+\frac{u}{2}} - e^{-\frac{u}{2}}}{e^{\frac{u}{2}} + e^{\frac{-u}{2}}} \tag{2.46}$$

which can be approximated as $\frac{u}{2}$, since $u \approx 0$. At the body temperature of ≈310K, $u = 6.6 \times 10^{-6} B_0 \cdot \frac{1}{T}$ (T is the unit Tesla in this formula). The net magnetization that results from the difference between the populations of the two states is higher with higher B_0.

2.1.2 Semiclassical Description

In the case of large systems, a classical description is possible according to Bohr's correspondence principle. Excessive spins on the lower energy level contribute to a net macroscopic magnetization $\boldsymbol{M} = (M_x, M_y, M_z)$. The equation of motion for this macroscopic magnetization is

$$\frac{d}{dt}\boldsymbol{M}(t) = \gamma \boldsymbol{M}(t) \times \boldsymbol{B}(t). \tag{2.47}$$

2.1.2.1 Relaxation

Proton spins inside a magnetic field interact with a surrounding lattice. The change rate of the macroscopic longitudinal magnetization $\frac{dM_z(t)}{dt}$ that is aligned with the external magnetic field is proportional to the difference of the equilibrium magnetization M_0 and $M_z(t)$. The proportionality constant is empirically determined and called T_1, the spin-lattice relaxation time. The change rate of the macroscopic longitudinal magnetization is described by

$$\frac{dM_z(t)}{dt} = \frac{1}{T_1}(M_0 - M_z(t)). \tag{2.48}$$

with the solution

$$M_z(t) = M_z(0)e^{-\frac{-t}{T_1}} + M_0(1 - e^{\frac{-t}{T_1}}). \tag{2.49}$$

Similarly, the transverse magnetization that is directed orthogonal to the static external magnetic field relaxes. Nuclear spins experience a local magnetic field which is composed of the external magnetic field and the magnetic fields generated by their neighbors. The local magnetic field component caused by their neighbors is not the same for each spin in an ensemble of spins. Each spin therefore has a slightly different precession frequency. Since the magnetization of this ensemble is the sum of all individual transverse components, increasing phase differences lead to a decrease of the net transverse magnetization.

To simplify further considerations, the rotating frame concept is introduced. Instead of observing the magnetization M in the static laboratory frame of reference, a frame that is rotating with the same frequency ω_0 as the spins is introduced. Exemplarily the trajectory of the net magnetization of a spin ensemble is shown in the laboratory frame and in the rotating frame (Figure 2.1). The vector is rotated about the x-axis while precessing around the z-axis with frequency ω_0. In the rotating frame, the only trajectory that is observed is the rotation about the x'-axis.

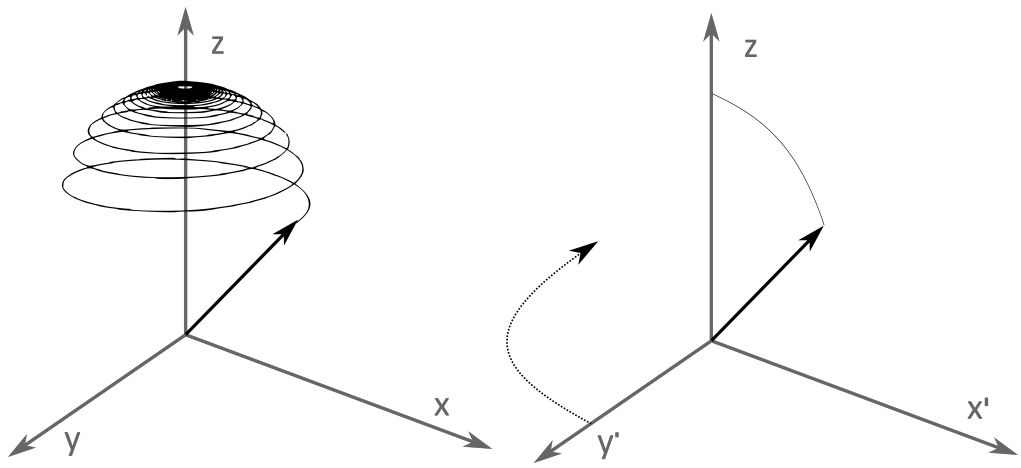

Figure 2.1: Left: Trajectory of magnetization that experiences a static magnetic field and another magnetic field with the same frequency as the Larmor precession frequency. The magnetization simultaneously rotates around the z-axis and an orthogonal axis to the z-axis. In the rotating frame, the observed trajectory of the same motion is the rotation around the x' axis only.

The change of the transverse component of the magnetization $\frac{d\boldsymbol{M}_{xy}}{dt}$ is proportional to another empirically determined constant T_2, called spin-spin relaxation rate. In the rotating frame the differential equation describing the relaxation of the transverse relaxation is:

$$\frac{d\boldsymbol{M}_{xy}}{dt} = -\frac{1}{T_2}\boldsymbol{M}_{xy} \tag{2.50}$$

with the solution

$$\boldsymbol{M}_{xy}(t) = \boldsymbol{M}_{xy}(0)e^{-\frac{t}{T_2}}. \tag{2.51}$$

Besides the local spin-spin interactions the external macroscopic magnetic field is not homogeneous which leads to a faster reduction of transverse net magnetization. Different susceptibilities in different tissues as well as the magnet's static field contribute to this effect. This decay is characterized with T_2'. The overall decay of the transverse magnetization is described by $\frac{1}{T_2^*} = \frac{1}{T_2} + \frac{1}{T_2'}$:

$$\frac{d\boldsymbol{M}_{xy}}{dt} = -\frac{1}{T_2^*}\boldsymbol{M}_{xy}. \tag{2.52}$$

T_2'-decay in contrast to T_2-decay is reversible, which means that the arising phase differences stemming from slightly different precession frequencies can be rewound since they are static in time. This is not possible for the phase differences arising because of local spin-spin interactions. The full equations of motion are the Bloch equations that describe the motion of nuclear magnetization with relaxation:

$$\frac{dM_x(t)}{dt} = \gamma(\mathbf{M}(t) \times \mathbf{B}(t))_x - \frac{M_x(t)}{T_2^*} \tag{2.53}$$

$$\frac{dM_y(t)}{dt} = \gamma(\mathbf{M}(t) \times \mathbf{B}(t))_y - \frac{M_y(t)}{T_2^*} \tag{2.54}$$

$$\frac{dM_z(t)}{dt} = \gamma(\mathbf{M}(t) \times \mathbf{B}(t))_z - \frac{M_z(t) - M_0}{T_1}. \tag{2.55}$$

2.1.2.2 MR Signal Simulations

Simulations of the MR signal can be performed by finitely calculating the Bloch equations. Another description is the extended phase graph [Wei15] concept that describes nuclear magnetization in terms of configurations states. The effect of timely varying magnetic fields are described by matrix operations on these configuration states.

2.2 Magnetic Resonance Imaging

In this section, techniques of using magnetic fields in order to manipulate nuclear spins inside objects or living organisms to obtain measurable signals are described. After explaining the free induction decay (FID), the following part of this section is divided into one part that describes the image formation and another part that describes the signal generation. It should be noted that although the second part which describes the signal generation is denoted 'Sequences', a sequence can also require a distinct method for image formation.

Free Induction Decay

A basic MR experiment involves the application of an RF pulse to a sample inside a temporally constant magnetic field B_0. The measured signal $s(t)$ is acquired with coils surrounding the sample and demodulated at the frequency ω_0 (Figure 2.2):

$$s(t) \propto \omega_0 \int d^3 r e^{-\frac{t}{T_2^*(\boldsymbol{r})}} M_{xy}(\boldsymbol{r}, 0) B'_{xy}(\boldsymbol{r}) e^{i(\varphi_0(\boldsymbol{r}) - \theta_{B'}(\boldsymbol{r}))} \tag{2.56}$$

with $B'_{xy}(\boldsymbol{r})$ the receive field magnitude, $\theta_{B'}(\boldsymbol{r})$ the receive field phase, $M_{xy}(\boldsymbol{r}, 0)$ the transverse magnetization magnitude and $\varphi_0(\boldsymbol{r})$ the magnetization phase at t=0.

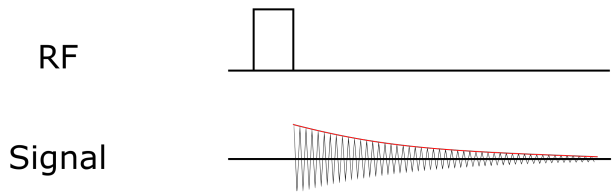

Figure 2.2: Application of an RF pulse and the generated signal (not demodulated in black and demodulated in red) of a sample.

The signal called free induction decay (FID) can be sampled and Fourier transformed to obtain a spectrum of the frequencies present in the sample.

2.2.1 Image Formation

Most MR experiments however are intended to yield spatial rather than spectral information. Several properties of MR experiments can be utilized to spatially resolve the information obtained from a sample.

Slice/Slab Selective & Nonselective Excitation

In a large volume V another magnetic field $G_z = \frac{\partial B_z}{\partial z}$ can be applied, that leads to a constant gradient of the precession frequency in one direction while ideally being constant in the other (perpendicular) directions.

$$f(z) = f_0 + \gamma \cdot G_z \cdot z \tag{2.57}$$

An RF pulse with a certain bandwidth can then be designed to only manipulate spins that are inside a frequency band. In the simplest case, this can be approximated by the inverse Fourier transform of the desired frequency profile. Since the spin precession frequency depends only on the position in z-direction the RF pulse will only excite spins at distinct positions in z-direction. For a non-selective excitation, no G_z is needed and an RF pulse employed that excites all spins in the volume V. Schematic examples of a slice selective pulse (Figure 2.3a)), the simultaneously applied gradient (Figure 2.3b)) and a non-selective pulse (Figure 2.3c)) are shown in Figure 2.3.

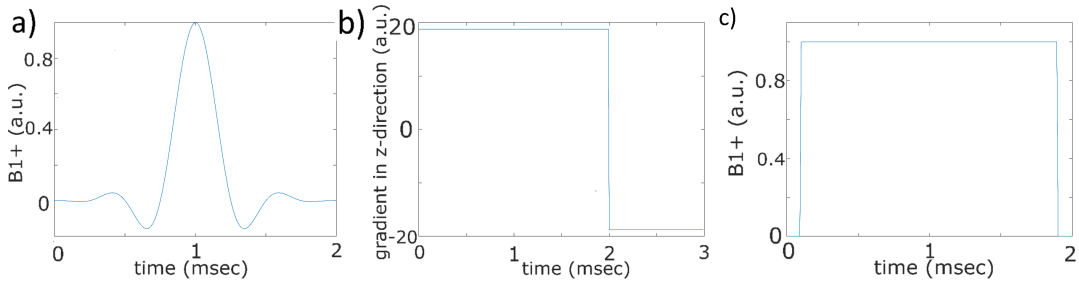

Figure 2.3: Schematic illustration of a slice selective pulse and its associated gradient and a non-selective pulse. a) shows the applied B_1^+ of a slice-selective pulse over time and b) the associated gradient in z-direction including the rewinding moment beginning after two milliseconds. c) shows an example of a non-selective pulse.

K-Space and Cartesian Sampling

During the time the signal generated by the transverse magnetization is sampled, another magnetic gradient field $G_x = \frac{\partial B_z}{\partial x}$ can be applied in one direction such that:

$$f(x) = f_0 + \gamma \cdot G_x \cdot x. \tag{2.58}$$

A phase $\varphi_G(x,t)$ is accrued for the time the magnetic gradient field is applied:

$$\varphi_G(x,t) = -\gamma x \int_0^t dt' \, G_x(t'). \tag{2.59}$$

The measured signal is (with $\rho(x)$ the spin density at position x):

$$s(t) = \int dx \rho(x) e^{i\varphi_G(x,t)}. \tag{2.60}$$

Introducing the spatial frequency $k_x = k_x(t) = \frac{\gamma}{2\pi} \int_0^t dt' G_x(t')$ leads to:

$$s(k_x) = \int dx \rho(x) e^{-i2\pi k_x(t)x}. \tag{2.61}$$

The inverse Fourier transform of $s(k_x)$ yields

$$\rho(x) = \int dk_x \, s(k_x) e^{+i2\pi k_x(t)x}. \tag{2.62}$$

Sampling the signal at different times while the gradient is switched on, means sampling spatial frequencies. By calculating the inverse Fourier transform, the spatially resolved signal is computed.

This equation can be expanded to three spatial dimensions:

$$s(\boldsymbol{k}) = \int d^3r \, \rho(\boldsymbol{r}) e^{-i2\pi \boldsymbol{k}\boldsymbol{r}} \tag{2.63}$$

with

$$\boldsymbol{k} = \boldsymbol{k}(t_1, t_2, t_3) = \frac{\gamma}{2\pi} \begin{pmatrix} \int_0^{t_1} G_x(t_1') dt_1' \\ \int_0^{t_2} G_y(t_2') dt_2' \\ \int_0^{t_3} G_z(t_3') dt_3' \end{pmatrix} \tag{2.64}$$

such that

$$\rho(\boldsymbol{r}) = \int d^3k \, s(\boldsymbol{k}) e^{+i2\pi \boldsymbol{k}\boldsymbol{r}}. \tag{2.65}$$

K-space is sampled discretely. For frequency encoding, this means that the signal is sampled at discrete time steps Δt such that a step size $\Delta k_x = \frac{\gamma}{2\pi} \Delta t G_x$ separates the samples in k-space. The remaining dimensions that need to be encoded are phase encoded. This means that varying gradients are switched on before sampling the signal and frequency encoding. The steps in k-space

are:

$$\Delta k_y = \frac{\gamma}{2\pi} G_y \Delta t \tag{2.66}$$

$$\Delta k_z = \frac{\gamma}{2\pi} G_z \Delta t. \tag{2.67}$$

Some features of different k-space sampling patterns are illustrated in Figure 2.4. The original image (2.4 a)) and its (logarithmic) k-space representation (Figure 2.4 b)) are depicted. The k-space data of the low-frequencies is responsible for the image contrast (Figure 2.4 d)), while the higher frequencies contain the edge information (Figure 2.4 e)). The pixel size Δw is determined by $\Delta w = \frac{1}{k_{\max}-(-k_{\max})}$ An image of an extension x has to be sampled with $\Delta k = \frac{1}{x}$. If as exemplarily depicted in (2.4 c)) every third line is not acquired, artifacts when performing the inverse Fourier transform arise. Each of the three image segments (divided by the orange lines in Figure 2.4 a)) is aliased on the other segments (Figure 2.4 f)).

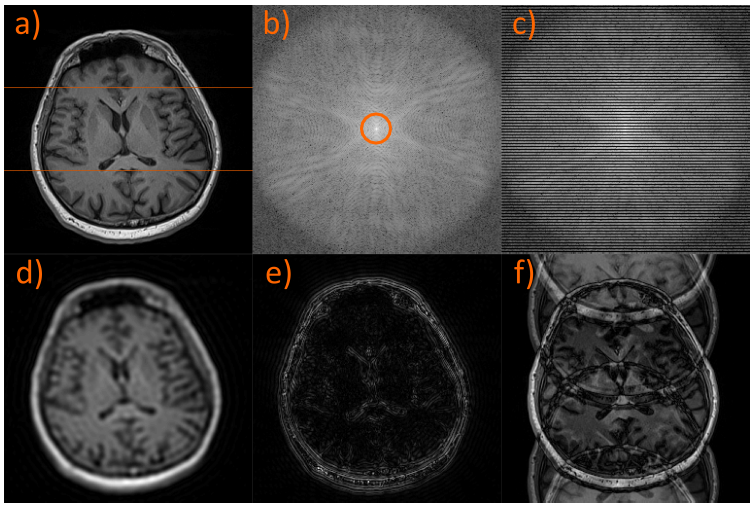

Figure 2.4: a) shows the original image (imaginarily divided into three segments by orange lines) and b) the logarithmic k-space representation. d) shows the image corresponding to the k-space inside the orange circle in b) and e) the image for the k-space data outside the circle. c) shows the same k-space data as b) where every third line is set to zeros and f) the corresponding image with undersampling artifacts. The three segments as delineated in a) are aliased on top of each other.

Non-Cartesian sampling

Sampling of data points is not restricted to a Cartesian raster (Figure 2.5a)). Non-cartesian methods exist in which the input signal is not sampled at equally spaced points. Two examples are radial (Figure 2.5b)) and spiral trajectories (Figure 2.5c) and d)) to sample k-space. These trajectories yield non-uniformly spaced samples in the spatial frequency domain, which obstructs

the use of fast Fourier Transforms that rely on uniformly spaced samples.

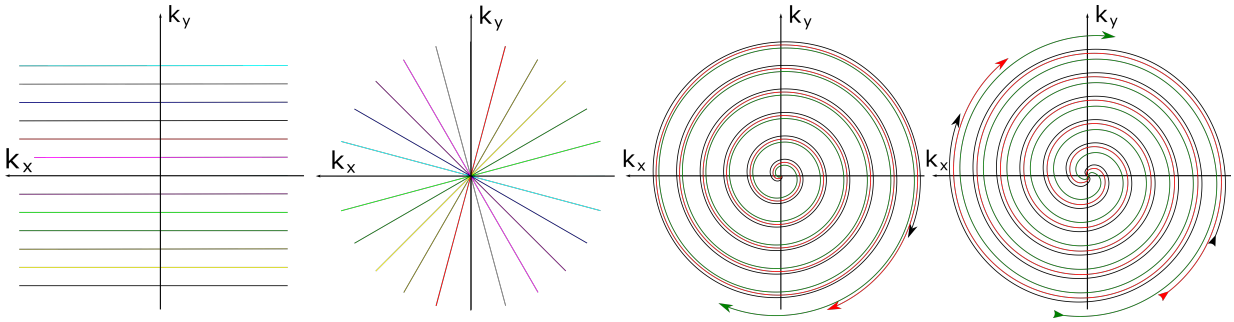

Figure 2.5: a) Cartesian k-space sampling pattern. b) radial sampling pattern. c) Spiral starting from the center of k-space and traversing it outwards. d) Spiral starting from the edge of k-space, traversing it inwards to the center and outwards to the edge again.

To reconstruct the non-Cartesian data, the measured k-space is usually projected onto a Cartesian grid, to be able to use computationally fast Fourier transform techniques. This process called nonuniform fast Fourier transform (NUFFT) involves a density compensation since k-space points are not necessarily equidistantly sampled and a convolution with functions such as e.g. Kaiser-Bessel to project the data onto a Cartesian grid.

2.2.2 Sequences

In this section the generation of signals in MRI is described. Two important general definitions are the time between the applications of two RF pulses in MRI which is usually denoted repetition time (TR) and the time between the application of an RF pulse and the echo sampling, echo time (TE).

Gradient Echo

One of the two basic types of MRI sequences is the gradient echo. A gradient echo consists of an RF pulse that excites spins and a latter applied gradient in one direction (Figure 2.6). The generated signal is sampled during the application of the gradient. The applied gradient dephases the spins such that the signal decreases during the readout. This leads to asymmetric k-space information.

To solve this, the experiment is altered by adding a gradient that has opposed sign than the gradient during readout (Figure 2.6). The experiment thus leads to a range of negative and positive k-space points for measurements made symmetrically about the echo. The negative gradient prephases the

spin ensemble such that in the middle of the positive rephasing gradient an echo is created.

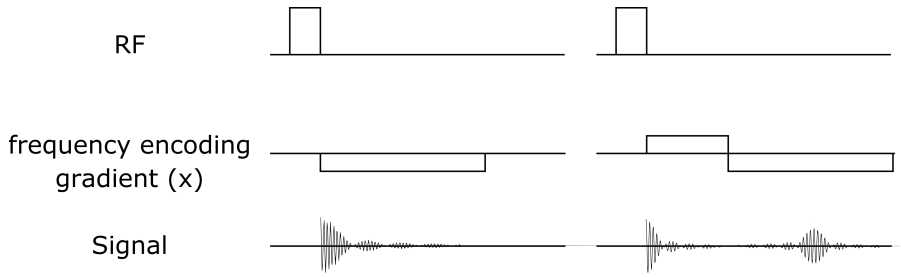

Figure 2.6: On the left side a gradient echo experiment without prephasing gradient and on the right side one with a prephasing gradient are shown as well as for both the generated signals. With the prephasing gradient, the signal during the readout (negative frequency encoding gradient) is symmetrical.

When combining this experiment with phase encoding, multiple RF pulses with following readout gradients can be performed. With each readout, one line in k-space is sampled. The utilized TR (time between successive RF pulses) and TE (time between RF pulse and the data sampling) influence the signal strength from specimens with different relaxation parameters T_1 and T_2.

Gradient echo sequences exist in several variants. One is the so called (Fast Low-Angle Shot) FLASH technique (Figure 2.7). In this technique, gradients are applied after each readout has finished, to spoil remaining magnetization, that could refocus later due to further RF pulses being applied. Furthermore, the phase of the RF pulses is varied to minimize this effect and to generate signals that are mostly affected by T_1.

Another technique is the so called ssfp (steady-state free precession) or FISP (fast imaging with steady-state precession). Here the RF pulses have the same phase while gradient spoiling can be performed optionally (Figure 2.8).

In bssfp (balanced steady-state free precession) or TrueFISP (true fast imaging with steady-state precession) the phases of the pulses are alternating (0 and 180°), while all gradient moments are zero in each TR (Figure 2.9). This leads to a B_0 dependency of the generated signal, since the relative phase of a spin ensemble to the RF pulses varies with its precession frequency B_0. In the case where the spins precess 180° between RF pulses, the relative phase between RF pulses and spin ensembles stays constant. This generates a very small signal and is called stop-band condition. However, the signal response generally varies with B_0 in this sequence. Under the stop-band condition, this effect is just the strongest. On the other hand, since all signal is always rephased, this gradient echo sequence produces high signal and is similar to spin echo sequences.

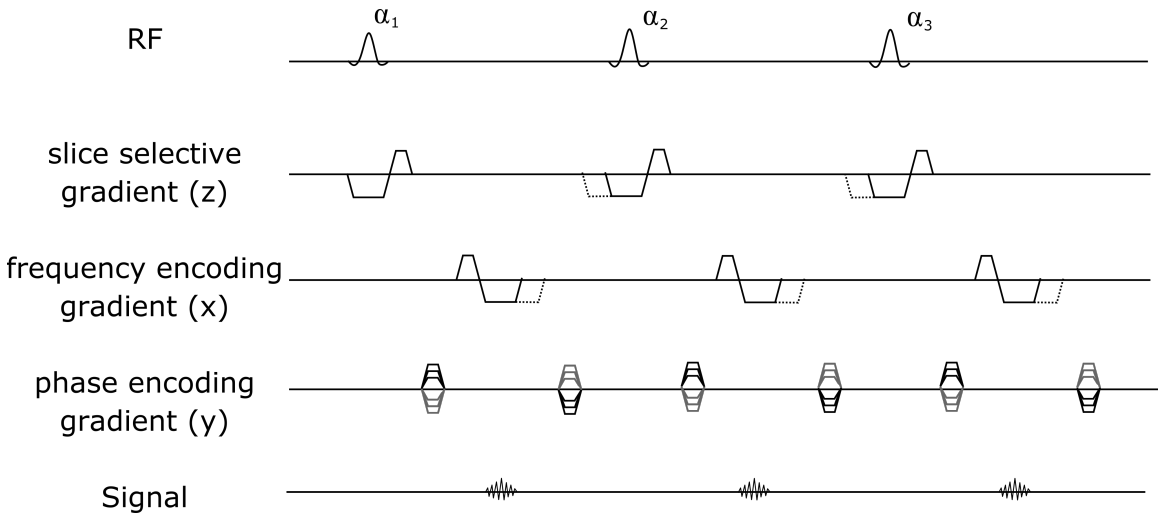

Figure 2.7: Sequence diagram of a FLASH sequence, where RF pulses vary in phase. Slice selective and readout gradients are unbalanced and can also be further unbalanced by adding spoiling gradient moments, while phase encoding gradients are rewound.

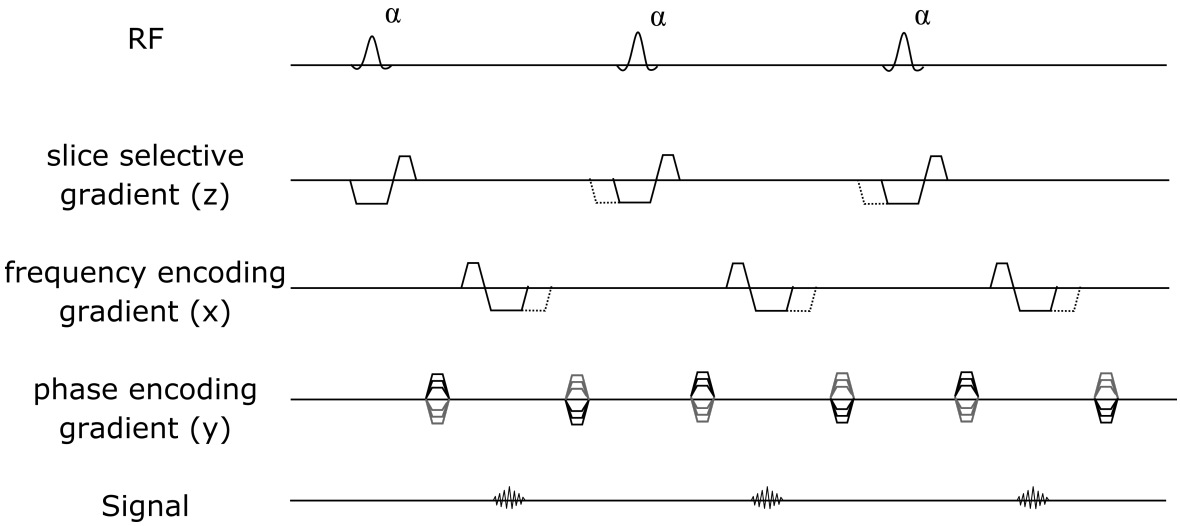

Figure 2.8: Sequence diagram of a FISP sequence, where RF pulses do not vary. Slice selective and readout gradient moments are unbalanced and can also be further unbalanced by adding spoiling moments (dashed lines), while phase encoding gradient moments are rewound.

Spin Echo

The other basic type of MR experiments is the spin echo experiment. With this method, the dephasing due to static-field inhomogeneities can be reversed. In gradient echo techniques, the artificial dephasing by the application of prephasing gradients is rephased but not the dephasing due to static-field inhomogeneities. The T_2* dephasing is usually much faster than the pure T_2 and thus higher signals can be achieved with spin echoes.

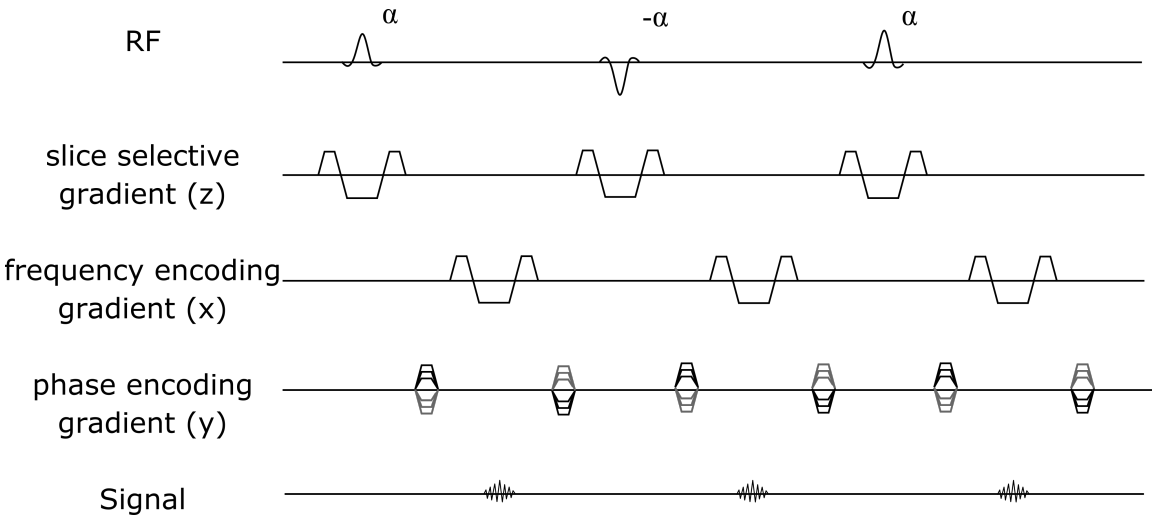

Figure 2.9: Sequence diagram of a TrueFISP sequence, where RF pulses phases alternate (0 and 180 degree). All gradient moments are balanced.

A spin echo experiment (Figure 2.10) consists of the application of a 90° RF pulse and another 180° RF pulse after TE/2. The phase offsets between the spins that accumulates between the two pulses is flipped by 180° by the second RF pulse. Since the precession frequency offsets are constant, the reversed phase offsets are zero after another time period TE/2 (Figure 2.11). The T_2 decay however is not reversible.

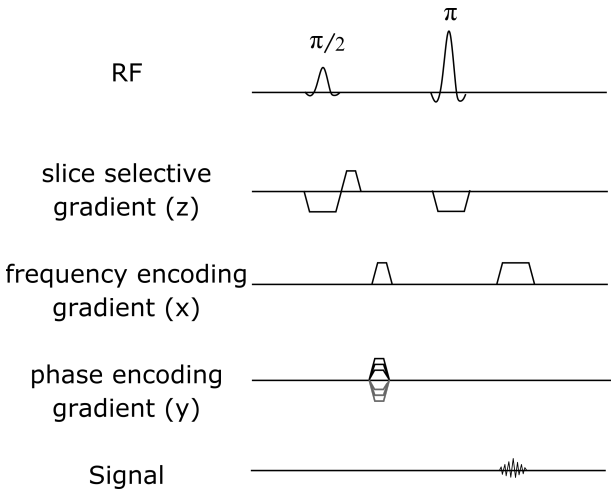

Figure 2.10: Sequence diagram of a spin echo sequence. The application of a 90° RF pulse is followed by another 180° pulse after TE/2. Another TE/2 later, the spin echo is produced and acquired.

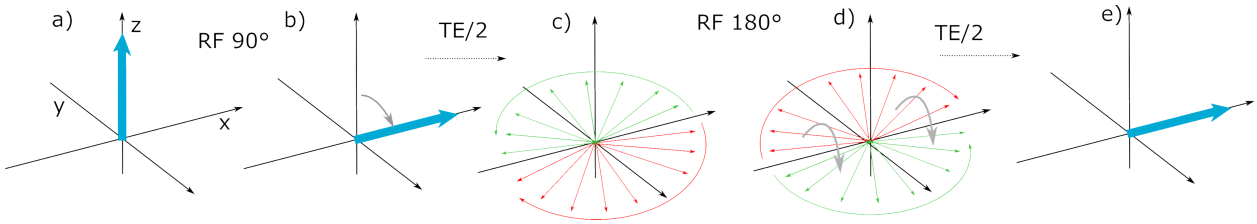

Figure 2.11: In a) all spins are oriented in z- direction. The 90° pulse flips the magnetization in the transverse plane, after which the spins dephase for TE/2. The 180° pulse flips the spins and effectively also the relative phases to each other. After another TE/2 all spins are again aligned and a spin echo produced.

Multi-Echo Spin Echo

The simple spin echo experiment can be performed with more than one $180°$ RF pulse following the $90°$ RF pulse (Figure 2.2.2). Usually spoiling gradients right before and after the $180°$ RF pulses are employed to spoil potential FIDs, when the pulses are not exactly $180°$. An important technique for minimizing the effect of RF pulses generating flip angles different from the expected ones is to fulfill the Carr-Purcell-Meiboom-Gill (CPMG) condition. It demands, that the $90°$ RF pulse has to be $90°$ phase shifted to the following $180°$ RF pulses, such that errors due to inaccurate flip angles are not accumulated.

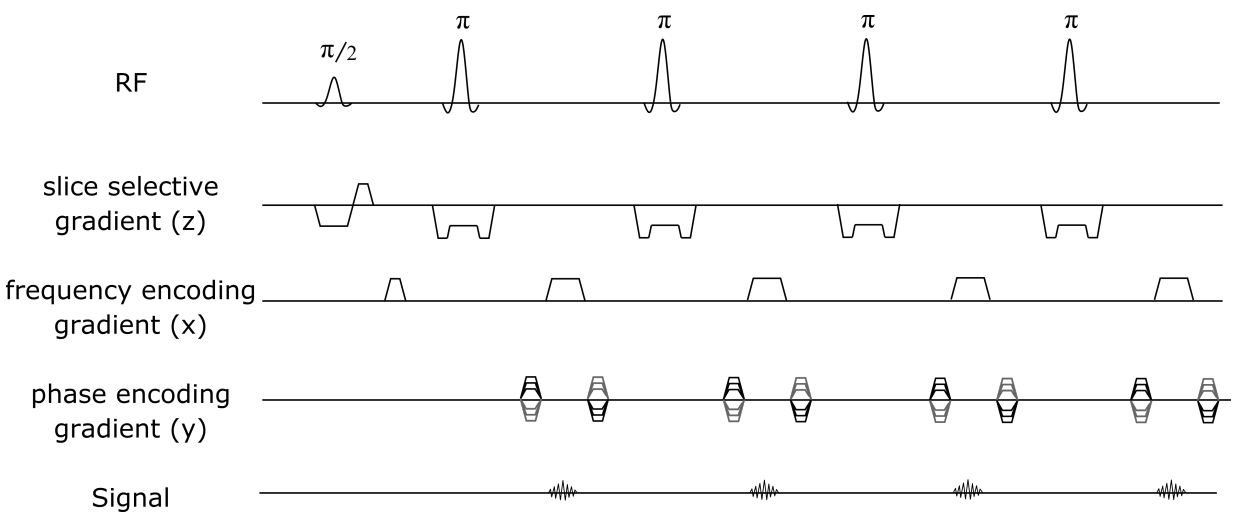

Figure 2.12: Sequence diagram of a multi-echo spin echo sequence. The application of a 90° RF pulse is followed by N 180° pulses after TE/2 + n× TE with n∈ $[0, 1, ..., N]$. Each TE/2 after an 180° pulse, a spin echo is produced and acquired. Usually additionally strong gradient spoiling moments (crushers) in slice-selective direction are played out before and after the 180° pulses to mitigate the effect of B_0 inhomogeneities.

Advanced Pulses

Besides hard RF pulses that are non-selective and slab-/slice-selective RF pulses, other RF pulses exist that have certain features. Adiabatic RF pulses vary in amplitude and frequency during application, such that the pulse's effect on the spins, i.e. achieving the desired flip angle is similar for a wide range of local B_1^+ field magnitudes. Adiabatic pulses are e.g. used as so called inversion pulses. Here, initial longitudinal magnetization is flipped by 180°. The time between the inversion pulse and the echo acquisition is denoted inversion time (TI). Inversion pulses are often designed to cover a whole volume which demands a homogeneous effect for various B_1^+ amplitudes.

Certain series of RF pulses compose preparation modules and are played out before the regular imaging sequence. One example is a T_2 preparation module that consists of a 90° pulse followed by a 180° RF pulse, a certain waiting period, another 180° RF pulse and -90° pulse flipping the spins back. This module has the purpose of amplifying the influence of T_2 on the received signal. During the waiting periods, the magnetization relaxes with T_2, thereby yielding different available longitudinal magnetization for following sequences depending on T_2.

Spectrally selective pulses can be played out with subsequent spoiling in order to minimize the signal from certain frequencies. One example is the suppression of fat signal, where proton spins in fat which have a slightly different precession frequency are excited and effectively spoiled before the acquisition of water proton spins begins. The frequency difference between proton spins in fat and water is $\sim$3.5ppm.

Contrast Weighting

Images produced by MRI are usually classified as T_1, T_2 or proton density weighted. By choosing imaging parameters such as TR, TE etc., different contrasts can be generated using the same sequence structure. In reality however, a contrast weighted image might be dominated by one tissue characteristic but still also affected by others. A pure contrast is very difficult to achieve since in general a multitude of parameters affects the MRI signal to a certain degree.

Most MR experiments are carried out in complex biological tissues. Simple models of single substance voxels do not fully describe the processes and effects occurring during an MRI scan, since more complex effects than T_1 and T_2 relaxation occur. These range from simple bulk subject motion and flow of fluids during an MR experiment to magnetization transfer, diffusion, susceptibility and perfusion effects. However, special MR sequences exist that are dedicated for producing images that reflect information related to these effects.

Shortcomings compared to ideal experiments

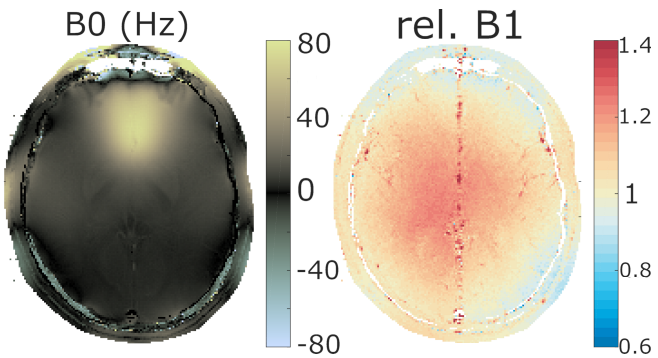

Figure 2.13: Examplary B_0 and B_1^+ distributions in a transversal slice through a human brain at a static magnetic field of 3T.

Compared to ideal experiments, several factors significantly affect MR experiments. Although a very high homogeneity is achieved in modern MRI systems, the static field B_0 is usually not homogeneous. Besides this rather small cause of B_0 inhomogeneity, permittivity and susceptibility differences of tissues cause different local B_0 field magnitudes as well as transition zones between tissues. The same holds for the transmit field B_1^+. Its inhomogeneity is caused by dielectric and standing wave effects. An exemplary distribution of B_0 and B_1^+ in a transverse slice through a human brain is depicted in Figure 2.13. Similar to the transmit B_1^+ field, the receive field is also not homogeneous. The so called coil sensitivities vary from coil to coil and depend among other factors on production quality, the number of coil elements and their position inside the coil.
Eddy currents and anisotropic gradient amplifier delays in the electronics generating the desired magnetic fields cause desired k-space trajectories to be distorted. Furthermore, concomitant gradient field effects can cause further k-space errors as well as signal phase errors in scans that are not carried out in the iso-center of the gradient system. These effects mostly affect non Cartesian trajectories such as radial and spiral trajectories. In Cartesian sampling only small phase changes in the reconstructed images are introduced. To correct for such deviations, multiple techniques are possible. The actually played out trajectory can be measured and used for the reconstruction of the data or a model that describes the effects can be parameterized to correct arbitrary trajectories. Examples are the generalized eddy-current model by Tan and Meyer [Tan09] and the Gradient Impulse Response Function (GIRF) [Van13, Van16, CW16].
MR scanners are highly complex physical measurement devices. Several types of scanners exist that differ e.g. in bore size and the gradient and transmit coils as well as electronics that drive the system. Besides the differences of scanner types, scanners of the same type can behave slightly different because of differences in the production and setup process of the magnet. Fast calibration

scans are usually carried out before MRI experiments to generate a homogeneous B_0 field or a reasonable transmit B_1^+ field to achieve the desired flip angles in the scanned probe. These are not always perfect and can cause differences from scan to scan. During the experiments the electronics and coils heat up and change their behavior slightly.
The combination of technical factors mentioned above (e.g. the B_1^+ transmit field can be different from scan to scan even on the same scanner and with similar positioning) and the complexity of investigated tissues hampers the generation of repeatable and reproducible contrast weighted MR images. Commonly contrast weighted images are only investigated for contrast differences within one acquisition.

2.3 Quantitative Magnetic Resonance Imaging

In this section, methods to quantify parameters associated with MRI are briefly described. The section is limited to the measurement of magnetic fields and relaxation parameters. The measurement of more parameters such as perfusion, diffusion, blood flow, magnetization transfer and susceptibility can of course also be performed.

2.3.1 Conventional Quantitative Magnetic Resonance Imaging

A common property of most conventional quantitative imaging techniques is the design of a certain MR sequence that is highly susceptible to the parameter that is intended to be quantified. However, similar as in contrast weighted imaging, other parameters might affect the obtained values and the assumption that the obtained information is solely influenced by the parameter to be quantified only holds for a certain range of all involved parameters.

1. B_0 **mapping**

   The main magnetic field B_0 can be measured by acquiring at least two images with different echo times TE while keeping all other parameters the same. The phase φ is proportional to the off-resonance and from the phase difference of the images with different echo times, the off-resonance can be computed:

$$\Delta f = \frac{\varphi(TE_2) - \varphi(TE_1)}{2\pi(TE_2 - TE_1)}. \tag{2.68}$$

2. B_1^+ **mapping**

For measuring the RF field B_1^+ several methods were proposed. The double-angle method [Sto88, IE92] consists of the acquisition of two images with flip angle α_1 and $\alpha_2 = 2\alpha_1$. All other parameters are kept constant. From the obtained magnitude images I_1 and I_2, the actual flip angle can be derived, when neglecting T_1 and T_2 relaxation:

$$\alpha(\boldsymbol{r}) = \arccos\left(\left|\frac{I_2(\boldsymbol{r})}{2I_1(\boldsymbol{r})}\right|\right). \tag{2.69}$$

Modifications of this technique exist, such as the method by Chung et al. [Chu10], where two images are acquired using a FLASH readout with and without a Slice Selective Preconditioning pulse of flip angle α_{nom}. The B_1^+ scaling factor $\kappa(\boldsymbol{r})$ can be found from the intensities of the two images ($I_{SSPre}(\boldsymbol{r})$ the intensity of the image with slice selective preconditioning pulse and $I_{PD}(\boldsymbol{r})$ the image intensity of the image without preconditioning pulse):

$$\kappa(\boldsymbol{r}) = \arccos\left(\frac{I_{SSPre}(\boldsymbol{r})}{I_{PD}(\boldsymbol{r})}\right)/\alpha_{nom}. \tag{2.70}$$

Another method [Ako93] utilizes the signal's dependency on stimulated echoes. It is based on the application of a pulse with flip angle α, another pulse after TE/2 with flip angle 2α and the sampling of the associated spin echo (SE) after another TE/2. After TM-TE/2 another RF pulse with flip angle α is applied and the associated stimulated echo (STE) acquired after another TE/2. TM is the mixing time and should be short compared to the T_1 of imaged species. The actual flip angle α_{act} can be computed from the ratio of the images from stimulated I_{STE} and spin echo I_{SE}:

$$\alpha_{act} = \arccos\left(\frac{I_{STE}(\boldsymbol{r})}{I_{SE}(\boldsymbol{r})}\right). \tag{2.71}$$

Other methods are actual flip-angle imaging AFI [Yar07] that acquires gradient-echo images at two different TRs, phase-sensitive methods, that encode B_1^+ information in the signal phase [Mor08] or using the Bloch-Siegert shift [Sac10].

3. T_1 **mapping**

In general many sequences that produce T_1 information can be utilized for T_1 mapping. All

methods have in common that a sequence is designed that provides one or more images that are strongly dependent on T_1 and only little to other parameters. T_1 is then fitted to the data. Several important general techniques are briefly described in this section, however a multitude of methods exist to measure T_1.

As a gold standard, the relaxation parameter T_1 can be measured by performing spin echo experiments with an inversion pulse and a subsequent waiting period called inversion time TI, before the actual spin echo experiment. The longitudinal magnetization is then proportional to T_1. This experiment can be repeated with different TIs, so that the equation for T_1 relaxation can be fitted to the obtained data points. This method is very slow, since a very long TR has to be employed to allow for full relaxation after each echo acquisition. With every echo, only one data acquisition (e.g. sampling one line of k-space) can be performed.

One way to speed this process up is the Look-Locker method [Loo70]. Here, the relaxation curve is sampled many times during the T_1 recovery (with a TR of τ) using RF pulses with flip angle α. The RF pulses alter the signal evolution and the effective T_1 ($T_{1,eff}$) obtained has to be corrected to determine the 'real' T_1:

$$\frac{1}{T_{1,eff}(\boldsymbol{r})} = \frac{1}{T_1(\boldsymbol{r})} - \frac{\ln(\cos\alpha)}{\tau}. \tag{2.72}$$

Saturation recovery (SR) techniques are an alternative to inversion recovery techniques. The longitudinal magnetization is effectively nulled by the application of a saturation pulse independently of its state before. Thus, there is no need to wait for T_1 recovery between saturation pulses. The regrowth of longitudinal magnetization can then be sampled after different waiting periods.

Partial saturation methods, work in a similar fashion. A steady-state is reached by continuously applying 90° pulses, spaced by TR. When assuming that TE is much smaller than T_2, the measured Signal S is only dependent on TR, $T_1(\boldsymbol{r})$ and $\rho(\boldsymbol{r})$ the proton density:

$$S(\boldsymbol{r}) = \rho(\boldsymbol{r})\left(1 - e^{\frac{-TR}{T_1(\boldsymbol{r})}}\right). \tag{2.73}$$

After acquiring images with at least two TRs, T_1 (and ρ) can be fitted to the acquired data.

With DESPOT1 (Driven-equilibrium single-pulse observation of T_1) [Chr74], T_1 quantification

is performed by acquiring at least two FLASH images with different flip angles, while keeping all other imaging parameters constant:

$$S(\boldsymbol{r}) = \frac{\rho(\boldsymbol{r})\left(1 - e^{\frac{-TR}{T_1(\boldsymbol{r})}}\right)\sin(\alpha)}{1 - e^{\frac{-TR}{T_1(\boldsymbol{r})}}\cos(\alpha)} \tag{2.74}$$

With known flip angle α and TR, $T_1(\boldsymbol{r})$ and $\rho(\boldsymbol{r})$ can be fitted to the measured signals. This method relies on the accuracy of the applied flip angles and is therefore susceptible to B_1^+ inhomogeneities.

4. **T_2 mapping and T_2^* mapping**

   Similar to T_1, techniques to measure T_2 usually generate multiple images that are highly T_2 dependent and desirably little dependent on other parameters. T_2 is then fitted to the data.

   As a gold standard, the relaxation parameter T_2 can be measured by performing pure spin echo experiments with varying echo times. This requires long repetition times between the spin echo measurements and takes a long time since only one data acquisition is performed per TR.

   This process can be sped up by performing a CPMG acquisition where many $180°$ pulses are applied. The downside of speeding the measurement up this way is the contribution of stimulated echoes or FIDs that can potentially corrupt the accuracy and precision, especially in the presence of B_1^+ inhomogeneities.

   When a T_1 map is known, DESPOT2 [Deo03] can be performed, which is based on a bssfp sequence. In the steady state, the signal is described by

$$S(\boldsymbol{r}) = \frac{\rho(\boldsymbol{r})\left(1 - e^{\frac{-TR}{T_1(\boldsymbol{r})}}\right)\cdot sin(\alpha)}{1 - e^{\frac{-TR}{T_1(\boldsymbol{r})}}e^{\frac{-TR}{T_2(\boldsymbol{r})}} - \left(e^{\frac{-TR}{T_1(\boldsymbol{r})}} - e^{\frac{-TR}{T_2(\boldsymbol{r})}}\right)\cdot cos(\alpha)}. \tag{2.75}$$

   Signals obtained with different α (and known TR) can be used to fit T_2 and the proton density ρ when T_1 is known. Similar to DESPOT1, DESPOT2 relies on exact knowledge of the flip angles.

   For T_2^* usually a FLASH acquisition is used with varying TE and T_2^* is fitted to the obtained signal curves.

2.3.2 Magnetic Resonance Fingerprinting

Since the result of an MRI experiment is in general potentially affected by a multitude of parameters, a sequence for a quantitative MR measurement needs to be robust against variations of other parameters while being sensitive to the parameter that is intended to be measured. MRF follows a different approach by accepting the fact that a sequence is sensitive to multiple parameters and makes them part of the solution.

In Magnetic Resonance Fingerprinting (MRF) [Ma13] flip angles, phases, and temporal spacings of a series of RF pulses are deliberately varied to generate a complex signal response, in contrast to conventional sequences where steady-state signals are utilized. Instead of fitting the measured signal response to a parameterized signal equation, in MRF the measured signals ("fingerprints") are compared with a precalculated dictionary of potentially observable signals. By comparing a measured fingerprint with the dictionary of simulated fingerprints, the most similar simulated fingerprint is identified. This identification process reveals the signal's properties, which are the parameters that the best matching fingerprint had been simulated with. This has the benefit that several parameters can be quantified simultaneously in a very efficient way since the sequence design can be much more complex than those having to follow an analytical model. This freedom opens up the possibility to design more efficient sequences for quantitative MRI but also to intrinsically resolve potential interdependencies of parameters by simultaneous quantification. With the dictionary based approach, more complex signal models taking more effects into account can be utilized since computational demanding tasks can be carried out before the measurement and not after such as in fitting methods.

MRF acquisitions can be substantially shortened by means of spatial undersampling. Established techniques for undersampling in MRF are single-shot spirals [Ma13, Jia15] and radial sampling [Clo16]. In principle, every undersampling strategy including conventional Cartesian sampling using GRAPPA (GeneRalized Autocalibrating Partial Parallel Acquisition) [Gri02], SENSE (Sensitivity Encoding) [Pru99], partial-Fourier or elliptical scanning can be utilized. The undersampling factors can be considerably higher than the ones applied in conventional MRI. The basic assumption underlying fast MRF is the hypothesis that a temporal variation of the undersampling pattern leads to incoherent aliasing artifacts in the time domain. Accordingly, the pattern matching process is assumed to be unaffected by these artifacts. An example of the fingerprinting framework is shown in Figure 2.14.

TrueFISP Magnetic Resonance Fingerprinting

In the first proof-of-principle of MRF [Ma13], a bssfp or TrueFISP sequence preceded by an

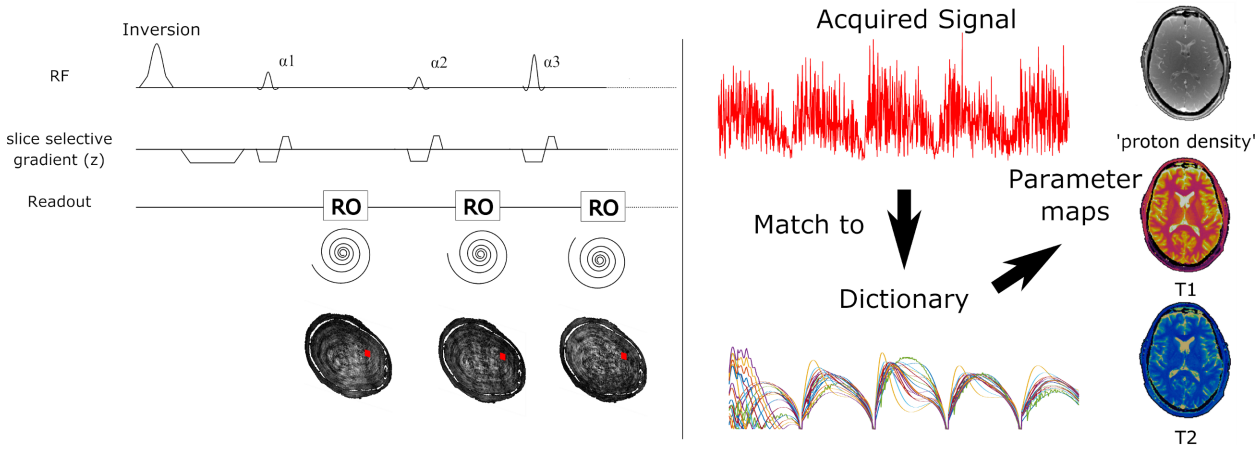

Figure 2.14: This examplary fingerprinting sequence starts with an inversion pulse and is followed by RF pulses with different flip angles. The sampling pattern for each data acquisition is a spiral that is rotated from data acquisition to data acquisition. The reconstructed images (in this case a human brain) are highly undersampled. When looking at the signal in the marked red pixel these undersampling artifacts can be observed over the time course. Comparing this acquired signal to the dictionary (set of simulated signal evolutions) the most similar signal is found and thereby also the parameters that it had been simulated with. When performing this comparison process for all pixels in the image the parameter maps (in this case T_1 and T_2) are reconstructed. Proton density is estimated a scaling factor of the measured signal.

inversion pulse was employed (Figure 2.15). The dictionary had a T_1, T_2 and off-resonance dimension. A variable density spiral trajectory was designed to sample k-space. A simple ascending reordering was used for MRF. Here, a limited number of spirals n is generated by rotating an initially designed spiral. For every data acquisition, the spiral is rotated by an angle $\alpha = (360^\circ)/n$. Although bssfp is an efficient gradient echo sequence in terms of encoding capability and signal-to-noise ratio, it is highly sensitive to off-resonances. Off-resonances are simulated and are identified by the pattern match, but signals under the stop band condition suffer from very low SNR and susceptibility effects, such that parameter map errors can be found at off-resonances.

Building on this implementation, pseudo-SSFP-MRF [Ass17] reduces the sensitivity of TrueFISP MRF to off-resonances and susceptibility effects. To this end, TE and TR patterns were derived from the flip angle pattern such that a spin echo like refocussing is achieved. TR and TE are altered to account for varying dispersion widths of spin ensembles for pulses with different flip angles.

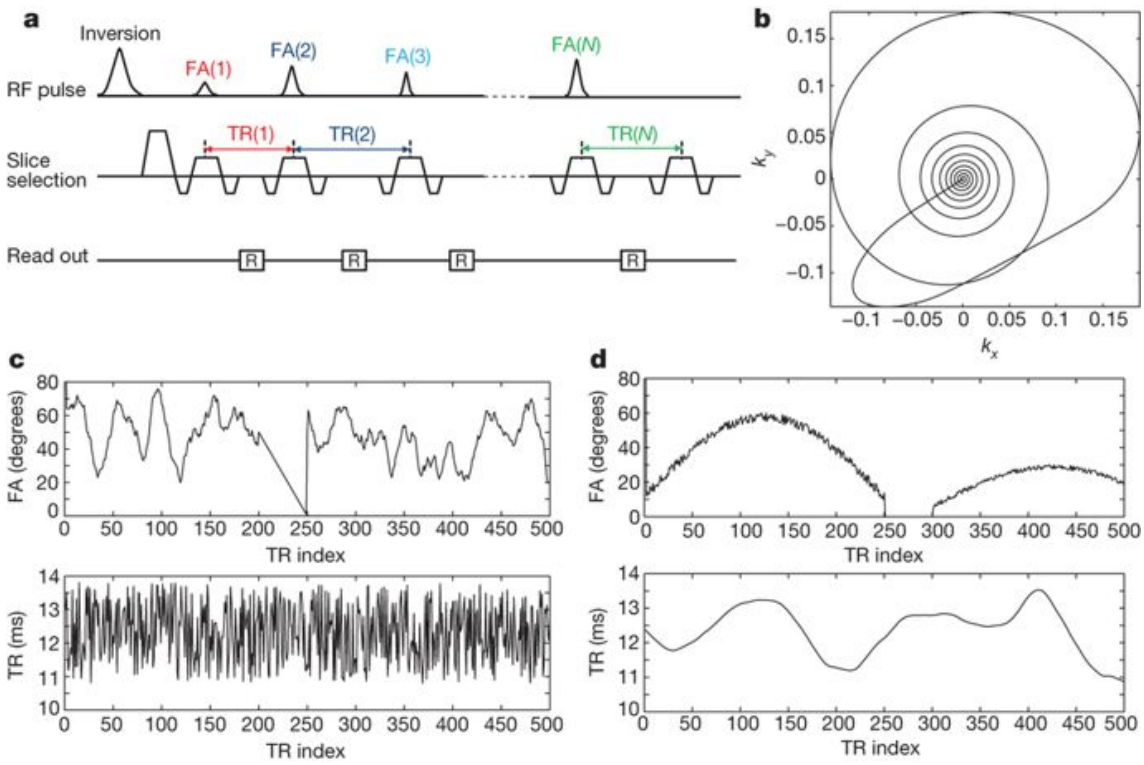

Figure 2.15: Sequence originally proposed for the first published MRF implementation. A bbsfp or TrueFISP sequence is used a) in combination with a variable density spiral b). Two different flip angle and TR patterns are proposed in c) and d). Image taken from [Ma13].

MR Fingerprinting Using Fast Imaging with Steady-State Precession (FISP) with Spiral Readout

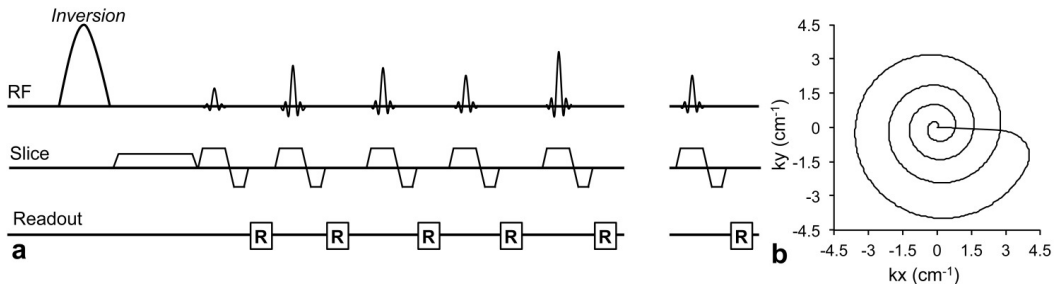

Figure 2.16: Sequence proposed for the FISP MRF implementation. a) shows the FISP like sequence diagram with unbalanced slice selective gradient and b) the used variable density spiral. Image taken from [Jia15]

.

To overcome the problem of banding artifacts in bssfp based MRF, an MRF implementation based on ssfp or FISP was developed (Figure 2.16) [Jia15]. The slice selective gradient is unbalanced in

this implementation, which makes it less sensitive to off-resonances but it also has lower SNR and is less sensitive to T_1 and T_2 compared to the bssfp based MRF implementation. It should be noted that in contrary to the original publication, 3000 pulses instead of 1000 were employed for the following experiments [Jia16b]. The flip angles and repetition times used are depicted in Figure 2.17.

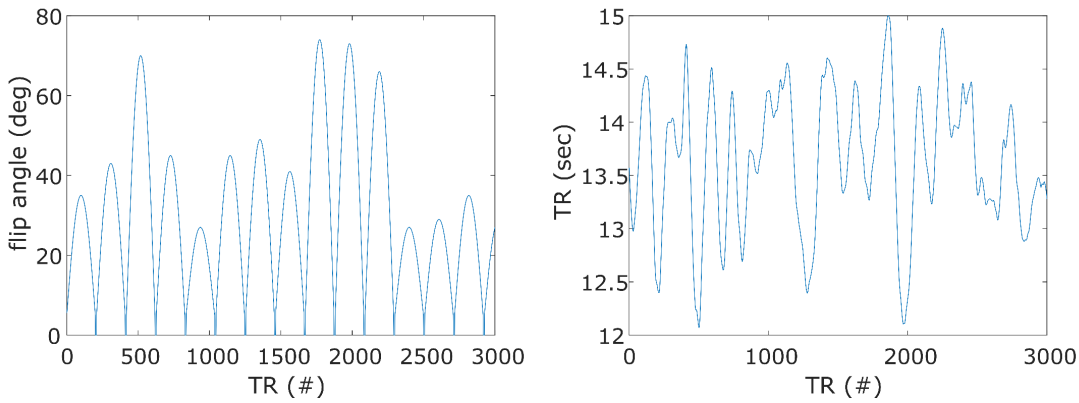

Figure 2.17: Flip angles and repetition times used for the 3000 pulses variant of FISP MRF.

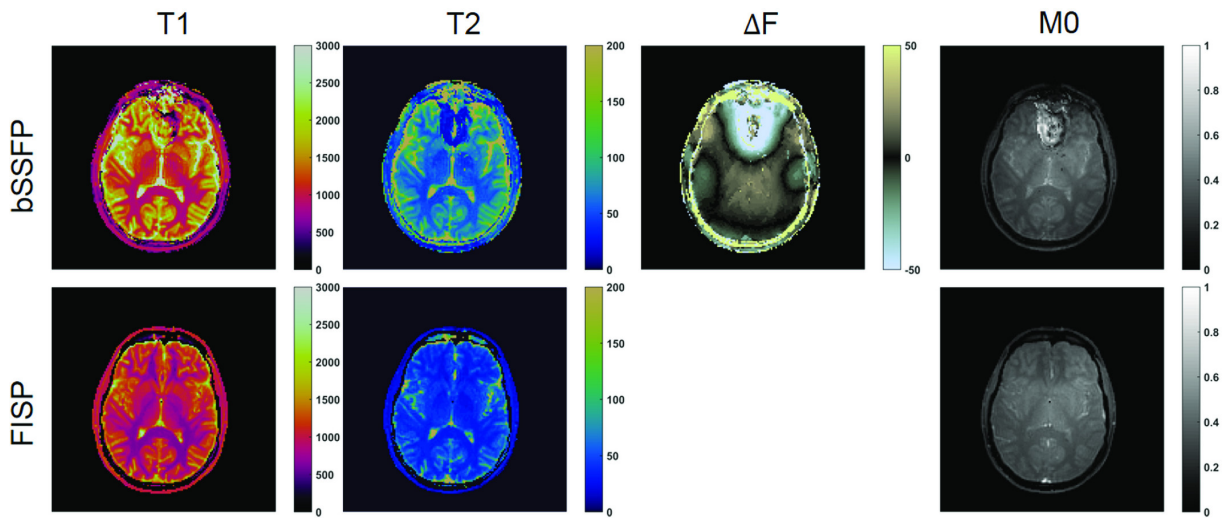

Figure 2.18: A comparison of parameter maps in the same slice from the original bssfp MRF and the FISP based MRF are shown. In the frontal region strong artifacts on both the T_1 and T_2 map due to off-resonances can be observed in the bssfp version. Image taken from [Bip18]

.

A comparison of parameter maps generated by FISP-MRF and the original TrueFISP based MRF is shown in Figure 2.18.

Other MRF implementations

Several MRF techniques simultaneously quantify other parameters than T_1 and T_2. Methods exist, that aim to simultaneously quantify the transmit RF field B_1^+. In one implementation [Buo16] a solely FISP based acquisition is used where a block of high ($> 90^\circ$) flip angles are applied at the end of the acquisition. These blocks generate oscillations of the magnetization and their frequency is proportional to the B_1^+ field. One downside of the method is that these oscillations have high frequencies, similar to those of the undersampling artifacts because of the high undersampling factors employed in MRF. This approach was therefore proposed in combination with a Cartesian sampling pattern. Later on a spiral based approach at a field strength of 7T was proposed [Buo17] where a substantial share of the acquisition generates these B_1^+ dependent oscillations.

Another approach [Clo16] tries to simultaneously quantify T_1, T_2 and B_1^+ using a segmented acquisition and a transmit coil that can operate in two different modes. With the help of the spatially complementary transmit coil modes, a higher degree of B_1^+ homogeneity can be achieved. Instead of a continuous acquisition, a segmented acquisition was proposed, where within each segment either a FLASH or FISP sequence is used and the coil modes vary from pulse to pulse or are constant over one segment. This method is promising under the condition of B_1^+ voids that can appear at high field strengths (B_0 >3T) and near metallic implants.

Other effects that can be simultaneously matched with specialized MRF implementations sensitized to the specific effects are among others diffusion [Jia16a], magnetization transfer [Hil17], chemical exchange [Ham15a] or blood flow [Su17].

MRF can also be applied as an ECG triggered sequence [Ham17] for quantification of cardiac tissues. Since time constraints are imposed by the heart rate, inversion and T_2 preparation modules are applied to rapidly generate signals that are sensitive to T_1 and T_2. MRF has been adapted to work in several body parts, such as abdomen [Che16], breast [Che19] or prostate [Yu17a]. The versatility of MRF has been demonstrated in MRF-Music [Ma16]. Here the imaging gradients are played out in a specific way to produce music, while meaningful parameter maps can still be generated.

Volumetric MRF

To rapidly acquire volumetric parameter maps with MRF, two basic approaches have been proposed. One is the simultaneous multislice technique (SMS) where two slices are excited simultaneously such that the signals from the slices are as orthogonal as possible. The signal is matched to two dictionaries to jointly estimate the parameter maps of both slices [Jia17].

Another way is to excite a whole volume using either a non-selective or slab-selective pulse and

to use a phase encoding gradient along the third dimension [Ma17b]. The acquisition can also be sped up by using parallel imaging such as GRAPPA or SENSE, along z-direction.

Reconstruction Algorithms and Optimization of MRF

Techniques to simulate a dictionary are Bloch simulation and the extended phase graph formalism. For a given MRF sequence the dictionary has to be computed once and can be stored and used for reconstructions of all measurements that were carried out with the exactly same sequence. MRF dictionaries can easily become very large and grow exponentially with the number of parameter dimensions. An important task in MRF simulations is to find out which effects contribute to the signal evolution and have to be incorporated. For 2D implementations, the slice profile has to be considered which affects the accuracy of produced maps [Ma17a]. It describes the effect of a selective pulse on a slice or slab. The actual magnetization depends on the position within the slice or slab. The B_1^+ magnitude can be simulated as a scaling factor of the flip angles and off-resonances are simply rotations of spins.

To perform a fast matching process of acquired signals to the dictionary, the signals can be compressed along the time dimension to save storage space as well as to decrease the computational effort for the matching process. One popular method for performing this is the singular value decomposition (SVD) [McG14], which projects the measured and simulated fingerprints to a lower-dimensional subspace.

The reconstruction process can be formulated as an inverse problem. Two out of many examples for implementing this are accelerated iterative reconstruction MRF (AIR-MRF) [Cli17] and "maximum likelihood reconstruction for magnetic resonance fingerprinting" [Zha16]. In AIR-MRF, the reconstruction is formulated as

$$\min_{X} \quad ||Y - G(X)||_2^2 \tag{2.76}$$

Where Y is the measured k-space data, X the estimated images (restricted to the fingerprints in the dictionary) and $G(X)$ an operator consisting of the sampling function, the Fourier transform and the coil sensitivities. The estimated images are iteratively updated by minimizing the difference of estimated images X and acquired k-space data Y.

In the "maximum likelihood reconstruction for magnetic resonance fingerprinting" method, the tissue properties are estimated from a similar model. In contrast to the iterative approach, the alternating direction method of multipliers (ADMM) [Boy11] and the variable projection method (VAPRO) [Hal07] are used to solve the underlying minimization problem.

The optimization of MRF is a very complex and highly computationally demanding task since MRF sequences have a lot of degrees of freedom. Several works approached the problem, e.g. by using the Cramer Rao bound [Bo 16] or Monte-Carlo based sequence simulations [Som17].

3. Influence of Undersampling on Magnetic Resonance Fingerprinting

In this chapter, the basic assumption underlying MRF that a spatial undersampling scheme leads to incoherent aliasing artifacts in the time domain is investigated. The pattern matching process is assumed to be unaffected by these artifacts [Ma13]. Originally, a simple ascending reordering was used for MRF. Here, a limited number of spirals n is generated by rotating an initially designed spiral. For every data acquisition, the spiral is rotated by an angle $\alpha = \frac{360°}{n}$ [Ma13, Jia15, Che16]. Other MRF implementations use a golden-angle increment for rotation of the spirals [Ham17, Buo17]. To improve the parameter map quality, the MRF data can also be reconstructed using iterative or low-rank methods [Zha16, Ass18, Cli17, Pie16].
The presented work aims to study the effect of spiral interleave order on aliasing artifacts and resulting quantitative maps in a FISP-MRF implementation applying single shot spiral sampling. Experiments were performed on phantoms and compared to results from numerical simulations. With insights gained and further theory derived from these experiments, in-vivo spiral FISP-MRF measurements in the human brain could be significantly improved, compared to the originally proposed ascending order of spirals. The content of this chapter has previously been published as a journal article [Kör19b]. Verbatim copies of text passages are marked with quotation marks.

3.1 Methods

"For all simulations and experiments in this work, a prototype FISP-MRF implementation, based on the signal encoding scheme from Jiang et al. [Jia15], was used. This implementation is briefly described in the following section.
After the application of an adiabatic inversion pulse, a train of slice selective RF pulses with varying flip angles and repetition times (TR) is applied." In each TR one image is encoded with a short spiral read-out of approx. 6 ms, resulting in a series of strongly undersampled images.
"For the experimental and theoretical investigations in this work, a train of 3000 RF pulses was

used. A base TR of 12 ms was chosen with an additional TR increment changing from echo to echo as in [Jia15]. Two different spiral trajectories were used to sample the two-dimensional k-space, one with a dual-density design [Mey11] and the other one with constant density. The dual-density spiral was designed for a field of view of 300mm, a matrix size of 256 and an undersampling factor of 24 in the center of k-space with a transition to 48 in the peripheral regions of k-space. A constant-density spiral was designed for a FOV of 400 mm and a matrix size of 352 with a constant undersampling factor of 48. Spiral trajectories were corrected using the generalized eddy-current model by Tan and Meyer [Tan09].

In order to produce undersampling artifacts varying in the time domain, 48 spiral interleaves were generated that are rotated versions of the original spiral interleaf. Each of the 48 spiral interleaves is rotated by an angle $\phi = i \cdot 360/48°$ against the original spiral interleaf ($i = 0$), where $i \in \{0; 1; \ldots .; 47\}$ denotes the index of the spiral interleaf.

To constrain the problem, focus was placed on recurrent interleaf reordering (ILR) patterns with the length of 48. The straight forward approach is to use a simple ILR such as [0;1;2;. . . .;47] which is called ascending mode, or similarly the descending mode [47;46;45;. . . .;0]. Furthermore, it is possible to define interleaf reorderings, which apply an index increment of consecutive spirals. These are called STEP-x ILRs, with x denoting the index increment of consecutive spirals. For example, STEP-1 is identical to ascending mode which was proposed in the original MRF implementations [Ma13, Jia15], STEP-2 is $[0; 2; 4; 6; \ldots]$, and STEP-24 is [0;24;1;25;. . .]. The index is incremented by 1 when a previously used interleaf index is reached, in order to use all indices. As an additional parameter, the starting index (ILR offset) of the first spiral interleaf that is played out was varied.

'Sinc' shaped RF pulses with a time-bandwidth product of 8, duration of 2000 ms and a slice thickness of 5 mm were used for excitation except for the adiabatic inversion pulse. To mitigate the influence arising from inhomogeneities of the transmit RF field B_1^+ [Buo16, Gao15], a B_1^+ correction was applied. Here a B_1^+ prescan [Chu10] was acquired and the relative B_1^+ value determined a subdictionary for the matching process, calculated with the corresponding relative B_1^+. This method is similar to previously reported prescan based B_1^+ corrections for MRF [Ma17a, Che16]" and described in more detail in the following chapter.

"The impact of the different sampling trajectory implementations on MRF parameter maps can be investigated by performing simulations using the spatial response function (SRF) [Dyd00]. While the point spread function describes how signal from one pixel is distributed to other pixels, the SRF describes how signal in one pixel is collected from other pixels. Each pixel's signal was computed by multiplying the signal map and the pixel's SRF. A two-dimensional digital phantom

incorporating a B_1^+ map and coil sensitivities derived from a scan of a real phantom was used, neglecting other possible influences on the signal. The real phantom was an oil-filled sphere to minimize dielectric effects on the transmit field. MRF scans were acquired with both spiral trajectories and different spiral interleaf reorderings and compared to the corresponding simulated MRF parameter maps. All data were acquired on a 3 T whole-body scanner (MAGNETOM Skyra, Siemens Healthcare, Germany).

STEP-x spiral ILRs were also tested on a human head-shaped phantom filled with agarose. The signals resulting from the experiments were compared to the non-undersampled signal, which was approximated as the fingerprint with the mean T_1 and T_2 relaxation times over the phantom. A subtraction of the measured signal from the best-matching dictionary entry yielded the residuals for every pixel caused by aliasing. Since the spiral reordering was repeated every 48 echoes, the residuals can be divided into segments, each 48 time points long and plotted one above the other. This procedure was done for several ILRs, and the mean value over the segmented residuals of each ILR was calculated. A Fourier transform of the mean of the segmented residuals reveals their frequency composition. Rearranging the mean of the segmented residuals by index of the spiral interleaf leads to spiral-interleaf-specific aliasing noise rather than temporal aliasing noise.

Furthermore, the mean residual per spiral interleaf for each pixel can be rearranged in a specific order similar to the STEP-x patterns, which leads to an artificial residual pattern. This approach provides an easier means for analyzing the characteristics of residuals without the need for measuring with different spiral ILRs. Frequency analyses of these artificial residual patterns were carried out for all STEP-x ILRs, and a score for estimating the effects on pattern matching was introduced. The sum of squares over the pairwise differences of the spectra of fingerprints was taken on the exhaustive dictionary. The result characterizes the fingerprints' frequencies contribution to the encoding of tissue parameters. This spectrum was used as a weighting function for the spectra of the residuals. The residuals' frequencies are thus weighted according to their contribution to the encoding of tissue parameters. The hypothesis underlying this score is that residuals consisting of different frequencies than the ones contributing to the encoding of tissue parameters have a vanishing correlation with all dictionary atoms, whereas other frequency residuals potentially distort the signal in a way that the pattern matching results are biased.

A further experimental criterion for evaluating the effects of a reordering mode upon spatial biases is to compare two parameter maps from acquisitions with the same reordering mode. The two acquisitions differ only in the starting point of their reordering. One starts at index n and the other one at n + 24, yielding maximum phase difference of residuals. Resulting difference maps should be zero if the reordering scheme is well suited i.e. the result does not vary in spatial position.

ILR schemes were tested and evaluated regarding the criteria described above. The pattern performing best was also tested in vivo on a volunteer brain and compared to the conventional STEP-1 ILR schemes. The data from in vivo acquisitions were also reconstructed using AIR-MRF [Cli17], a method for iterative reconstruction of MRF data that employs fingerprint compression, additional spatial regularization and FLANN [Muj09, Muj14], an accelerated dictionary search methods. One tree was used for FLANN, leaves to check was set to 512 and ten iterations were used for AIR-MRF."

3.2 Results

"Figure 3.1 displays resulting parameter maps from simulated spiral MRF in the oil-filled sphere. For comparison, the parameter maps from real MRF experiments on the phantom are also

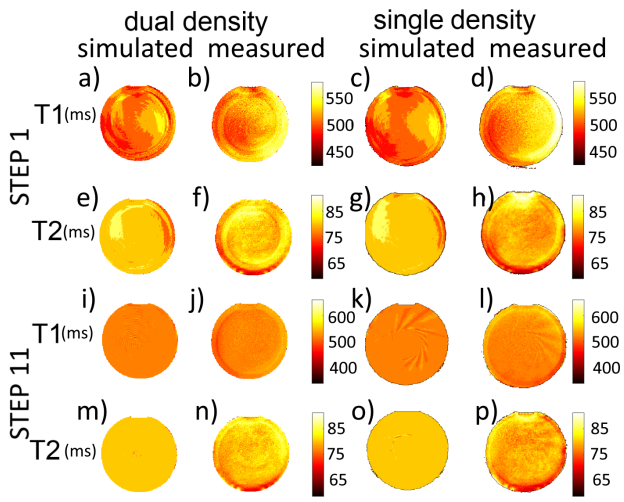

Figure 3.1: Parameter maps of an oil-filled sphere calculated from simulated and measured MRF acquisitions. Left side shows results for the dual-density spiral, right side for the constant-density spiral. a) b) c) d) are T_1 maps from ascending (STEP-1) reordering mode and e) f) g) h) the respective T_2 maps. i) j) k) l) are T_1 maps from STEP-11 reordering mode and m) n) o) p) the respective T_2 maps. Image taken from [Kör19b].

depicted in this figure. With ILR STEP-1, shading (i.e. spatially smoothly varying results) can be observed in parameter maps, especially the T_1 maps, with both spiral variants. When using the ILR STEP-11, this effect is largely mitigated. The T_1 maps acquired using a single-density spiral and ILR STEP-11 show a remarkable spiral-like pattern, which can be reproduced with the simulations. Shading is also visible in the T_2 maps, but since T_2 map errors are also influenced strongly by B_1^+ inhomogeneities [Che16, Buo16, Gao15] and noise, they are harder to reproduce

by simulation. Nevertheless, the artificial T_2 maps from simulations show a similar pattern to those from MRF experiments.

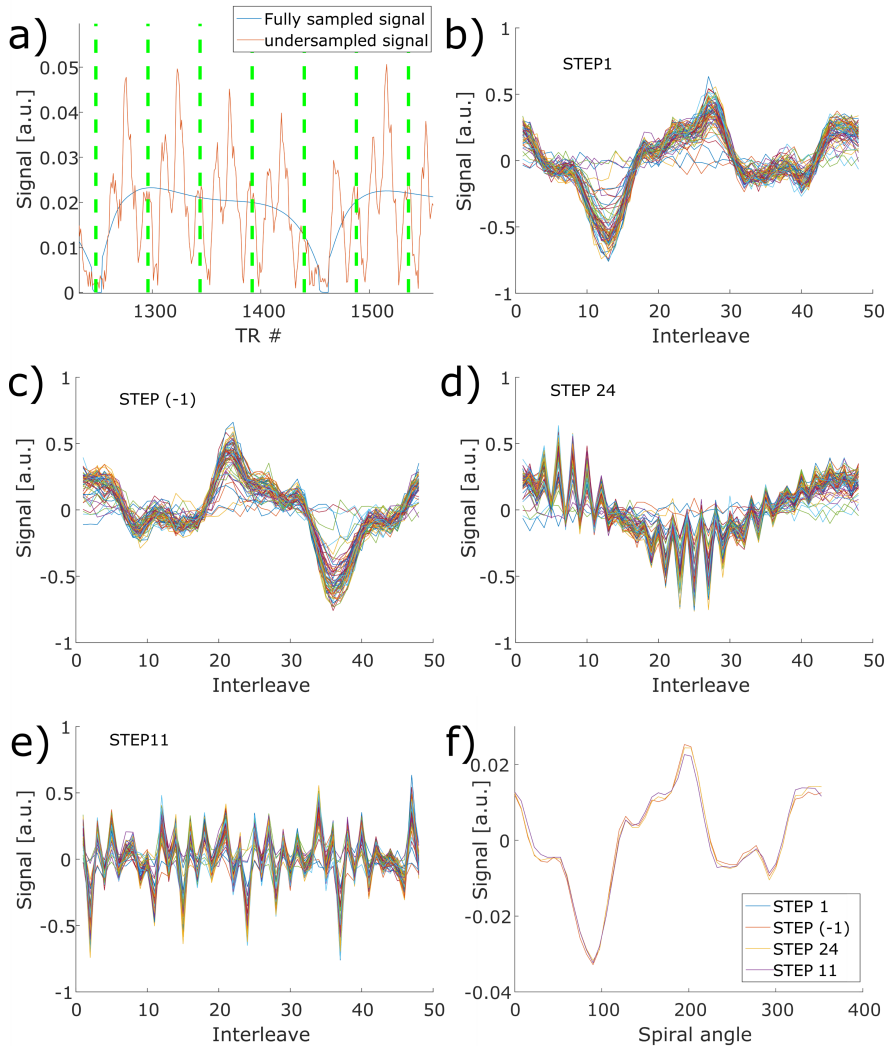

Figure 3.2: a) True (fully sampled) and measured undersampled signal from one pixel (excerpt of the whole temporal signal course). Dashed green vertical lines are shown every 48 echoes. The subtraction of measured and true signal, which is the residual is divided in these sections. In each of these sections the Reordering is the same. b) to e): Residuals from subtracting true and measured signals for several reorderings. Since the reorderings are recurrent, residuals are plotted one above the other. For simplicity, only the real part of the residuals is shown here; a similar behavior can be observed for the imaginary part. b) ascending (STEP-1) reordering, c) descending (STEP-(-1)) reordering, d) alternating (STEP-24) and e) STEP-11 reordering. f) shows the mean real value of the 48-time-point-long residuals for each reordering. The residuals are plotted against the spiral interleaf angle. Image taken from [Kör19b].

Results from subtracting true and measured signal are exhibited in Figure 3.2. Figure 3.2 a) illustrates how this is carried out in detail. One pixel in the phantom was analyzed using acquisitions with different interleaf reordering schemes (Figure 3.2 b) - e)). The residuals were reordered by index of the spiral interleaf instead of a temporal order, and the mean residual for each spiral interleaf was calculated (Figure 3.2 f)). These spiral-interleaf-specific mean residuals from MRF acquisitions with different ILR schemes deviate very little from each other.
Calculating a pixel-specific mean residual curve was repeated for all pixels in the phantom. Since this mean is independent of the reordering scheme and mainly depends on the spiral interleaf, the mean residual curve of each pixel can be rearranged by ILR patterns. A Fourier analysis of the artificially reordered residuals reveals the 'residual spectra' (Figure 3.3 a)). Weighting the resulting spectrum by a function that reflects which frequencies contribute to the encoding (Figure 3.3 b)) gives a metric that is called weighted frequency score. Frequencies are weighted according to their contribution to the encoding of tissue parameters. The resulting mean score of all pixels within the phantom for STEP-x interleaf reorderings is depicted in Figure 3.3 c).

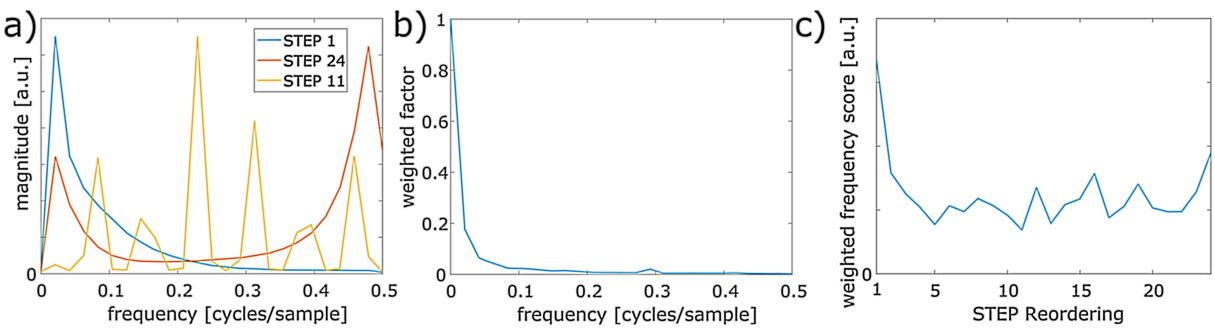

Figure 3.3: a) Mean frequency spectrum of residuals from all pixels in the phantom from ascending (STEP-1), alternating (STEP-24) and STEP-11 reorderings. b) Function used for weighting the frequency spectrum of the residuals. c) Mean of weighted frequency score over residuals from all pixels in the phantom. Residuals were computed by reordering the sum of residuals according to STEP patterns. Weighted frequency score for STEP-1 to STEP-24 reorderings is shown. Higher values indicate that residuals have a relatively high amount of low-frequency components. STEP-11 turns out to be the best STEP reordering, based on this measure. Image taken from [Kör19b].

The findings can be transferred to MRF measurements of the human brain. Parameter and difference maps are depicted in Figure 3.4. STEP-11 parameter maps with offset 0 and 24 and the corresponding difference maps exhibit almost no spatial biases, whereas both STEP-1 difference maps show a strong bias that is rotated with ILR offsets. With AIR-MRF the artifacts when using STEP-1 are significantly reduced compared to the conventional reconstruction. STEP-11 acquisitions with AIR-MRF exhibit the smallest difference between offset 0 and 24. T_1 values of

all parameter maps in four ROIs in the brain, and corresponding T_2 values are displayed in Table 3.1."

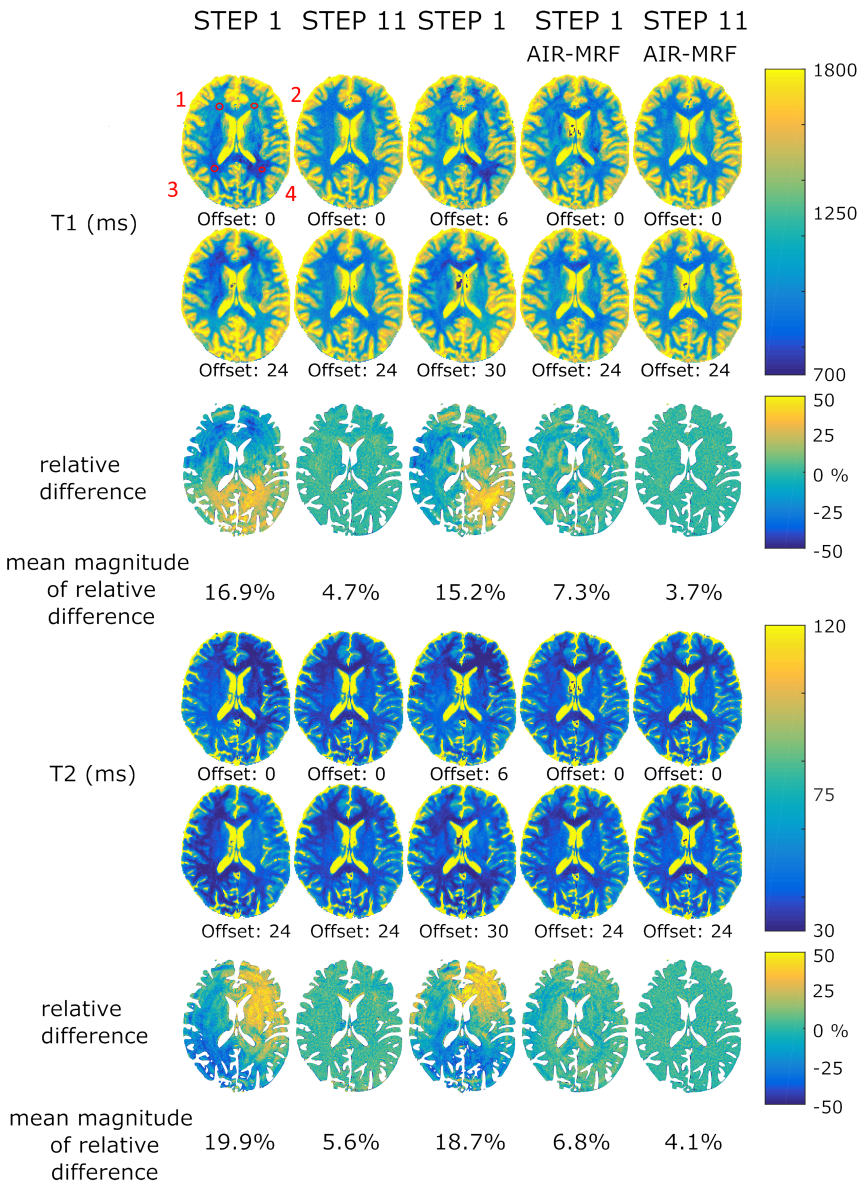

Figure 3.4: MRF parameter maps and difference maps from dual density spiral MRF acquisitions using different ILR reorderings. T_1 maps and the corresponding T_2 maps are shown for different reorderings and offsets with and without AIR-MRF reconstruction,Respective shading maps, i.e., difference of the two parameter maps are shown for non fluid parts of the brain in the same column, together with the mean magnitude of the relative differences. Image taken from [Kör19b].

T_1	T_1 in ROI 1 $[ms]$	T_1 in ROI 2 $[ms]$	T_1 in ROI 3 $[ms]$	T_1 in ROI 4 $[ms]$
STEP-1 offset 0	1033 ± 66	1127 ± 45	825 ± 37	779 ± 26
STEP-1 offset 24	769 ± 27	816 ± 37	1082 ± 43	1062 ± 32
STEP-11 offset 0	897 ± 35	916 ± 45	934 ± 43	887 ± 33
STEP-11 offset 24	884 ± 31	906 ± 32	958 ± 28	903 ± 26
STEP-1 offset 6	961 ± 41	917 ± 38	971 ± 35	755 ± 42
STEP-1 offset 30	877 ± 32	825 ± 44	911 ± 29	1135 ± 28
STEP-1 offset 0	948 ± 42	921 ± 40	964 ± 40	922 ± 42
STEP-1 offset 24	877 ± 41	906 ± 25	949 ± 45	872 ± 21
STEP-11 offset 0	895 ± 37	903 ± 28	946 ± 31	919 ± 28
STEP-11 offset 24	903 ± 30	893 ± 29	950 ± 27	943 ± 33
T_2	T_2 in ROI 1 $[ms]$	T_2 in ROI 2 $[ms]$	T_2 in ROI 3 $[ms]$	T_2 in ROI 4 $[ms]$
STEP-1 offset 0	35 ± 1.9	32 ± 2.2	43 ± 2.6	33 ± 2.3
STEP-1 offset 24	30 ± 1.3	40 ± 2.6	32 ± 1.5	37 ± 1.5
STEP-11 offset 0	32 ± 1.7	33 ± 1.9	37 ± 1.9	37 ± 2.1
STEP-11 offset 24	32 ± 1.4	33 ± 1.7	37 ± 1.6	37 ± 1.6
STEP-1 offset 6	33 ± 2.9	28 ± 2.2	44 ± 1.6	39 ± 3.3
STEP-1 offset 30	34 ± 1.2	39 ± 1.5	33 ± 2.2	34 ± 1.5
STEP-1 offset 0	34 ± 2.0	34 ± 1.5	37 ± 1.5	39 ± 1.5
STEP-1 offset 24	33 ± 1.9	36 ± 1.8	38 ± 1.9	36 ± 1.5
STEP-11 offset 0	33 ± 2.1	33 ± 1.3	37 ± 2.0	37 ± 1.4
STEP-11 offset 24	34 ± 1.8	33 ± 1.4	37 ± 1.7	38 ± 2.0

Table 3.1: Relaxation parameter values in the four ROIs in the brain as shown in Figure 3.4.

3.3 Discussion

"Parameter maps of the oil-filled sphere resulting from simulations show similar spatial biases as the actual measured maps. This result demonstrates that the biases in MRF parameter maps are mainly influenced by the reordering of aliasing artifacts rather than other potential factors, such as signal deviations by eddy currents, which were not incorporated in the simulation.

The residuals of different reorderings in the phantom experiment are repetitive: when reordering the mean of the segments per ILR by spiral interleaf index, almost the same curves are generated for the four ILR patterns tested on the phantom. Within the scope of the experiments presented in this work, the spiral-interleaf-specific residuals dominate all other sources of signal errors and are almost uninfluenced by ILR patterns.

Comparing these results to the weighted frequency score (Figure 3.3) of the STEP-x reorderings reveals that the occurrence of spatial biases in parameter maps in the homogeneous phantom corresponds to the frequency spectrum of the aliasing artifacts. For this phantom, the best STEP-x reordering was found to be STEP-11. This reordering also produces the residuals with the fewest

frequencies contributing to the encoding of tissue parameters. This finding can be explained by considering the design of the fingerprints. The signal in FISP-MRF is designed to vary slowly and subsequently to have a low frequency. High-frequency residuals as produced by the STEP-11 scheme exhibit a lower correlation with the dictionary atoms as compared to the low-frequency residuals produced by STEP-1. This finding is similar to a study where spiral interleaves were reordered to minimize the influence of motion on dynamic imaging [Tsa06]. In this work, spiral interleaves were reordered, such that the alias-free region of the PSF is effectively enlarged for low and intermediate frequencies while sacrificing the high frequency alias-free regions.

Strong biases occur mainly in T_1 maps. As the MRF sequence applies an inversion pulse in the beginning, the sensitivity to T_1-related signal changes is very high in this early phase of the experiment. In an intuitive picture, a shift of residuals with low frequency and with a distinct minimum may cause a shift in time of the first zero crossing of the transversal magnetization and therefore significantly affect the T_1 match. Whether the effect appears depends on the signal time course itself but also on the spatial location, which explains the observed artifact patterns within the object.

The findings in the homogeneous phantom were transferable to in-vivo brain measurements. A pronounced spatial bias with the STEP-1 reordering can be mitigated with other STEP ILR schemes, where STEP-11 is giving the best results. This finding was confirmed by calculating difference maps: the map for the STEP-11 pattern has zero mean with low variation. Nevertheless, the effects of undersampling artifacts strongly depend on the underlying structure and in more complex body parts a different ILR pattern might be favorable.

Ideally, an optimized reordering scheme enables the generation of unbiased parameter maps with a simple and fast template matching algorithm, even if the signal is severely affected by k-space undersampling. More sophisticated reconstruction methods such as iterative reconstruction [Cli17, Pie16] or low rank methods [Ass17, Zha16] can minimize the spatial biases caused by undersampling artifacts. These types of methods can also benefit from optimized reordering schemes which could result in faster convergence and a substantial improvement of iterative methods that rely on pattern matches. However, it should be noted that reconstructions formulated as inverse problems do not necessarily have to be biased similarly as the simple pattern matching, as has exemplarily been shown in this work for AIR-MRF. Differences in convergence are expected and potentially other ILR patterns might be better suited than the one found in this study.

This investigation does not cover the golden ratio reordering scheme that is used in a variety of MRF implementations [Buo17, Ham17], especially in those employing radial sampling [Clo16, Ass17]. However, a golden ratio reordering would correspond to a STEP $\approx$14.83 scheme, which is

very similar to STEP-15. Accordingly, it is not expected to provide significantly different results than the repetitive integer STEP reordering schemes investigated in this work. Nevertheless, golden angle reordering schemes also provide substantially better results than the originally proposed ascending reordering.
MRF can be implemented in various ways [Clo16,Che16,Ham17,Buo16,Ass17,Ye18,Kör18c] and a general solution to the optimization of MRF sequences [Bo 16] always has to be combined with the optimization of the sampling scheme. Insights gained in this work are nevertheless applicable to implementations of the fingerprinting concept with fingerprints that have similar frequency spectra and are expected to remain valid when using dictionary compression methods such as SVD compression [McG14]. The combination of low frequency signals and high frequency artifacts that was found to be favorable in this work is only a special case of the general problem to design signals and artifacts with different spectra. Future work is necessary to examine fingerprints with different spectra."

3.4 Conclusion

"When applying rigorous undersampling of k-space in MRF, it is an essential and non-trivial task to ensure stable, bias-free results, which are not affected by the sampling pattern. It was shown, both by simulation and experiment, how an inadequate spiral interleaf reordering pattern will introduce a spatial bias to the MRF parameter maps. Investigating basic properties of the temporal interleaving scheme leads to objective criteria to identify the most appropriate sampling pattern, which was demonstrated in phantom and human-brain experiments."

4. Influence of Field Inhomogeneities on Magnetic Resonance Fingerprinting

In this chapter, the influence of inhomogenous B_0 and B_1^+ fields on FISP-MRF is investigated. Spatial distributions of B_0 and B_1^+ depend on several factors and can in general not be assumed to be homogeneous throughout an imaged object (e.g. because of electric susceptibility). Furthermore shim coils as well as transmit coils need to be calibrated before actual MRI experiments to yield the desired B_0 and B_1^+. Calibration scans are usually optimized for speed so that the results can vary in certain limits. Therefore, B_0 and B_1^+ distributions can be different in the same object on different scanners and even on the same scanner from scan to scan. A dependency of FISP-MRF results on B_0 and B_1^+ would accordingly impair both reproducibility and accuracy and needs to mitigated.

4.1 Influence of B_1^+ on Magnetic Resonance Fingerprinting

A common effect in Magnetic Resonance Imaging is the spatial variation of the RF transmit field (B_1^+). Such variation can introduce systematic errors in MRF results [Ma17a]. The B_1^+ field effectively scales the applied flip angles and thereby alters the generated signal evolution's time course. A simple scaling of the generated signal would however have no effect on the pattern match results.

4.1.1 Mitigation of the Influence of B_1^+ on Magnetic Resonance Fingerprinting Results with an External B_1^+ map

A straightforward approach to account for the inhomogeneity of the B_1^+ field is the acquisition of a B_1^+ map before or after the actual MRF experiment. The data of this map can then be used for the voxelwise selection of an associated subdictionary in B_1^+-dimension for the matching process. These subdictionaries are calculated for a range of relative B_1^+ values.

4.1.1.1 Methods

The FISP-MRF method was preceded by a low-resolution B_1^+ map measurement. The B_1^+ map [Chu10] covers a volume of 420 * 450 * 450 mm^3 with a resolution of $7mm * 7mm * 8mm$. The acquisition of the B_1^+ map with these parameters takes approximately 22 seconds. Multiple slices are acquired and bicubic interpolation is performed to generate B_1^+ information for the high-resolution MRF acquisitions. The B_1^+-prescan is acquired only once and can be accessed by any succeeding MRF measurement. Multiple subdictionaries considering different relative B_1^+ values ranging from 60% to 140% in 1% steps were generated. Singular-value decomposition in the time domain was carried out in order to limit the size of the dictionary [McG14]. During the matching process, for each voxel a subdictionary with the previously measured relative B_1^+ value of this voxel was selected.
Based on the subdictionaries in B_1^+ dimension, the theoretical impact of B_1^+ inhomogeneity was evaluated. Fingerprints with a certain T_1/T_2 combination from a subdictionary simulated with relative B_1^+ values of 70% to 130% in 5% steps were matched to the subdictionary with $B1^+ = 100\%$. The percental T_1/T_2 value differences of the matched to the real values for every T_1/T_2 combination in the dictionary and the different relative B_1^+ values were calculated. A linear fit to the resulting percental deviations along relative B_1^+ was performed for each T_1/T_2 combination in the dictionary.
The effect of B_1^+ on experimental MRF results and the correction with the prescan method were demonstrated in measurements. The T_1 and T_2 layer of the NIST/ISMRM phantom (Figure 4.1) and three slices of a human brain were scanned with and without applying the B_1^+ prescan based correction method. In the phantom experiments, the relative B_1^+ was furthermore altered by manipulating the transmit coil gains by $\pm 20\%$. All scans were performed on a commercial scanner (MAGNETOM Skyra 3T, Siemens Healthcare, Erlangen, Germany).

4.1.1.2 Results

Figure 4.2 displays the slope of the linear fits to relative T_1 and T_2 deviations of matching fingerprints simulated with different B_1^+ to the dictionary with $B_1^+ = 100\%$. For most dictionary entries a very small positive slope in T_1 was found. T_1 values originating from a voxel with $B1^+ > 100\%$ are overestimated except for fingerprints with small T_1 ($<$ 500ms) and T_2 ($<$ 10ms). The response of T_2 to B_1^+ changes is the other way round. For most species in the dictionary, T_2 values originating from a voxel with $B1^+ >$100% will be underestimated, except for some species with very low T_2 ($<$ 10 ms). Besides the reversed slope sign, the effect of B_1^+ is higher on T_2 than T_1.

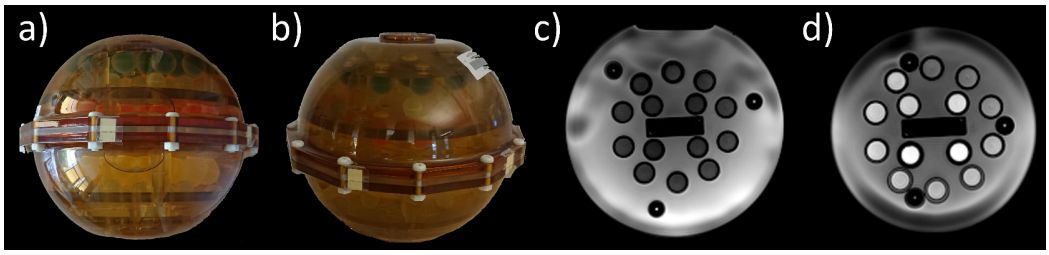

Figure 4.1: Two views (a) and b)) of the NIST/ISMRM system phantom used in the experiments. The spherical phantom consists of several plastic plates (layers) with mounted spheres. The spheres contain different solutions with distinct T_1 and T_2 values. Two layers, the T_1 (green spheres) and the T_2 layer (red spheres) were scanned. The T_1 values are logarithmically spaced in the T_1 layer and T_2 values are logarithmically spaced in the T_2 layer. c) shows a proton density weighted slice through the T_2 layer and d) through the T_1 layer.

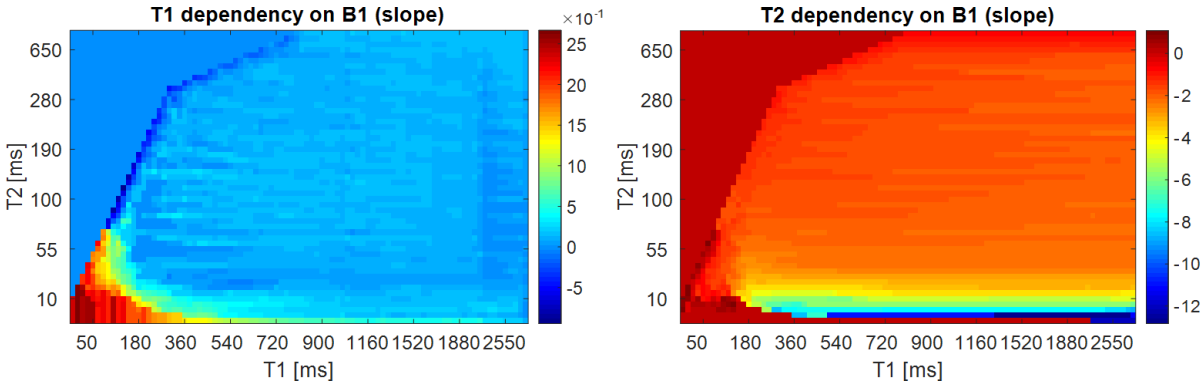

Figure 4.2: Dependency of T_1 (left side) and T_2 (right side) results on B_1^+ in MRF. The values shown in the plot are the slopes from fits to the rel. parameter deviations from matching signals with different relative B_1^+ to the dictionary with 100% B_1^+. The parameter values are not equally spaced since the dictionary from the FISP-MRF publication [Jia15] was used. Here, T_1 and T_2 resolution vary.

Figures 4.3 and 4.4 show measured B_1^+ and T_1 values in 14 spheres in the T_1 array as well as the measured B_1^+ and T_2 values in the 14 spheres of the T_2 array of the NIST phantom. The experimental results are in agreement with the findings from the simulations. Only a slight positive correlation of the T_1 values to B_1^+ in the NIST phantom was observed. The correlation of T_2 to B_1^+ is negative and stronger than for T_1. When using the prescan based correction the T_1 and T_2 values are similar for different B_1^+ settings. In spheres with $T_1 < 400$ ms a deviation to the nominal values remains with the B_1^+ prescan.

Figure 4.5 shows acquired B_1^+ maps in three slices in the brain of a volunteer. A strong variation of B_1^+ in the slices and between slices of up to 50 % can be seen. T_1 maps resulting from the corresponding MRF measurement are shown on the left side, both with and without B_1^+ correction

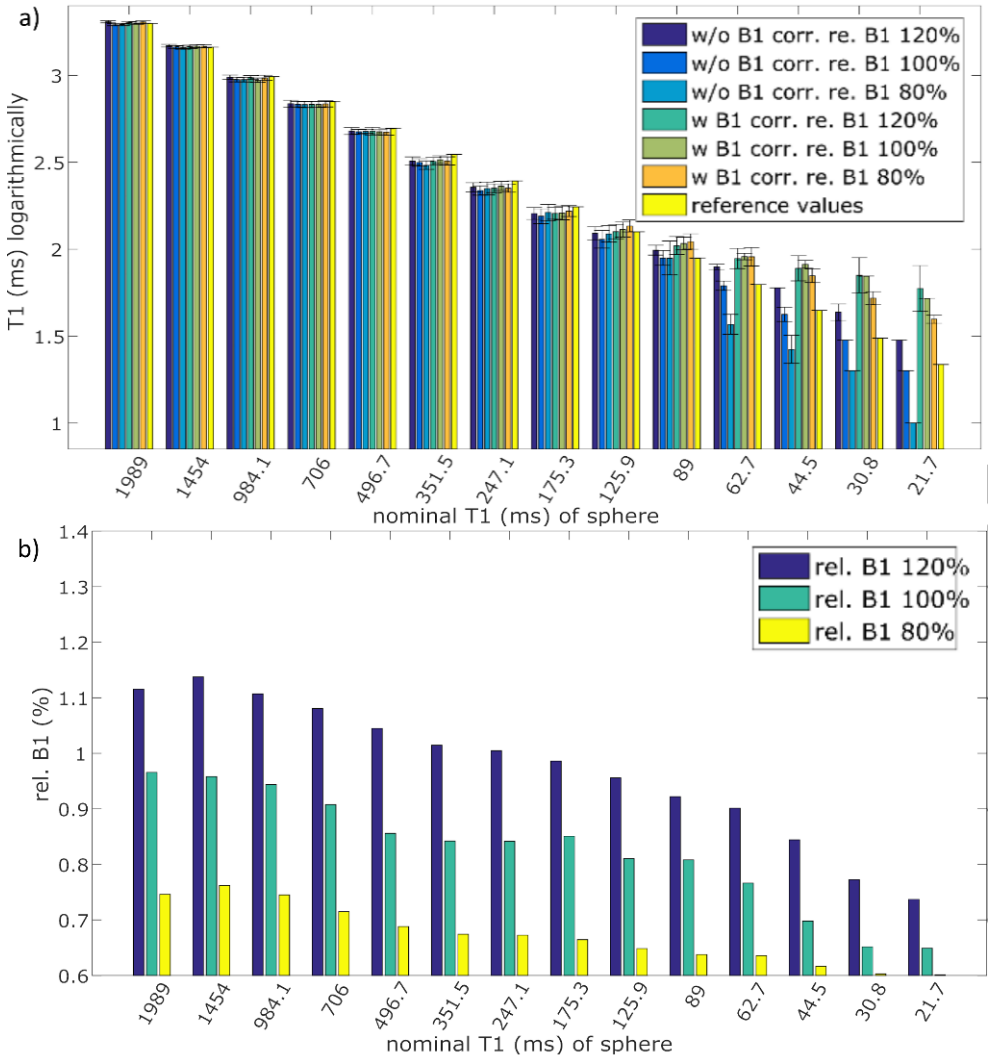

Figure 4.3: a) shows T_1 values measured with FISP-MRF with and without B_1^+-prescan correction and the nominal values in the 14 spheres of the T_1 layer in the NIST phantom. In b) the measured B_1^+ values in the spheres are shown for the three different transmit coil settings (80%, 100%, 120%).

and the difference between them. Similarly, T_2 maps and the differences are displayed on the right side. The differences between parameter maps with and without prescan based corrections exhibit a similar distribution as the B_1^+ maps.

4.1.1.3 Discussion

B_1^+ inhomogeneities have a severe impact on quantitative maps in MRF. Results show that especially T_2 values are exorable to RF transmit field inhomogeneities. Without correction, T_2

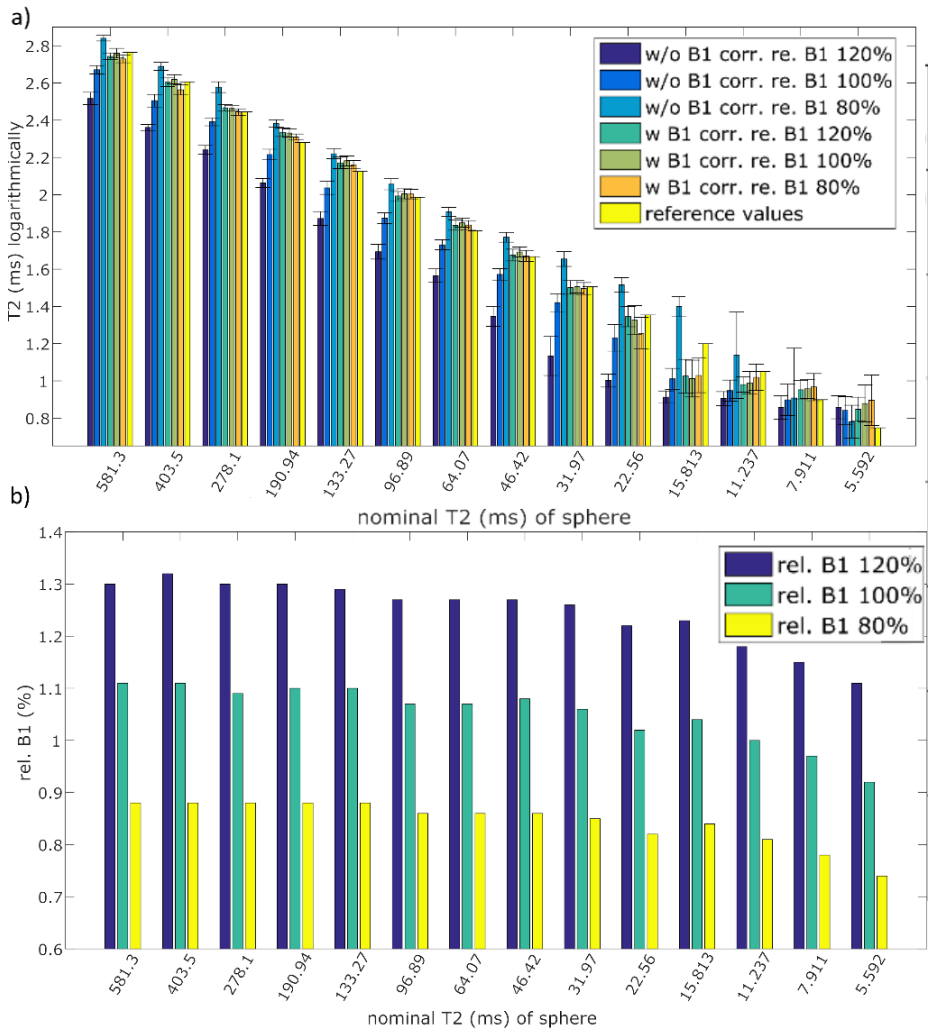

Figure 4.4: In a) T_2 values measured with FISP-MRF with and without B_1^+-prescan correction and the nominal values in the 14 spheres of the T_2 layer in the NIST phantom are depicted. The measured B_1^+ values in the spheres are shown in b) for three different transmit coil settings (80%, 100%, 120%).

values of the same tissue differ spatially up to 50%. There is also a dependency of T_1 values on B_1^+, but that is considerably smaller. T_2 values of white matter of the human brain differ from slice to slice and within each slice. Results show that a mitigation of the B_1^+ dependency can be achieved by acquiring a B_1^+ prescan and using the information in the template matching process. The accuracy and precision of this method rely on the employed B_1^+ mapping method. In this work the B_1^+ prescan is only accurate and precise for species with $T_1 > 400$ ms [Chu10] and leads to unsatisfactory results in species with smaller T_1. Since most clinically relevant tissues have higher T_1, the technique can be considered reliable.

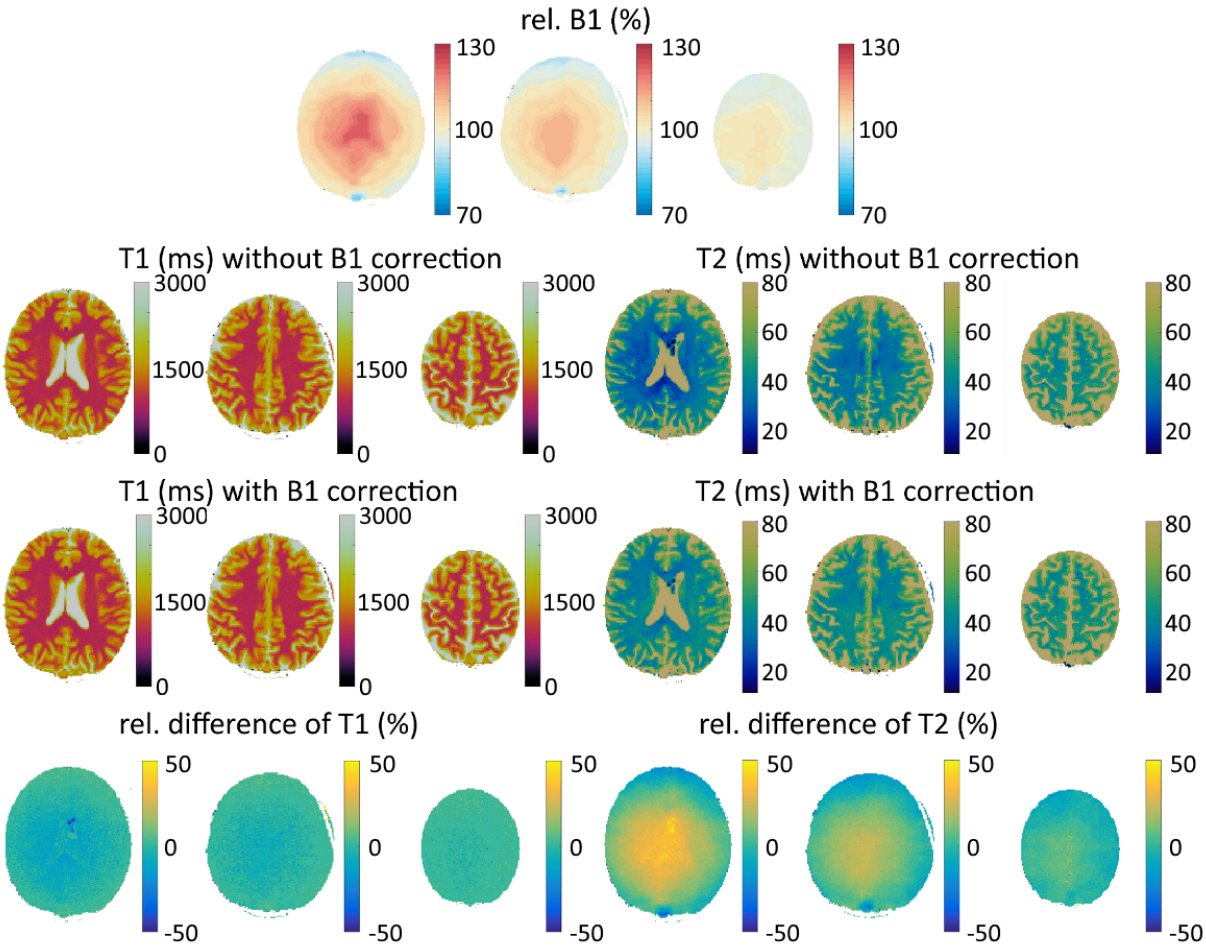

Figure 4.5: B_1^+ distribution measured in three axial slices of a human brain. The FISP-MRF T_1 maps and T_2 maps with and without B_1^+ correction as well as the relative difference between them is depicted.

4.1.2 Integration of B_1^+ into Magnetic Resonance Fingerprinting

Another approach to account for the inhomogeneity of the B_1^+ field is the encoding of B_1^+ in the fingerprints and subsequent identification of B_1^+ via pattern matching. Two different approaches are described in the following sections.

4.1.2.1 Dual Pulse Magnetic Resonance Fingerprinting

A novel encoding scheme for FISP-MRF was designed which introduces an additional dedicated B_1^+ dependent component into the complex signal evolution by applying two 90° phase shifted RF pulses in each TR. The content of this section has previously been published in abstract

form [Kör16].

4.1.2.1.1 Methods

The reference FISP-MRF sequence employs conventional slice-selective RF excitation pulses with identical phase. In the novel implementation (FoV 300mm, resolution 1.2 mm, slice thickness 5 mm), each conventional RF pulse is replaced by a composite variant comprising two pulses with a relative phase shift of 90 ° (compare Figure 4.6). Also, the flip angles of the encoding pattern were increased by 40% compared to the reference. For simplicity, in the current implementation both pulses are played out successively, rewinding the slice-selective gradient in between. This results in a phase evolution of the signal depending mainly on B_1^+, a property that has been used for the purpose of mapping the B_1^+ field before [Fei].

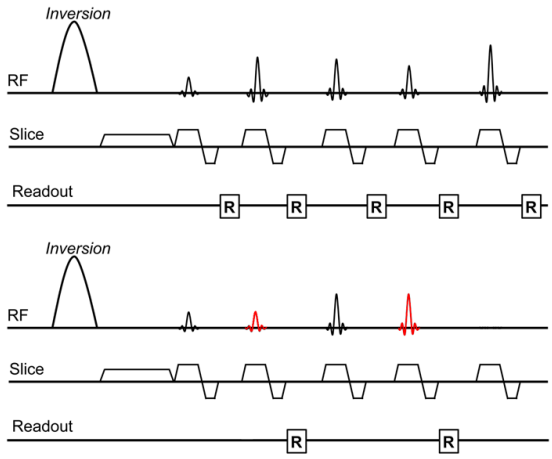

Figure 4.6: The original FISP-MRF sequence diagram is shown on top and on the bottom the proposed one with a second 90° shifted pulse of the same flip angle in each TR.

The resulting signal generated by this encoding can be adequately described and used for differentiation of MRF signals in the B_1^+ dimension. The resulting signal's phase is mainly governed by B_1^+. High-resolution 2D parameter maps were acquired on a human-head-shaped phantom filled with gel using a prototype MRF sequence implementing the novel encoding. For that purpose, a dictionary was calculated with a relative B_1^+ resolution of 5 %, ranging from 75 to 125%.

All scans were performed on a clinical 3T MR scanner (MAGNETOM Skyra, Siemens Healthcare, Erlangen, Germany).

4.1.2.1.2 Results

Figure 4.7 shows simulated phase evolutions of the tissue in the phantom (T_1: 300ms, T_2: 80 ms) for three different relative B_1^+ values. The phase differences are well visible in four segments of the signal evolution. These are the segments where relatively high flip angles ($> 80°$) are applied.

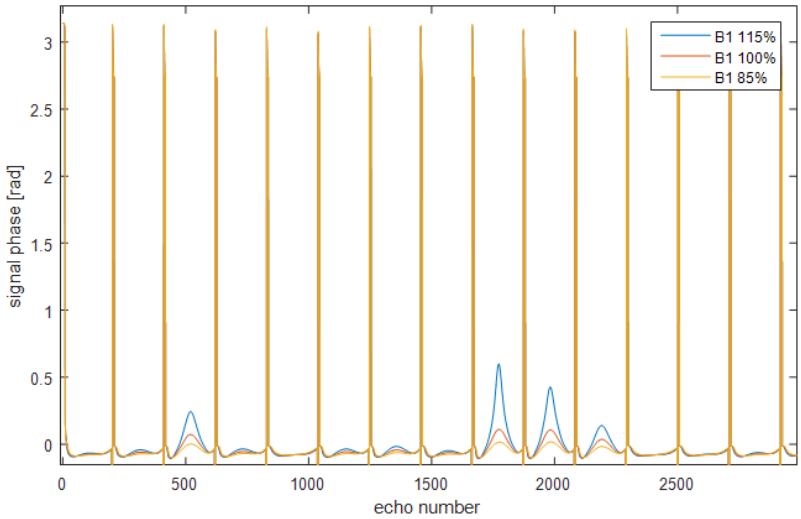

Figure 4.7: Simulated signal phases of a species with T_1 of 300ms and T_2 of 80 ms at three different relative B_1^+ settings (85%, 100%, 115%). The signal's phase mainly differs for different B_1^+ values at four segments in the time course. These are the segments where relatively high flip angles are applied ($> 80°$).

Figure 4.8 shows the template matching results in the homogeneous phantom. Since especially T_2 is very sensitive to B_1^+ inhomogeneities, a comparison of the T_2 map from the reference FISP-MRF method to the proposed method is depicted in the same figure. The underestimation of T_2 in the central region as well as the overestimation in the peripheral region is mitigated by the method using two RF pulses per TR and a reasonable B_1^+ map is generated.

4.1.2.1.3 Discussion

Results show that mitigation of B_1^+ effects on FISP-MRF can be achieved using dedicated composite RF pulses. This approach can be used in combination with sampling strategies that employ highly undersampled imaging techniques. Improvements can be made concerning more sophisticated, frequency-modulated single-pulse designs. Also, only a fraction of the RF pulse series could be extended by the novel encoding, or relative phase shifts could be varied throughout the encoding.

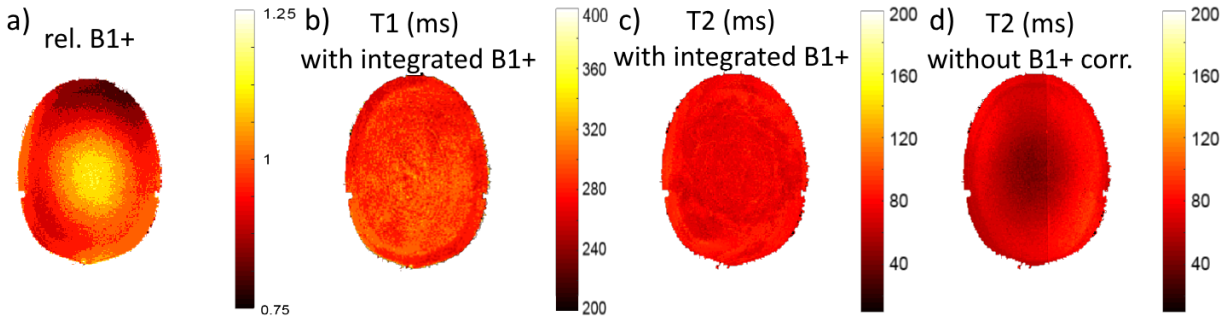

Figure 4.8: a) Relative B_1^+ map, b) T_1 and c) T_2 map as measured with the integrated B_1^+ FISP-MRF implementation using two RF pulses per TR. For comparison in d), the T_2 map from the original FISP-MRF (without using a B_1^+ correction) is shown on the right.

4.1.2.2 Combined FLASH and FISP Magnetic Resonance Fingerprinting

In this part of this thesis, the originally proposed FISP-MRF is extended to an alternative B_1^+ sensitive implementation. A novel encoding is applied, that generates continuous, transient signals that are sensitive to T_1, T_2 and B_1^+, which are all incorporated in the dictionary. The method was successfully applied and validated in phantoms, a human brain and the lower abdomen. The content of this section has previously partially been published in abstract form [Kör17].

4.1.2.2.1 Methods

The established encoding pattern [Jia15] was altered by replacing parts of the original encoding with three sections that employ RF spoiling with a phase increment of 117 ° [Zur91] . Each of these sections consisted of 420 time points. The maximum flip angles of each section are integer multiples of 6 degrees. Figure 4.9 shows the used flip angles and RF pulse phases. Images at each time point were acquired with single-shot spiral readouts. The spiral trajectory was designed to cover just a fraction of k-space and was rotated by an angle of 82.5 degrees from time point to time point as described in the previous chapter. A dual density spiral design [Mey11] was used to sample the two-dimensional k-space. For the phantom and brain study, a dual-density spiral trajectory was designed for a field of view of 300mm, a matrix size of 256 and an undersampling factor of 24 in the center of k-space with a transition to 48 in the peripheral regions of k-space. For the abdominal application, another spiral design with a FOV of 380 mm and a matrix size of 320 and an undersampling factor of 24 in the center of k-space with a transition to 48 in the peripheral regions of k-space was used. Another spiral design that was used for inspecting signal evolutions with less aliasing artifacts had a matrix size of 64 and a FoV of 300 mm with an undersampling factor of 4. Spiral trajectories for single-image reconstruction were corrected using a one-time calibration and a generalized eddy-current model by Tan and Meyer [Tan09].

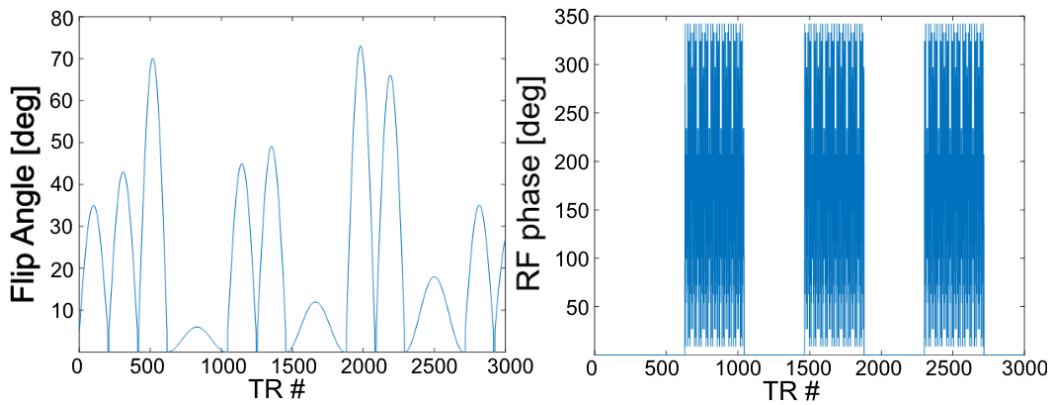

Figure 4.9: Flip angles (left side) and pulse phases (right side) used for the novel encoding scheme.

Sinc shaped RF pulses with a time-bandwidth product of 8, duration of 2000 ms and a slice thickness of 5 mm were used for all RF pulses except the adiabatic inversion pulse. For the abdominal scans, the flip angles in the FISP parts were scaled by a factor of 0.68 to account for RF power limitations.

Dictionaries were calculated using a Bloch simulation that included slice profiles and relaxation during the application of RF pulses. Relative B_1^+ values range from 0.7 to 1.3 in steps of 0.02. T_1 ranges from 100 ms to 3700 ms and T_2 from 4 ms to 1500 ms with variable step sizes. Two dictionaries were simulated, one for the novel encoding with RF spoiled segments and one using the originally proposed encoding in [Jia15].

Pattern matching was performed based on the multiscale iterative reconstruction [Pie16] with SVD compression [McG14]. A reconstruction with 5 iterations was employed, where the second to last pattern matching step was performed with only the RF spoiled signal parts to exploit the potentially lower flow sensitivity of voxels experiencing this effect. For this step T_1 and T_2 values were fixed to a range of $\pm 15\%$ of the result of the previous matching step while the relative B_1^+ was not constrained. In the last pattern matching step, the whole signal was matched with fixed relative B_1^+ from the previous matching step for each pixel. All data were acquired on a 3 T whole-body scanner (MAGNETOM Skyra, Siemens Healthcare, Germany).

Phantom validation

A phantom consisting of several cylindrical vials with different T_1 and T_2 relaxation times separated by air and a spherical phantom filled with doped water (Test Object T05, Sonar Diagnostics Ltd, Livingston/UK) were used for a quantitative evaluation. The vial phantom was scanned with the novel encoding scheme and for comparison with the originally proposed encoding for FISP-MRF. Since B_1^+ is very uniform throughout the vials, different B_1^+ settings

were created by manipulating the scanner's transmitter reference voltage. The phantom was scanned with relative transmitter gains of 0.8, 0.9, 1.0 and 1.1 1.2. The spherical phantom was scanned with the novel encoding scheme and the resulting B_1^+ map was compared to a reference scan as described in the following section.

Reference experiments

B_1^+ reference scans following the method described in [Ako93] were performed with the same FoV and matrix size as the MRF acquisitions. Flip angles of 90° and 120°, a TR of 1000 ms and a TE of 14 ms were employed. To obtain reliable quantitative T_1 and T_2 reference values for each phantom, two series of spin echo measurements, one with varying echo time (TE) and one with varying inversion time (TI) were performed. T_1 and T_2 values were obtained by fitting the measured data to the relaxation equations.

In vivo experiments

The novel MRF implementation was tested on a healthy volunteer's brain. Two axial slices, a sagittal and a coronal slice were scanned and the resulting B_1^+ map compared to reference B_1^+ maps. These experiments were performed using the spiral design with a matrix size of 256 and a FoV of 300 mm. Since highly undersampled MRF signals were highly artifact afflicted, another experiment in the brain was performed using the spiral design with a matrix size of 64 and FoV of 300 mm. This was performed to obtain signal evolutions exhibiting only mild undersampling artifacts that thus could be inspected visually. Experiments in the abdomen with the proposed method were performed using the spiral design covering a FoV of 380 mm and reduced flip angles in the encoding as described above.

Accelerated scans

Reconstructions of brain acquisitions were retrospectively accelerated by using only the first 1900 TRs which corresponds to a scan time of 28 seconds per slice. The results of these retrospectively accelerated MRF acquisitions were compared to the original results using all 3000 TR that correspond to a scan time of approximately 41 seconds per slice.

4.1.2.2.2 Results

Figure 4.10 shows results of the phantom consisting of several vials separated by air at different transmitter voltages.

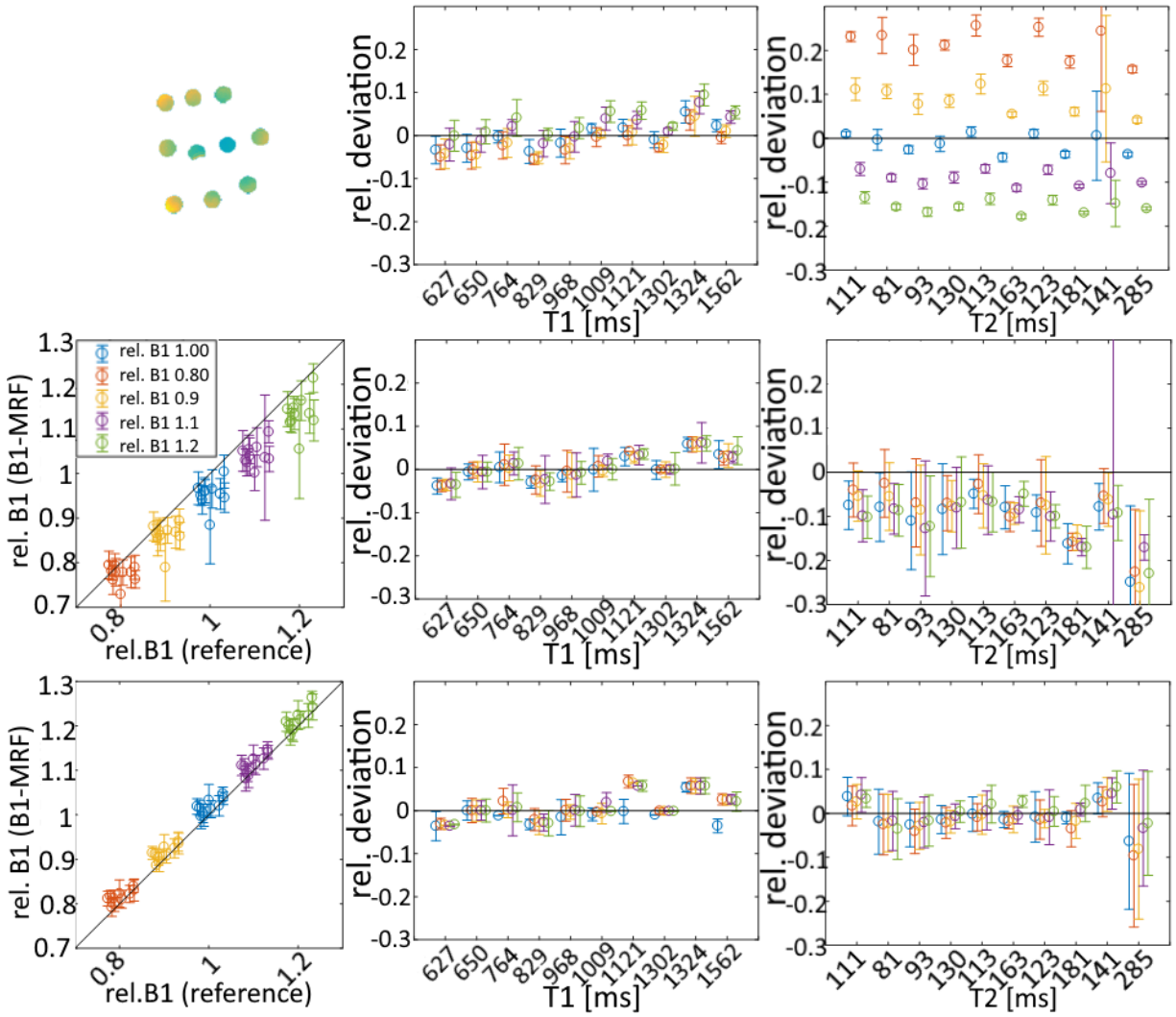

Figure 4.10: Phantom results for five different relative B_1^+ settings. Top row: Geometry of the phantom in an exemplary M0 map and matching results from using the original encoding without a B_1^+ dimension in the dictionary. T_1 and T_2 results (mean value and standard deviation) are displayed as relative deviation from values obtained with a spin echo measurement. Middle row: B_1^+, T_1 and T_2 results when using the original encoding with a B_1^+ dimension in the dictionary. Bottom row: Corresponding results for using the proposed B_1^+ sensitive encoding and a B_1^+ dimension in the dictionary.

The top row shows the geometry of the phantom in an exemplary proton density map and matching results from using the original encoding without a B_1^+ dimension in the dictionary. T_1 and T_2 results were displayed as relative deviation from values obtained with the reference spin echo measurement. They are given as mean value and standard deviation over the vial for five different relative B_1^+ settings. T_1 values were slightly increased with increased relative B_1^+. T_2 values show the opposed behavior and were decreased with increased relative B_1^+. The middle row shows B_1^+, T_1 and T_2 results when using the original encoding with a B_1^+ dimension in the dictionary. B_1^+ was underestimated and had high standard deviation, which in turn lead to underestimation of T_2 values and high standard deviation. The bottom row shows the corresponding results for using the proposed B_1^+ sensitive encoding and a B_1^+ dimension in the dictionary. B_1^+ as well as T_2 values were assessed correctly.

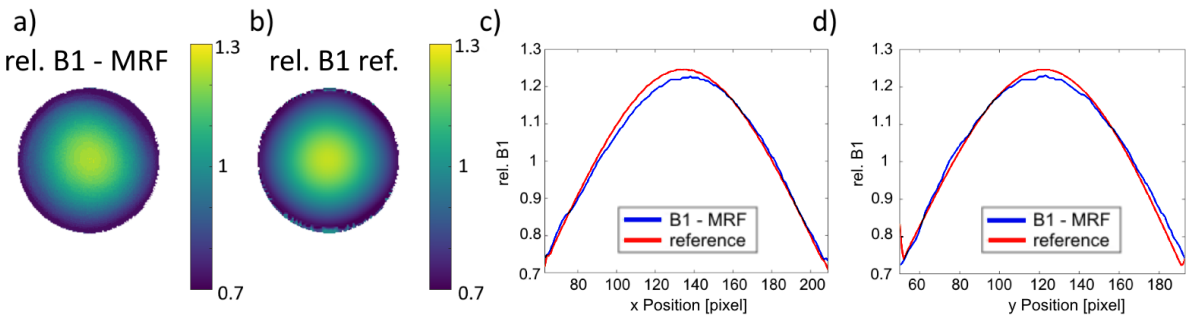

Figure 4.11: Comparison of a B_1^+ map in the spherical phantom. a) with the novel B_1^+ encoded MRF and a reference B_1^+ scan b). c) and d): B_1^+ profiles through the middle of the phantom in x and y direction.

Figure 4.11 shows a comparison of a B_1^+ map in the spherical phantom (a)) with the novel B_1^+ encoded MRF and a reference B_1^+ scan (b)). Additionally, the B_1^+ profiles through the middle of the phantom in x and y direction are plotted for both B_1^+ maps.

In Figure 4.12 an acquired signal evolution of a voxel containing CSF is shown. It is extracted from an in-vivo brain MRF acquisition using the spiral design with a matrix size of 64 and a FoV of 300 mm. The signals from acquisitions with lower undersampling factor were less afflicted by aliasing artifacts and could thus be utilized for visual inspection. The measured signal deviates strongly from the best matching fingerprint in the FISP segments. Deviations are especially high after the application of the inversion pulse, where the measured transversal magnetization does not reach zero. In contrary, the resulting match from using only the RF spoiled segments is close to the corresponding segments in the signal.

Figure 4.13 displays the results of an MRF acquisition in the human brain. a) shows the resulting T_1 map, b) the T_2 map and c) the rel. B_1^+ map when matching the full signal using the multiscale

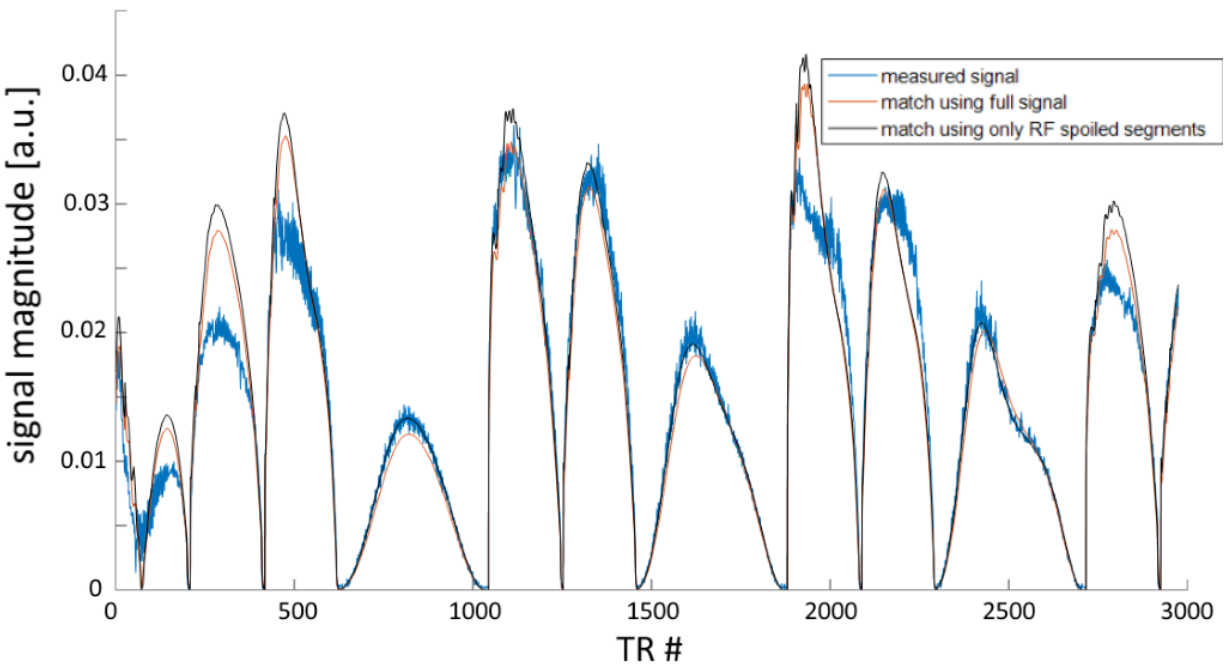

Figure 4.12: Signal evolution of a voxel containing CSF acquired with a spiral design with a matrix size of 64. The measured signal (blue) deviates strongly from the best matching fingerprint (red) in the FISP segments. The resulting match (black) from using only the RF spoiled segments is close to the corresponding segments in the signal.

reconstruction. Figure 4.13 d) displays the resulting B_1^+ map when matching only the RF spoiled segments in the second to last pattern matching step with T_1 and T_2 fixed to a limited range around the previous match result. Figure 4.13 e) shows the relative difference between these two results. Large deviations between c) and d) can be observed in voxels containing CSF. After matching only RF spoiled segments, the resulting B_1^+ map is smooth and no B_1^+ underestimations are present.

Figure 4.14 shows results of in-vivo brain MRF experiments. Two axial slices, one sagittal and one coronal slice are shown. In all three orientations MRF B_1^+ maps are in good agreement with the reference B_1^+ maps. T_1 and T_2 maps are free of B_1^+ effects.

Figure 4.15 depicts results in the lower abdomen. MRF B_1^+ maps are also in good agreement with the reference here and T_1 as well as T_2 maps are free of B_1^+ effects.

Results from a coronal brain scan using only 1900 TRs in the matching process are shown in Figure 4.16. For comparison, the relative B_1^+ map from the same acquisition using 3000 TRs for pattern matching. There is almost no change in B_1^+ maps when using less than two thirds of the signal.

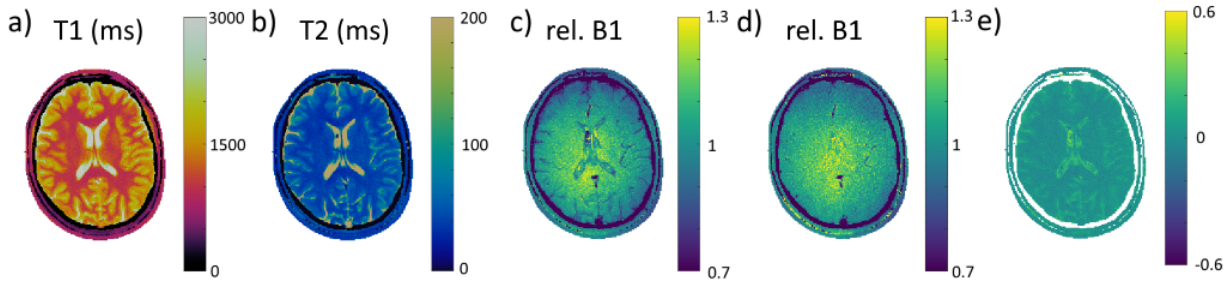

Figure 4.13: MRF parameter maps in the human brain. a) T_1 map, b) T_2 map and c) rel. B_1^+ map when matching the full signal using the multiscale reconstruction. d) displays the resulting B_1^+ map when matching only the RF spoiled segments in the second to last step with T_1 and T_2 fixed to a limited range around the previous match result. e) shows the the relative difference between these two results.

4.1.2.2.3 Discussion

A B_1^+ dimension can be added to FISP MRF for clinical purposes without the need to acquire a B_1^+ map separately. Unlike other methods, the proposed implementation is capable of estimating B_1^+ correctly in regions experiencing flow. Furthermore, it does not rely on segmented acquisitions or the use of multiple transmit channels [Clo16] and can estimate T_1, T_2 and B_1^+ simultaneously from a single continuous experiment.

The generated B_1^+ maps are in good agreement with reference B_1^+ maps. With this novel approach, quantitative maps in various orientations can be acquired in the human brain as well as in the abdomen. Wrong estimations of B_1^+ when using the full signal for pattern matching can be corrected by using only RF spoiled segments for a dedicated B_1^+ matching step. The resulting B_1^+ maps are smooth and bias free. This facilitates the application of further filtering of the B_1^+ map, exploiting the physical property that the transmit field is only slowly varying within the imaging volume, e.g. a guided median filter [He13].

It was observed that signals from RF spoiled segments are less prone to inflow of fresh magnetization. These signal segments do not rely as much on the spin history as the signal in FISP segments. Nevertheless, they are not completely immune to flow effects because of their dependency on longitudinal magnetization. Even though B_1^+ can be estimated with the proposed method, the precision of T_1 and T_2 values will be limited since the signal within the FISP segments is affected by flow. Instead of minimizing the dependency on flow, an alternative approach could incorporate flow into the signal model of an MRF experiment. The relatively lower flip angles in the RF spoiled compared to FISP segments also save magnetization for the following segments. This leads to higher SNR and possibly better overall differentiation capability of the whole signal. Another

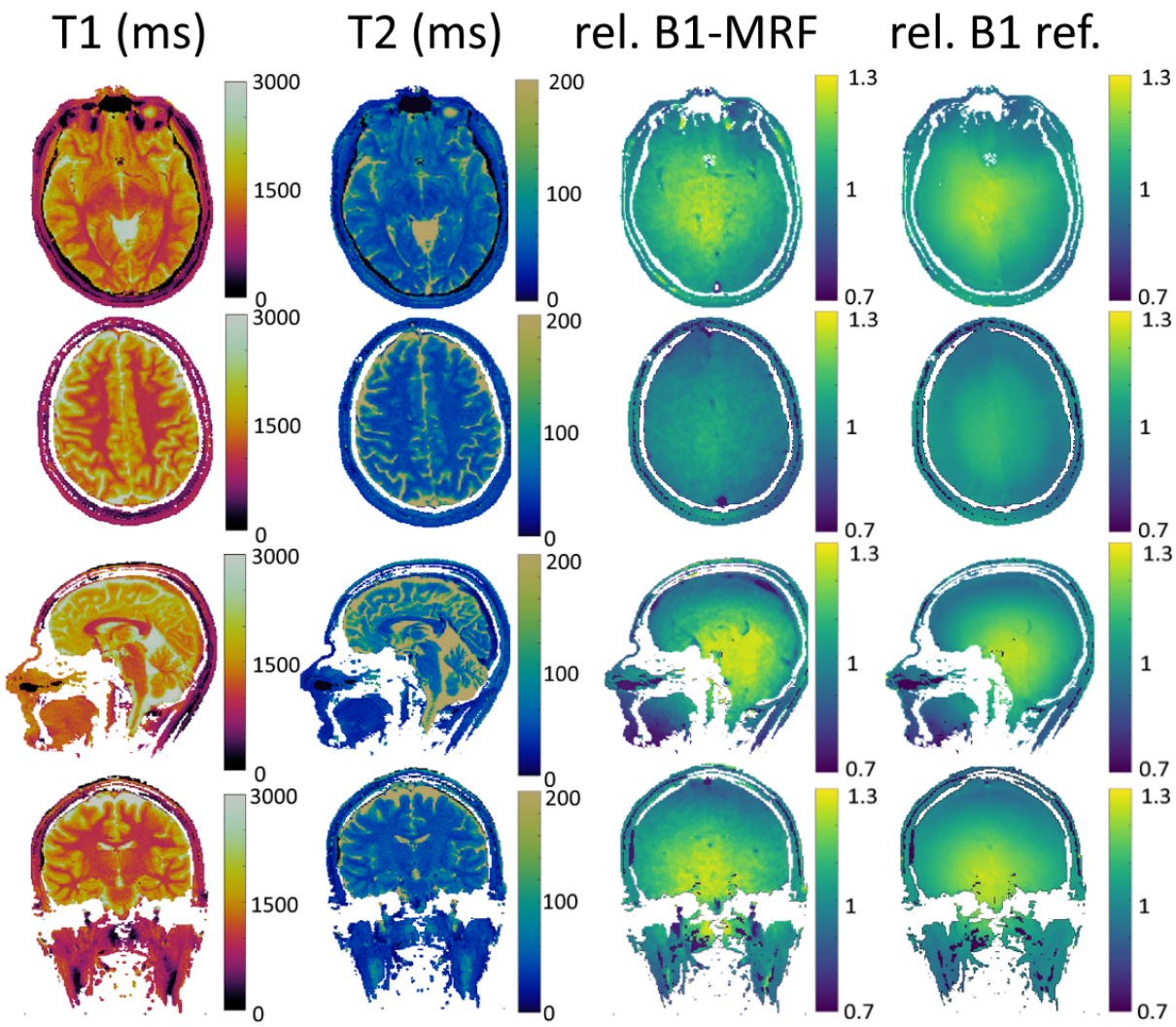

Figure 4.14: In-vivo B_1^+ sensitive MRF parameter maps in different orientations in the human brain. First column: T_1 maps, Second column: T_2 maps. Third column: rel. B_1^+ maps from MRF. Right column: reference B_1^+ maps for comparison.

benefit of RF spoiled signals is their smooth shape which is less affected by undersampling artifacts

Starting from a robust implementation using 3000 TR as a baseline, it was shown that the acquisition can be shortened to at least 1900 TR without sacrificing map quality. It was also found that only a rough B_1^+ estimation can be achieved when matching the original encoding scheme to a dictionary with an additional B_1^+ dimension. B_1^+ is underestimated and has higher variation in comparison to the proposed B_1^+ sensitive encoding in simple phantoms. In vivo, this approach did not work reliably.

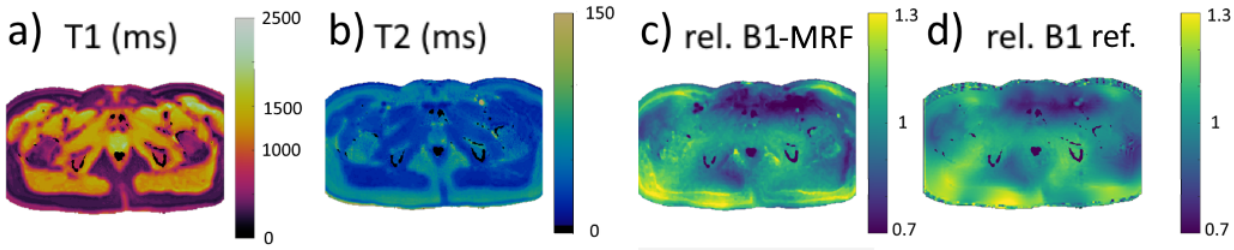

Figure 4.15: In-vivo B_1^+ sensitive MRF parameter maps in different orientations in the human abdomen. a) T_1 map, b) T_2 map, c) rel. B_1^+ map from MRF and d) corresponding rel. B_1^+ reference maps

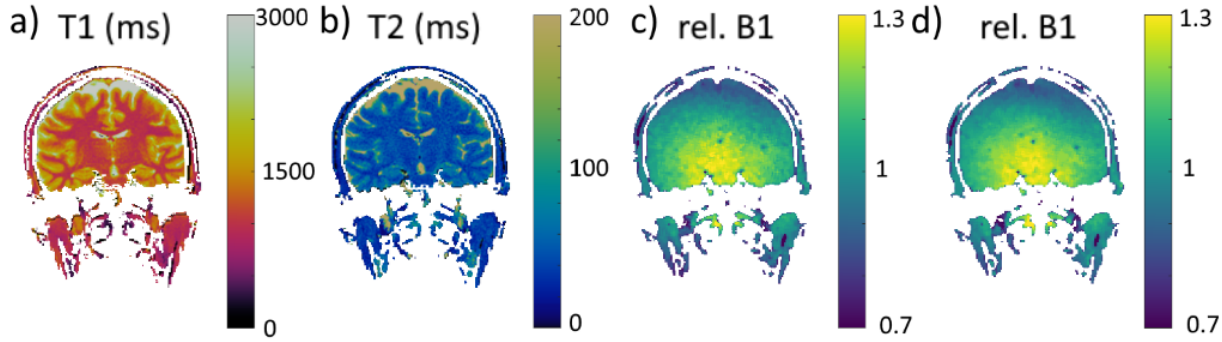

Figure 4.16: a) – c) Results from a coronal brain B_1^+ sensitive MRF experiment using only 2000 TRs. d) relative B_1^+ map from the same B_1^+ sensitive MRF experiment using 3000 TRs.

In contrast to methods acquiring a separate B_1^+ mapping measurement to correct for B_1^+ inhomogeneities, the method described here as well as other proposed methods [Clo16, Buo16, Buo17] might give more reliable results for a broader range of relaxation parameters. Since B_1^+ mapping methods depend on a certain degree on relaxation parameters (as e.g. [Chu10]) or are not accurate over a large range of flip angles, a dictionary matching approach including the relaxation parameters may turn out to be more comprehensive. At higher field strengths, B_1^+ inhomogeneities become more severe [Vau01] and even regions with B_1^+ voids may appear. In this regime, also adiabatic pulses might not be practical any more. A B_1^+ sensitive MRF method that utilizes multichannel transmit systems [Clo16] could be a promising approach under these conditions.

4.2 Influence of B_0 on Magnetic Resonance Fingerprinting

While the B_1^+ dependency in FISP-MRF is expected and can be addressed with several different approaches, B_0 has not been identified as a parameter that influences results. The gradient spoiling at the end of each TR is supposed to minimize B_0-dependent signal differences. In this chapter the sensitivity of FISP-MRF to B_0 is investigated.
The content of this section has previously been published in abstract form [Kör18a].

4.2.1 Methods

An implementation of the FISP-MRF method with a spiral acquisition scheme (undersampling factor 48, field-of-view 300 mm, resolution 1.2 mm, RF pulses with time-bandwidth-product of 8) was used. The spirals were rotated by 82.5 ° from TR to TR as described in a previous chapter. A B_1^+ correction based on a prescan as described in the previous section was employed.

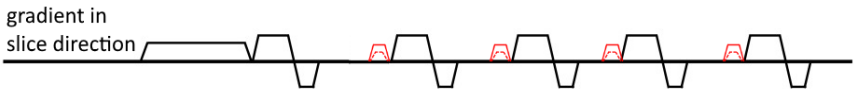

Figure 4.17: Schematic depiction of the additional dephasing moment in every TR. The dephasing moment was applied in slice selection direction, directly before the application of the regular slice selection gradient for the RF pulse. The gradient moment of the additional gradient was varied from experiment to experiment but kept constant within each experiment.

For the theoretical investigation a signal (T_1/T_2 (ms): 466/49) was simulated with and without an additional dephasing moment (corresponding to a dephasing of 8π across the slice thickness) in slice selective dimension before each RF pulse (Figure 4.17). The signals were simulated for [0, 20, 40, 60, 80] Hz off-resonance. The behavior of the spins across two times the slice thickness (since the pulses also excite spins outside the nominal slice thickness) was analyzed by plotting the spin distribution in the transverse plane. The behavior was related to a B_0 dependency.
Measurements on tubes filled with agarose and known T_1/T_2 combinations (T_1/T_2 (ms): 466/49, 643/77, 815/126, 954/111, 1009/163) were performed with 1D spatially encoded projection encodings. Instead of the spiral k-space trajectory, a Cartesian readout without phase encoding was used, such that a projection of the whole slice to a line in image space was acquired. This type of experiment lacks the spatial resolution of a 2D experiment. However, when performed in phantoms with limited extension in the projected dimension, it can be assumed that the phantom is homogeneous, including the B_1^+ and B_0 distribution. Under these conditions, this type of experiment provides undersampling artifact free projections and signal evolutions. Such

measurements were performed with different dephasing moments before each RF pulse and compared to the corresponding simulations. Mirroring the simulations, the vials were scanned with dephasing moments corresponding to $[1\pi, 2\pi, 3\pi, 3.5\pi, 4\pi, 8\pi]$ dephasing across the slice and with [0, 20, 40, 60, 80] Hz off-resonance.
Further conventional FISP-MRF measurements using spiral sampling and with varying artificial B_0 field gradients across the Field of View were performed on a head shaped homogeneous phantom without a dephasing gradient before each RF pulse. In vivo measurements with varying global B_0 field offsets were performed on a human brain, each without a dephasing gradient before each RF pulse and with a dephasing gradient corresponding to a dephasing moment of 8 π over the measured slice. Resulting parameter maps were evaluated in six ROIs inside white matter.

4.2.2 Results

Figure 4.18 shows measured (top row) and a simulated signal (bottom row) evolution for different off-resonances B_0 and excerpts at the position in the signal where relatively high flip angles ($>$ 70°) are applied. The effect of off-resonance is similar in both simulation and measurement. The signals are spread out for different off-resonances without additional dephaser (left side: 4.18 a), b) e, and f)). A B_0 dependency with a periodicity of $\frac{1}{TR} \approx 80Hz$ can be observed. The corresponding measured and simulated signals with an additional dephaser of moment 8π are displayed on the right side (Figure 4.18 c), d) g, and h)), where substantially less differences were observed.
The mean relative deviation of T_1/T_2 values averaged over the five different sample tubes, measured using the projection method and different dephasing gradient moments at different off-resonances are plotted in Figure 4.19. A trend to lower deviations with higher additional dephasing moments can be seen.
Figure 4.20 shows the transverse components of simulated spin ensembles across two times the slice thickness with arbitrary T_1 and T_2, without (a) and b)) and with (c) and d)) employing an additional dephasing moment. Two time points are shown; after the first RF pulse (a) and c)) and after ≈ 500 RF pulses (b) and d)). The behavior of the spin ensembles is considerably different. The mean signal of the spin ensemble is not 0 in the case without additional dephaser before the application of an RF pulse, i.e. the spin ensemble is not fully dephased.

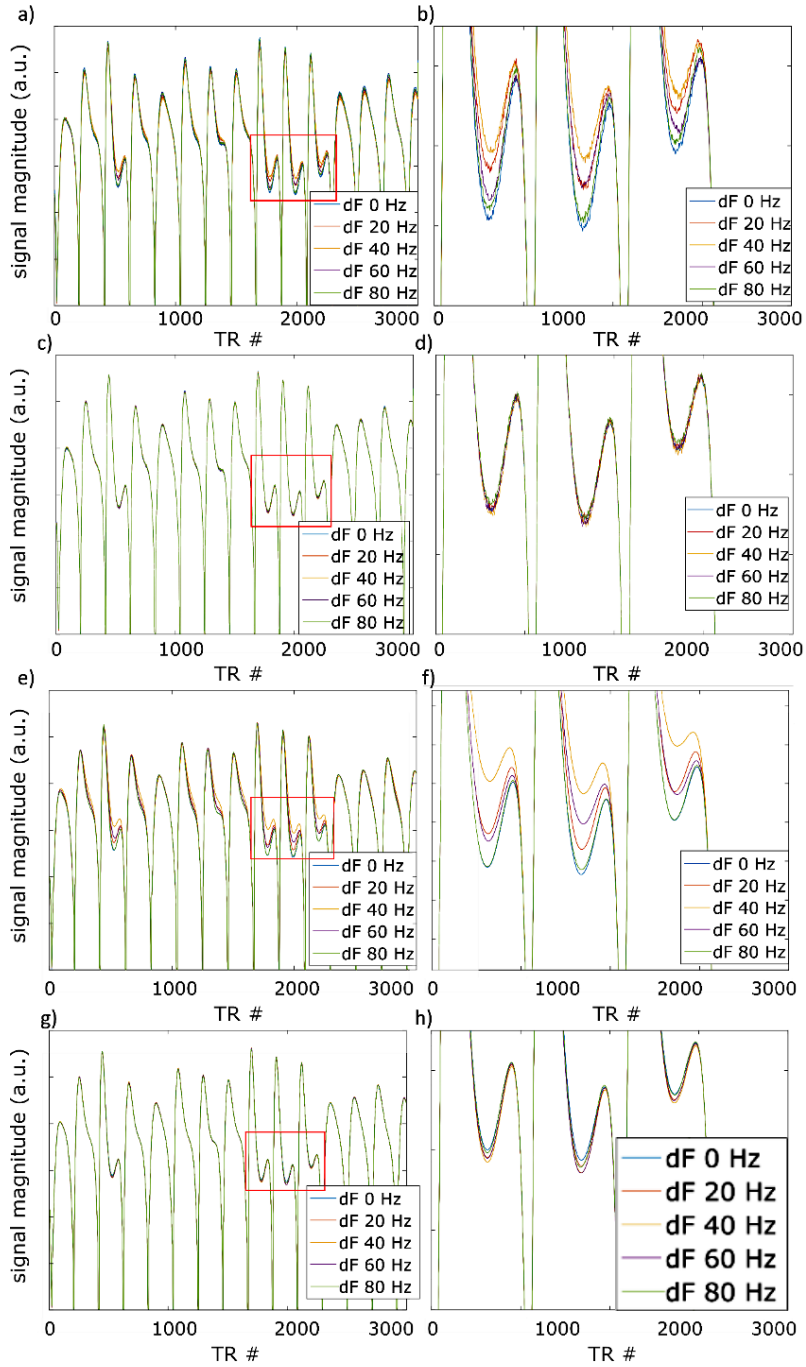

Figure 4.18: In a) measured signals using the projection method of a specimen with T_1 of 466 ms and T_2 of 49 ms at [0, 20, 40, 60, 80] Hz off-resonance are shown. An excerpt of the signal evolution (red box) where relatively high flip angles are applied is shown in b). In this measurement, no additional dephaser was applied. The measured signals from the same specimen but using an additional dephaser that causes an 8π dephasing over the slice is shown in c) (d) shows the excerpt of the measured signal). e), f), g) and h) show the corresponding simulated signals. In e) and f) the simulated signals without the dephaser are shown and in g) and h) with the dephaser.

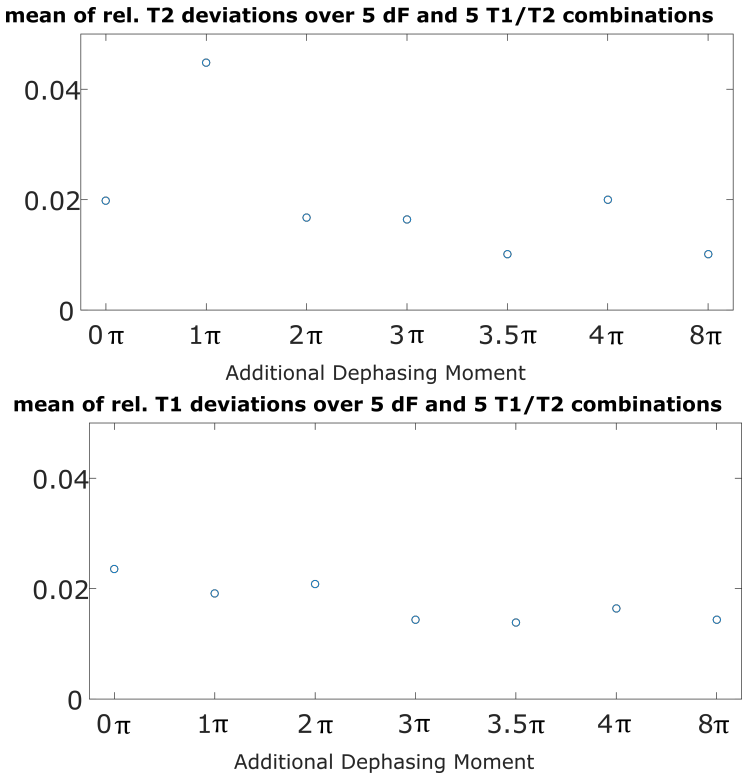

Figure 4.19: Average relative deviations of matching results using the projection method to the nominal value over five off-resonances (dF) [0, 20, 40, 60, 80] Hz in the five examined tubes. The relative T_2 and T_1 deviations when using different additional dephasing moments averaged over the five specimen are depicted.

T_1 and T_2 maps in the head shaped phantom illustrate the B_0 dependency in the 2D MRF experiment. Resulting maps are displayed in Figure 4.21. Depending on the local B_0 field, T_1 and T_2 values are altered. Since an artificially introduced linear B_0 gradient was applied, the periodicity of the B_0 dependency translates to a sinusoidal dependency of T_1 and T_2. With higher B_0 gradient the periods become smaller.

Figure 4.22 displays one of the T_1 and T_2 map in the human brain from MRF experiments without an additional dephaser and with an additional dephasing moment of 8π with global B_0 offsets. For simplicity only the parameter maps of the experiment with the additional dephaser and without applying a global B_0 offset is shown in this Figure. T_1 and T_2 values in six ROIs placed in white matter regions are further evaluated and depicted in Figure 4.23. Considerably higher deviations can be observed without an additional dephasing moment.

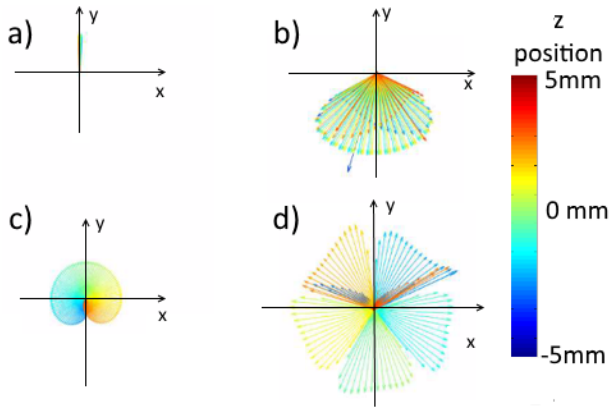

Figure 4.20: Transverse components of simulated spins over two times the full slice thickness (5mm). a) shows the transversal components of the spins after the first RF pulse in FISP-MRF without additional dephaser and c) after approximately 500 RF pulses. b) and d) show the corresponding transverse components of the spins at the same time points when using a dephaser. In the latter case, the spins are distributed more evenly in the transverse plane.

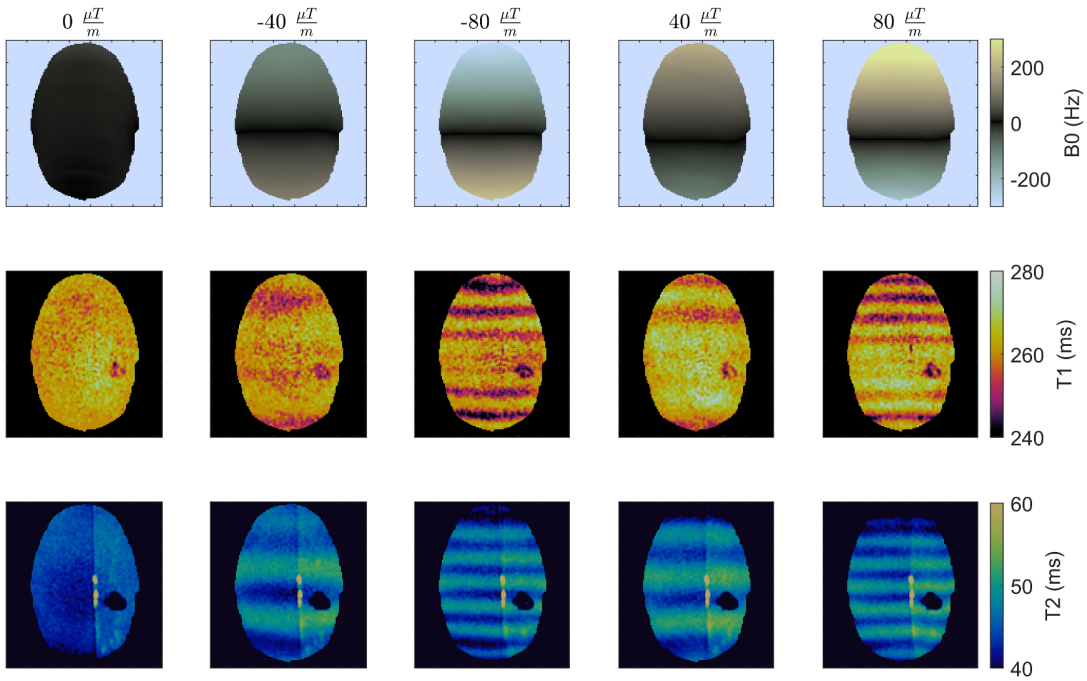

Figure 4.21: B_0 distributions achieved by varying shim currents and the matching results from FISP-MRF without additional dephaser in the human head shaped gel phantom. The periodic B_0 dependency can be observed in the parameter maps.

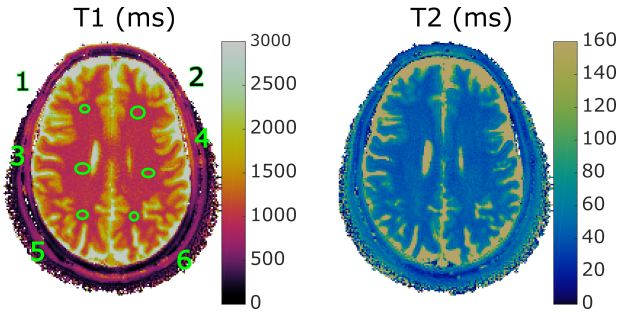

Figure 4.22: T_1 and T_2 map generated with FISP-MRF in one slice of a human head and the position of six ROIs where values were further analyzed.

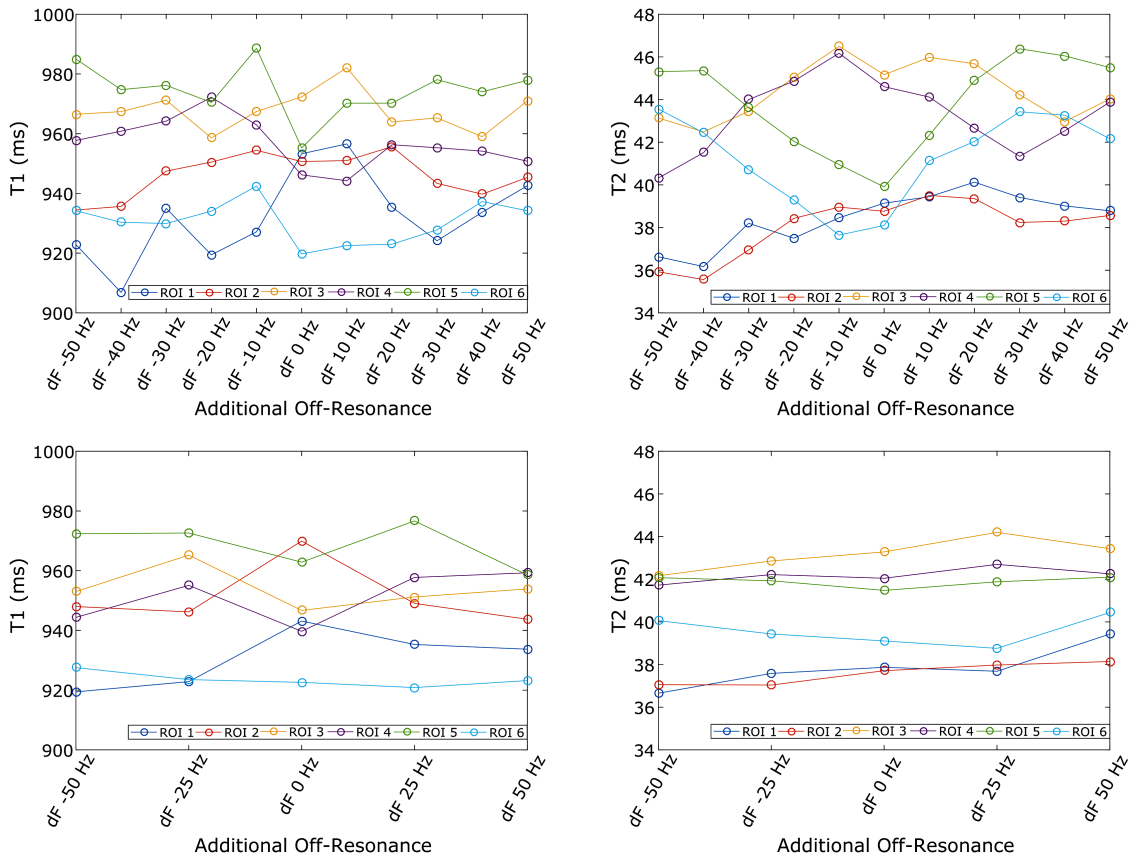

Figure 4.23: Parameter values in the six ROIs as shown in Figure 4.22 without using the additional dephaser (top row) and with using a dephaser causing a 8π dephasing over the slice. The variation of T_1 and T_2 values can be largely mitigated when employing the additional dephaser.

4.2.3 Discussion

A B_0 dependency in slice-selective FISP-MRF can be observed when the spin ensemble is not sufficiently spoiled before the onset of the RF pulse if no additional dephasing gradient is used.

This leads to a mild TrueFISP-like B_0 dependency that could be shown in a series of basic and in vivo experiments and was replicated in simulations. Since a TR of approximately 13 ms was used in the MRF implementation, the signal with an off-resonance of $40Hz \approx \frac{1}{2}TR$ differs most from the one with 0 Hz, while the signals from 0 and $80Hz \approx \frac{1}{TR}$ are almost the same.
To mitigate this TrueFISP-like off-resonance dependency, a sufficient spin dephasing before the onset of the RF pulse has to be ensured. An unbalanced slice-selection gradient is not sufficient since B_1^+ is already applied at the beginning of the slice-selection gradient while spins are not yet dephased. The assumption that a substantial amount of B_1^+ is applied at the middle of the pulse and sufficient spoiling of the spins by the slice selection gradient has already occurred at that time point does not hold. However, if all B_1^+ would be instantaneously applied at the middle of the slice-selection gradient, no additional dephasing moment would be needed, since the slice selection gradient would already have dephased the spins enough.
With different dephasing moments, the B_0 dependency can therefore be mitigated. A dephasing moment of 3.5 π has a similar effect as a dephasing moment of 8 π in this study.

4.3 Magnetic Resonance Field Fingerprinting

In this chapter, a method termed Magnetic Resonance Field Fingerprinting (MRFF) was developed, that generates T_1, T_2, B_0 and B_1^+ maps from a single continuous measurement using the MRF framework. Rather than employing prescans for characterizing the magnetic field inhomogeneities or trying to desensitize the sequence to such inhomogeneitites, an encoding pattern was designed, which yields distinguishable signals in all parameter dimensions. This approach promises stable identification of tissue related parameter maps by simultaneously matching acquired signals to a dictionary with all parameter dimensions to avoid subsequent errors. Further on, the knowledge of additional parameters can be utilized in further ways. Off-resonance maps can e.g. be used to further enhance the results by spiral deblurring, which has been applied to MRF [Ost17]. The content of this chapter has previously been published as a journal article [Kör18c]. Verbatim copies of text passages are marked with quotation marks.

4.3.1 Methods

Acquisition

"In the prototype implementation of MRFF, a sequence is designed that exploits several degrees of freedom. Flip angles, pulse phases, gradient moments and TE are varied, to design a sequence that integrates FLASH-, FISP- and TrueFISP-segments into one continuous acquisition. After the application of an adiabatic inversion pulse, a series of 3000 images is acquired. The sequence configuration is depicted in Figure 4.24. The first sequence part is a FISP segment, which is followed by a TrueFISP segment without phase cycling and then a TrueFISP segment with $0-180°$ phase cycling. After this, the first FLASH segment is placed. The order FISP - TrueFISP - FLASH is maintained for the rest of the sequence. In contrast to most previous MRF implementations, TR is kept constant at 12 ms yielding benefits that are described later. The acquisition time per slice is 36 seconds.

Sensitivities of each sequence with respect to tissue parameters and magnetic field parameters are different. In MRFF, this is exploited to generate signals with high sensitivity to each parameter. FISP is mainly sensitive to T_1, T_2 and B_1^+, FLASH to T_1 and B_1^+, and TrueFISP to T_1, T_2, B_0 and B_1^+. While FISP and TrueFISP are already sensitive to B_1^+, the FLASH segments help to resolve ambiguities [Clo16]. A FISP or TrueFISP signal with higher B_1^+ can e.g. resemble very closely one with a lower T_2. This kind of ambiguity can be better resolved with the FLASH segments that have only very little sensitivity to T_2. The FLASH parts of the encoding are characterized by low flip angles and quadratic phase increment [Zur91] from one RF pulse to the next. Since RF

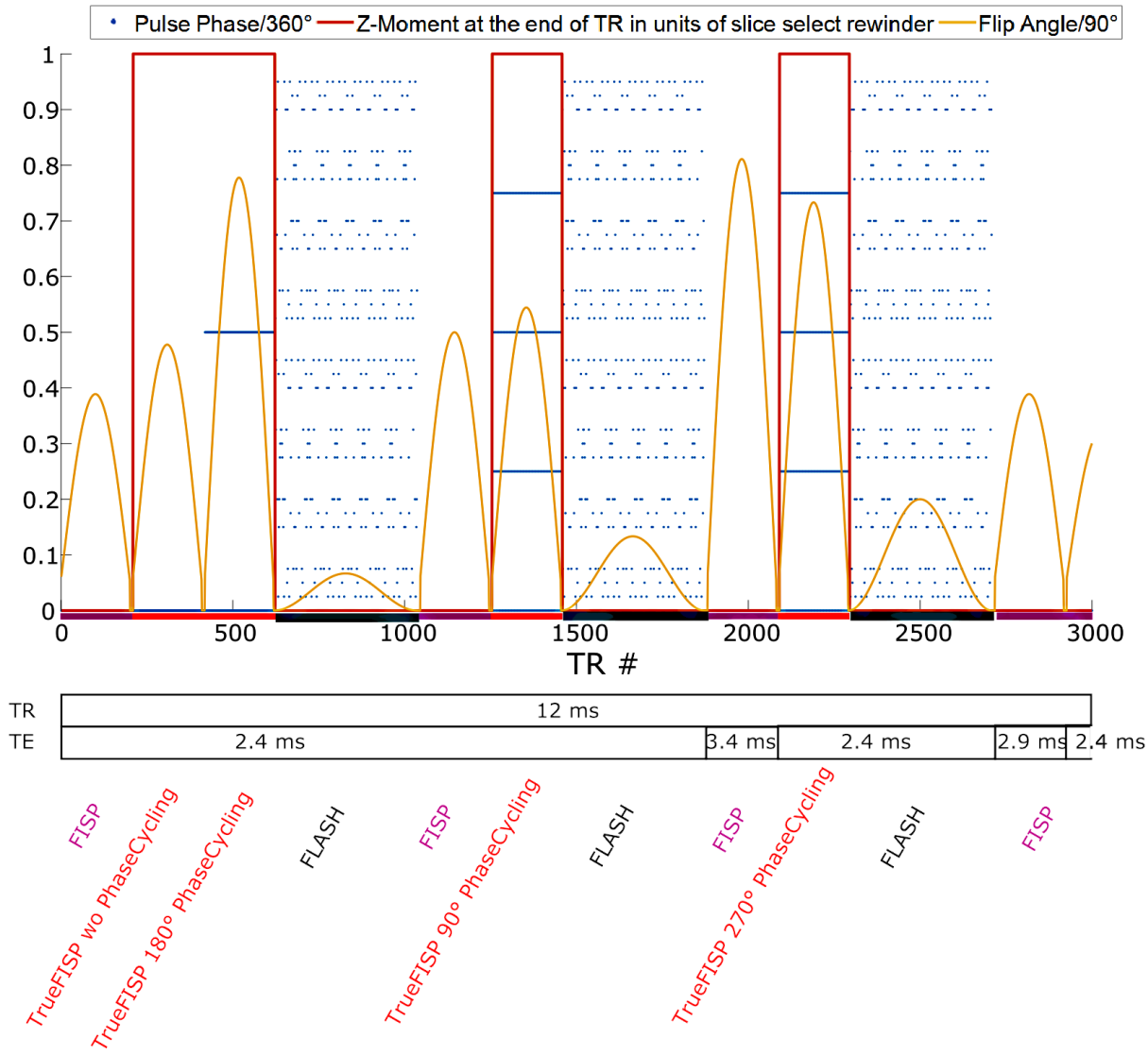

Figure 4.24: Flip angles, pulse phases, echo times (TE), repetition times (TR) and gradient moments in z direction used for the MRFF encoding. Each segment is also described by its sequence type. Employing an additional gradient moment in z direction that has the same moment as the slice select rewinder in one TR leads to fully balanced gradient moments in this TR. Leaving out the additional gradient moment results in a dephasing moment equivalent to the moment of the slice select rewinder. Image taken from [Kör18c].

spoiling destroys higher-order coherences, the T_2 sensitivity of the signal is negligible.

One possibility to shift the stopbands in the TrueFISP segments would be to alter the TR during the acquisition. While this is possible in theory, a large difference between the minimum and maximum TR would have to be used to shift the stopbands far enough. This would lead to a non-efficient k-space sampling because not all TR duration can be used to sample data in case

a sampling pattern of constant temporal duration is used. A more efficient approach would be to use varying k-space sampling patterns, i.e. very long and very short spirals. This approach is more appealing but also a lot more challenging. In MRFF a different strategy is employed: each of the TrueFISP segments uses a different phase cycling ($0°, 180°, 90°$ and $270°$ increments). This ensures that the entire frequency spectrum has high signal in most of the TrueFISP segments as well as differentiable signals with respect to B_0. Since the phase cycling pattern in MRFF is constant within each TrueFISP segment, a stop band condition also leads to rapidly decaying signal in MRFF. These low signals are compensated for by FISP and FLASH as well as the other TrueFISP segments, where this condition is not fulfilled.

With adding a dimension to the dictionary, the number of fingerprints that must be simulated rises exponentially. For decreasing the size, the TR is kept constant in MRFF to limit the extent in B_0 dimension. Because of employing a constant TR, the B_0 dimension in the dictionary only needs to cover one period of the banding structure. Therefore, the range of the B_0 dimension can be limited to (+/- 2/TR) Hz. The downside of limiting the B_0 dimension is wraparounds appearing in the B_0 maps. This wrap is not relevant for accurate matching of the parameters, but unwrapping the B_0 map may be useful for further processing steps, such as spiral deblurring. This can be achieved by FISP segments with different echo times. The resulting phase differences serve for computing a coarse B_0 map for unwrapping.

Images for each TR were encoded by spiral readouts. The spiral trajectory was rotated by an angle of 82.5 or 84 degrees from time point to time point as described in chapter three, resulting in a series of strongly undersampled images. Dual-density [Mey11] spiral trajectory designs were used in this work, with spatial resolutions varying from 1.2 to 0.8 mm in-plane, undersampling factors from 48 to 90, and readout durations from 4.98 to 6.28 ms. For undersampling factors of 48, a rotation angle of 82.5 degrees was used as described in a previous chapter, and for undersampling factors higher than 48, a rotation angle of 84 degrees. For brain scans, 'sinc'-shaped Hanning-filtered pulses with time-bandwidth product (TBP) of 8 and duration of 2000 μs and a slice thickness of 5 mm were used for RF excitation. For abdominal scans, 'sinc'-shaped Hanning-filtered pulses with a time-bandwidth product (TBP) of 4 and duration of 2000 μs were used to account for RF power limitations. For the case of TBP 8, the slice-select rewinder gradient moment is 8 π, and for TBP 4, it is 4 π. In FISP and FLASH segments, the dephasing moment is solely generated by the slice-selective gradients and no additional dephasers are used.

Dictionary Calculation

An MRFF dictionary was simulated with B_0 ranging from -41.33 to 41.33 Hz in 1 Hz steps, relative B_1^+ from 0.7 to 1.3 in 0.03 steps, T_1 from 50 ms to 5000 ms, and T_2 from 5 ms to 2000

ms, the latter two in logarithmic steps of 9.5%. Each dictionary entry was calculated using a C++ based Bloch Equation simulation of 200 spins that takes the slice profile into account [Ma17a]. The dictionary was compressed using SVD [McG14] to 50 singular values.

Image Reconstruction

Acquired data was reconstructed using a nonuniform fast Fourier transform [Fes03] with corrected spiral trajectories, using the generalized eddy-current model by Tan and Meyer [Tan09]. The actual parameter matching to the dictionary is divided into five steps in order to improve the robustness of results with respect to intravoxel dephasing and flow artifacts as described in the previous chapter. The reconstruction process is schematically summarized in Figure 4.25.

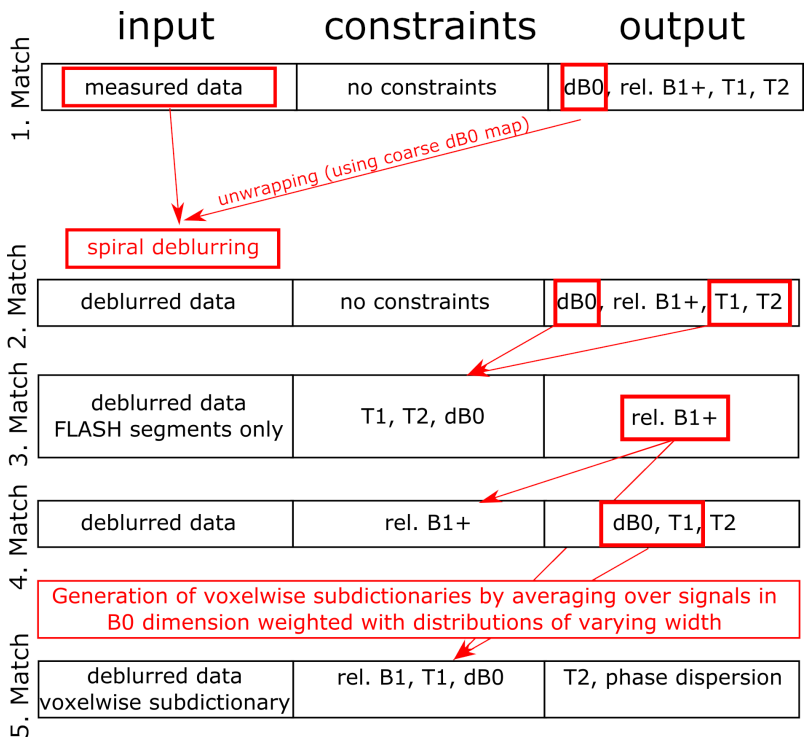

Figure 4.25: Schematic description of the reconstruction process. For each matching step, the input data, the constraints (partially or totally fixed parameters in the matching step) and the output are shown. Non-pattern matching steps are shown in red. Image taken from [Kör18c].

A first pattern matching with the whole dictionary is carried out for all voxels' signals, yielding T_1, T_2, B_0, and B_1^+ maps. The B_0 map potentially has wraparound artifacts and is unwrapped with the information of the coarse B_0 map. For this unwrapping step, the coarse B_0 map is calculated from the phase difference of the signals from the FISP parts with different echo times and smoothed afterwards. Then, the difference between the B_0 map resulting from the first match and the coarse

B_0 map is computed. According to the difference, multiples of 1/TR can be added to the wrapped B_0 map to preserve the high-resolution B_0 information while covering a broader range of B_0 than the one that exists in the dictionary. An example of the wrapped B_0 map, the difference map and the final B_0 map is shown in the Figure 4.26. In this example, a linear field shim in the vertical dimension was applied to illustrate the process. In the difference map, 5 segments corresponding to multiples of 1/TR can be seen. A spiral deblurring step is implemented after the calculation of the full scale B_0 map. The SVD-compressed images are deblurred in this step by using a frequency-segmented method [Nol92]. A second matching step follows that uses the deblurred SVD compressed images as input, yielding T_1, T_2, B_0 and B_1^+ maps.

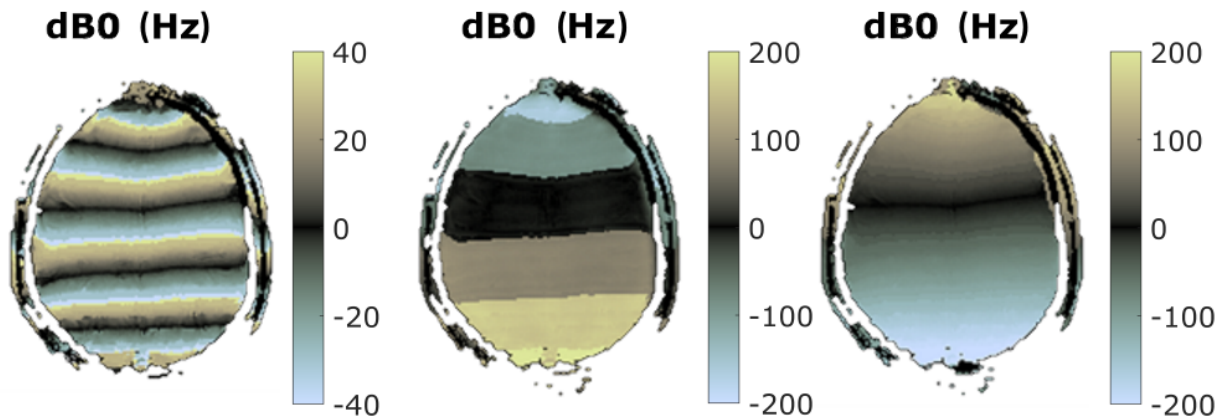

Figure 4.26: Illustration of the B_0 unwrapping process. The wrapped B_0 map resulting from the first pattern match is shown on the left side. The difference of the coarse B_0 map resulting from the phase difference of the FISP segments with different echo times and the wrapped B_0 map is shown in the middle. By rounding this difference to multiples of 1/TR and subtracting the result from the wrapped B_0 map, the unwrapped B_0 map on the right can be generated. Image taken from [Kör18c].

The B_1^+ matching result can be erroneous due to flow artifacts which are caused by inflowing fresh spins that have a different spin history than the expected one for stationary spins. While this effect also affects T_1 and T_2 estimation its influence on B_1^+ results can be mitigated by a dedicated matching step (as described in a previous chapter), that exploits the small T_2 and transverse magnetization history dependency of the FLASH signal. This third matching step is implemented by only matching FLASH segments while fixing B_0 and keeping T_1 and T_2 fixed to a certain range around the results from the previous matching step. It produces a B_1^+ map that is less afflicted by flow artifacts and can be smoothed using an image-guided filter [He13]. A fourth matching step follows, where the B_1^+ from the previous matching step is fixed while all other parameters remain unconstrained. In the fifth and last step, the T_2 results are refined by adding a matching

that takes intravoxel phase dispersion into account. Each voxel's signal is matched against its own additionally synthesized subdictionary. These subdictionaries have a T_2 and phase dispersion dimension, while T_1, B_0, and B_1^+ are fixed. Their fingerprints are generated by adding up signals in the B_0 dimension and thus approximate fingerprints arising from spins precessing at different frequencies in one voxel. For each T_2, the phase dispersion dimension is spanned by adding up the fingerprints along the B_0 dimension. The factors for summing up the signals are obtained from Gaussian distributions with varying standard deviation that are centered at the B_0 match of the respective voxel. With this step, the T_2 results are refined, and additionally a measure for the phase dispersion inside the voxel can be determined.

Phantom Study

A phantom consisting of several agarose filled vials with different T_1 and T_2 relaxation times separated by air was used for a quantitative evaluation. To manually create B_1^+ variation, the scanners transmitter voltage was modified. In addition, the phantom was scanned with various global B_0 offsets, spatial resolutions, TBP of the RF excitation pulses, and slice thicknesses. In total, 18 scans were carried out on three different days and with slightly different arrangements of the vials.

Furthermore, a single vial was scanned using a 1D projection to remove the influence of undersampling artifacts. Projection direction and readout were set perpendicular to the vial axis with 12 voxels being inside the vial. A readout phase dispersion of 20 Hz per voxel was set up to qualitatively depict the effect of intravoxel phase dispersion on the measured signal. The sensitivity of the phase dispersion measure was also evaluated on simulated data. To do so, the similarity of fingerprints synthesized assuming different phase dispersions and the corresponding single-frequency fingerprint was calculated for different mean B_0. T_1 of the fingerprints was set to 941 ms and T_2 was set to 71 ms. The simulation was done for a relative B_1^+ of 1.00 and for all B_0 in the dictionary with a dispersion corresponding to a Gaussian distribution with FWHM of 6Hz and 30Hz, respectively.

Reference Experiments

To obtain reliable quantitative numbers to compare MRFF results with, two series of spin echo measurements were performed in the quantitative phantom. One series with varying echo time (TE: [12, 28, 44, 60 ,68, 84, 100] ms) and the other series with varying inversion time (TI: [50, 100, 150, 200, 300, 400,600,1000] ms) and constant echo time of 12 ms The repetition time was 6 seconds, the FoV 230mm, the matrix size 256 for both measurements and a readout bandwidth

of 130 Hz/px was used. T_1 and T_2 values were obtained by fitting the measured data to the relaxation equations. B_0 reference scans (FoV of 230 mm, matrix size 64) were performed using established B_0 mapping techniques that use different echo times (4.92 ms and 7.38 ms) and calculate B_0 from the phase difference. B_1^+ reference maps were acquired using the sequence provided by the scanner software called $''rfmap''$ [Ako93] with a FoV of 300mm and a matrix size of 128. Flip angles of 90 and 120 degrees, a TR of 1000 ms and a TE of 14 ms were employed.

In Vivo Experiments

The novel MRFF implementation was tested on healthy volunteers' brains after informed consent. T_1 and T_2 maps from an MRFF acquisition (in-plane resolution 0.9 mm, undersampling factor of 48, slice thickness 5 mm, TBP 8) were compared to the ones obtained from a FISP-MRF implementation with a prescan-based [Chu10] B_1^+ correction. The acquisition time of FISP-MRF was 41s per slice and 21s for the B_1^+ map covering the whole volume. Respective B_0 and B_1^+ maps were compared to corresponding ones from conventional sequences. Furthermore, six ROIs were positioned in the maps, and T_1, T_2, B_0 and B_1^+ values inside the ROIs were compared. The integrated spiral deblurring in MRFF was tested by manually adding a B_0 shim to achieve a 400 Hz anterior-posterior gradient across the brain. The maps were compared to the corresponding ones without the additional shim. A volunteer with a clinically diagnosed cavernoma was scanned to illustrate the performance of the high-resolution B_0 maps (in-plane resolution 1.17 mm, undersampling factor of 48, slice thickness 5 mm). Another volunteer brain was scanned with a resolution of 0.76 mm and an undersampling factor of 90. Further MRFF experiments were carried out in the abdomen using a TBP of 4 and a slice thickness of 3.5 mm with an in-plane resolution of 1.03 mm.

All data were acquired on 3 T whole-body scanners (MAGNETOM Skyra, Siemens Healthcare, Erlangen, Germany)."

4.3.2 Results

"Figure 4.27 shows results in the phantom consisting of several vials separated by air. In the top row, a comparison of the gold standard values and the T_1, T_2 values obtained with MRFF using an in-plane resolution of 1.17 mm, pulses with a TBP of 8, slice thickness of 5 mm and default B_0 and B_1^+ settings are shown. The values are in good agreement. Figure 4.28 shows T_1 and T_2 values obtained from scanning the same phantom with different B_0, B_1^+, RF pulse settings, and with various resolution and slice thickness settings. In the bottom row, the coefficients of variation over the results from scans with 18 different settings are depicted for every vial. A higher variation

can be observed for T_2 than for T_1 values, the highest coefficient of variation is lower than 6%.

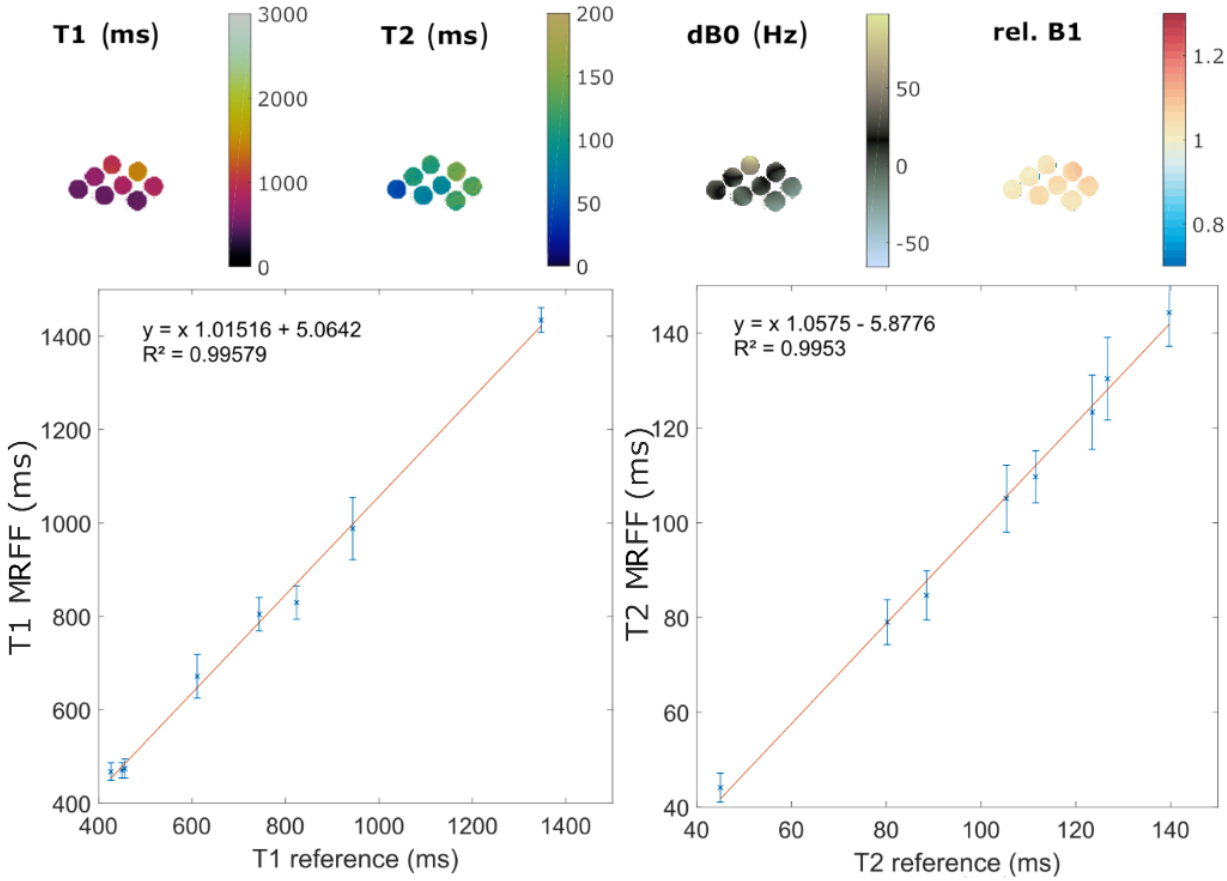

Figure 4.27: Phantom results with MRFF. The parameter maps from scanning the phantom with a matrix size of 256, FoV of 300 mm, slice thickness 5 mm using 'sinc'-shaped pulses with a TBP of 8 are shown in the top row. The comparison of relaxation parameter values with the reference are shown in the bottom. Image taken from [Kör18c].

In Figure 4.29, the results of scanning a single phantom vial using a 1D projection are shown. The B_0 gradient along the readout dimension corresponds to approximately 20 Hz per voxel. The similarity between the actual signal and the dictionary entry depends on the B_0 offset in the voxel. While the measured signal at a B_0 offset of -31.25 Hz is very similar to the best-matching dictionary entry, the measured signal with an offset of -21.88 Hz exhibits less similarity to the best-matching dictionary entry. The offset of 21.88 Hz leads to a stop band condition in the TrueFISP segment with a phase cycling of $0° - 270°$. The signal in this segment is rapidly rising for the first couple of applied flip angles and then decaying rapidly. The biggest difference during the temporal course occurs in the TrueFISP segment where this stop band condition is fulfilled. While the impact of intravoxel dispersion is rather small and temporally constant in FISP and

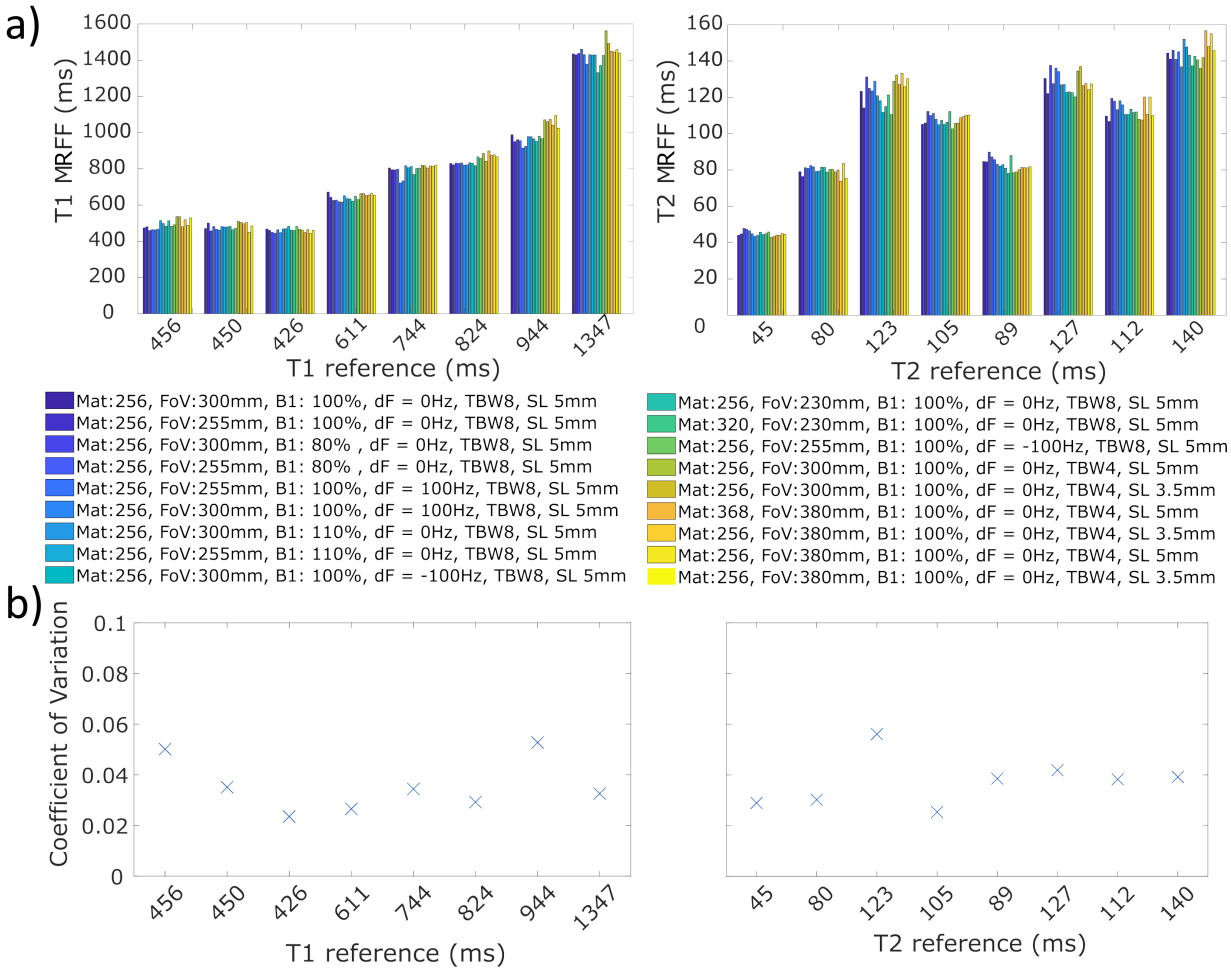

Figure 4.28: a) T_1 and T_2 values from MRFF scans with different settings. In total, 18 scans were performed using the 8 vials as shown in Figure 4.27. Different relative B_1^+ settings and global B_0 offsets were set. Various matrix sizes and different TBP products for the 'sinc'-shaped pulses and different slice thicknesses were used for the 18 scans as described in the figure legend. b) Coefficients of variation of T_1 and T_2 values over the 18 scans in each vial. Image taken from [Kör18c].

FLASH, a major impact can occur in TrueFISP under a stop band condition. The same effect can be found in a simulation. Three different fingerprints are shown in Figure 4.29 d) and e) that are generated by averaging dictionary entries with the same T_1, T_2, and B_1^+, but with different B_0 off-resonance centered at the B_0 match. The signal behavior differs substantially depending on the standard deviation of the Gaussian distribution. With broader B_0 distribution, the amplitude of the signal in the TrueFISP segment becomes smaller, similar as observed in the experiment.

The similarity of additionally synthesized fingerprints assuming different phase dispersions to

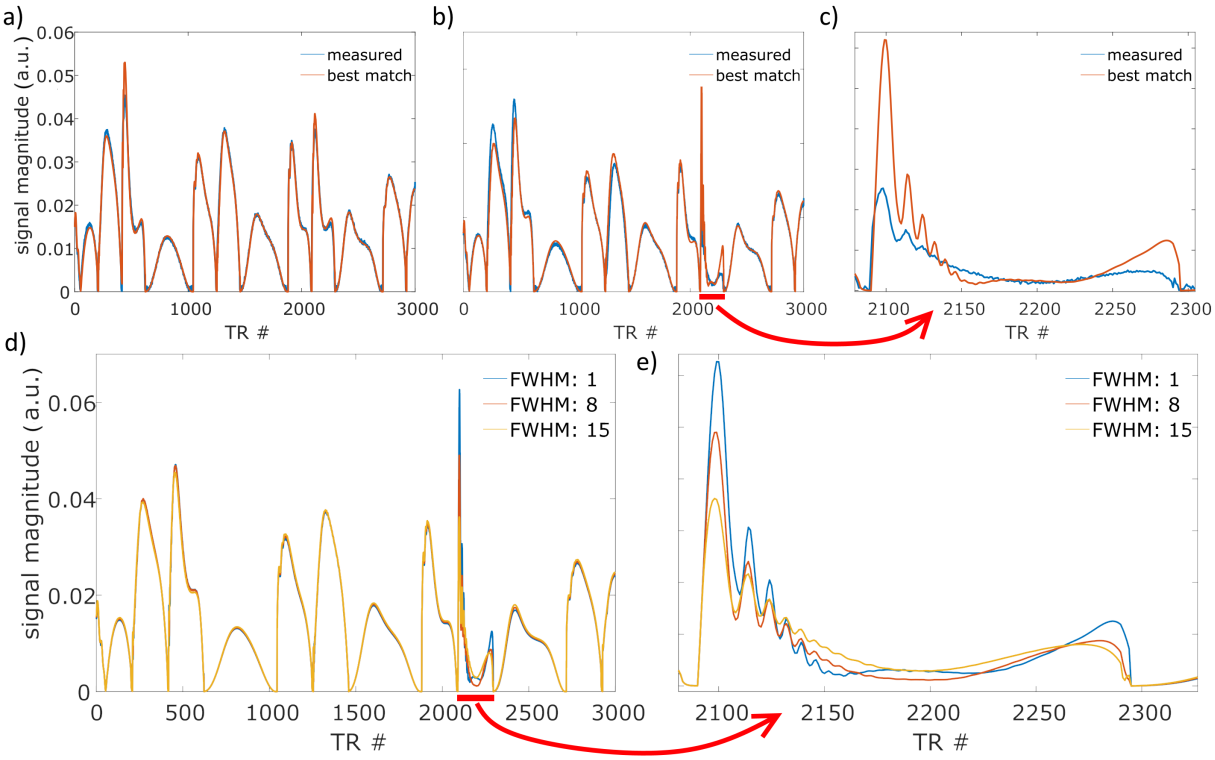

Figure 4.29: Signals from scanning a single phantom vial using a Cartesian readout without phase encoding. A B_0 gradient of 20 Hz per voxel along the readout dimension was present. In a), a signal from a voxel with a mean dB_0 of -31.25 Hz is shown; in b), a signal of the same vial but with a dB_0 of -21.88 Hz is shown. The effect of meeting the stop band condition in the TrueFISP segment with a phase cycling of 0° - 270° is visible: The best-matching fingerprint in the dictionary is less similar to the measured signal in this case, with the biggest difference occurring during the temporal course in the TrueFISP segment where the stop band condition is fulfilled. c) is showing the comparison of the measured signal and the best-matching fingerprint in this segment only. In d), three different fingerprints are shown, that are made up from adding fingerprints together along B_0 dimension according to a Gaussian distribution defined by FWHM. In e), the comparison between the three fingerprints resulting from Gaussian distributions with different FWHM is shown for the TrueFISP segment where the stopband condition is fulfilled. Image taken from [Kör18c].

their single-frequency counterparts is shown in Figure 4.30. For smaller phase dispersions, the similarity of the multi-frequency fingerprint to the single frequency fingerprint is higher for off-resonances outside the dark bands. For higher phase dispersions, this behavior changes, and higher similarity is found inside the dark band frequencies.

Figure 4.31 shows a comparison of parameter maps of MRFF with the corresponding ones from FISP-MRF with B_1^+ correction and conventional sequences for B_1^+ and B_0 mapping. Relaxation

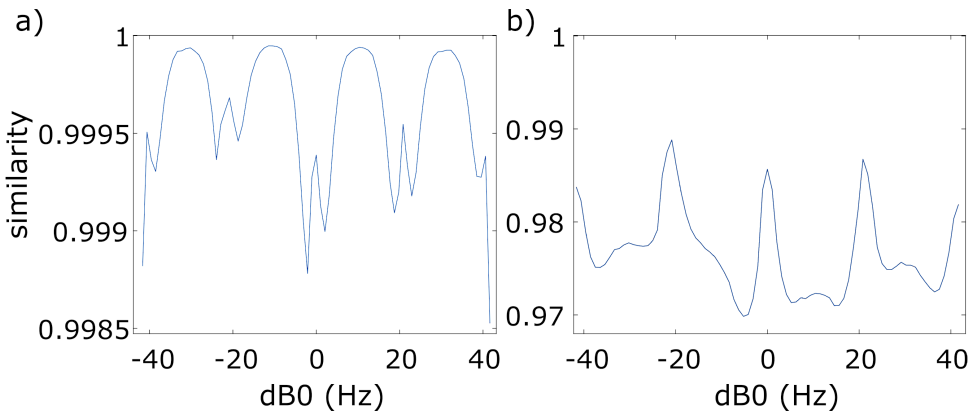

Figure 4.30: Similarity of multi-frequency fingerprints to the single-frequency fingerprint with the same T_1 (941ms), T_2 (71ms), rel. B_1^+ (1.00) and mean B_0. In a), the phase dispersion corresponds to a Gaussian distribution with FWHM of 6 Hz and in b) of 30 Hz. The similarity differs with mean B_0 of the fingerprint. For smaller phase dispersion, the similarity is high outside the dark bands, whereas for higher phase dispersion, the similarity is bigger inside the dark bands. Image taken from [Kör18c].

parameter maps are in good agreement with those from the B_1^+ corrected FISP-MRF. B_0 and B_1^+ maps show the same spatial distribution as well as similar values. Parameter values inside the nine ROIs are shown in table 4.1. The values are similar, with a tendency to higher T_1 values with MRFF.

Table 4.1: The T_1, T_2, B_0, and B_1^+ values in the nine regions of interest as positioned in Figure 4.31.

ROI #	T1 (ms)		T2 (ms)		dB0 (Hz)		rel. B_1^+	
	FISP-MRF with B_1^+ correction	MRFF	FISP-MRF with B_1^+ correction	MRFF	double echo reference	MRFF	B_1^+ reference	MRFF
1	919±43.9	950±72.7	37.3±2.0	38.6±2.6	-7.97±1.4	-4.80±1.4	0.97± 0.009	0.98±0.013
2	929±63.0	1005±87.2	37.8±2.3	36.0±3.2	-4.98±1.3	-2.44±2.0	0.99± 0.007	0.97±0.007
3	929±25.8	1022±70.7	40.5±1.4	40.5±3.3	2.18±0.6	5.90±0.8	1.06± 0.005	1.04±0.005
4	956±82.8	1050±99.7	39.1±2.1	39.1±2.5	5.31±0.7	9.22±1.0	1.04± 0.003	1.01±0.004
5	941±28.9	1003±71.1	39.7±1.3	43.9±3.1	6.56±0.3	8.36±0.7	1.09± 0.005	1.09±0.004
6	945±39.6	976±65.3	37.9±1.1	38.0±2.8	4.29±0.3	7.29±0.6	1.00± 0.002	0.96±0.003
7	1433±41.1	1479±91.0	55.1±2.1	57.1±8.0	-9.81±0.9	-4.05±1.1	0.99±0.008	0.98±0.006
8	1590±66.5	1552±108.2	64.9±6.9	62.8±13.2	-14.00±1.4	-9.60±0.9	0.94±0.001	0.96±0.002
9	1400±51.8	1346±111.5	58.9±6.2	56.3±7.1	5.80±0.6	8.33±1.1	0.92± 0.003	0.91±0.002

In Figure 4.32, the deblurring process is illustrated. The B_0 map that results from adding a linear shim in y dimension is depicted in the top right. To illustrate the performance of the deblurring, the same slice's T_1 and T_2 maps without any additional shim are depicted. With adding the shim, blurring in the parameter maps can be observed. By using the integrated spiral deblurring, the

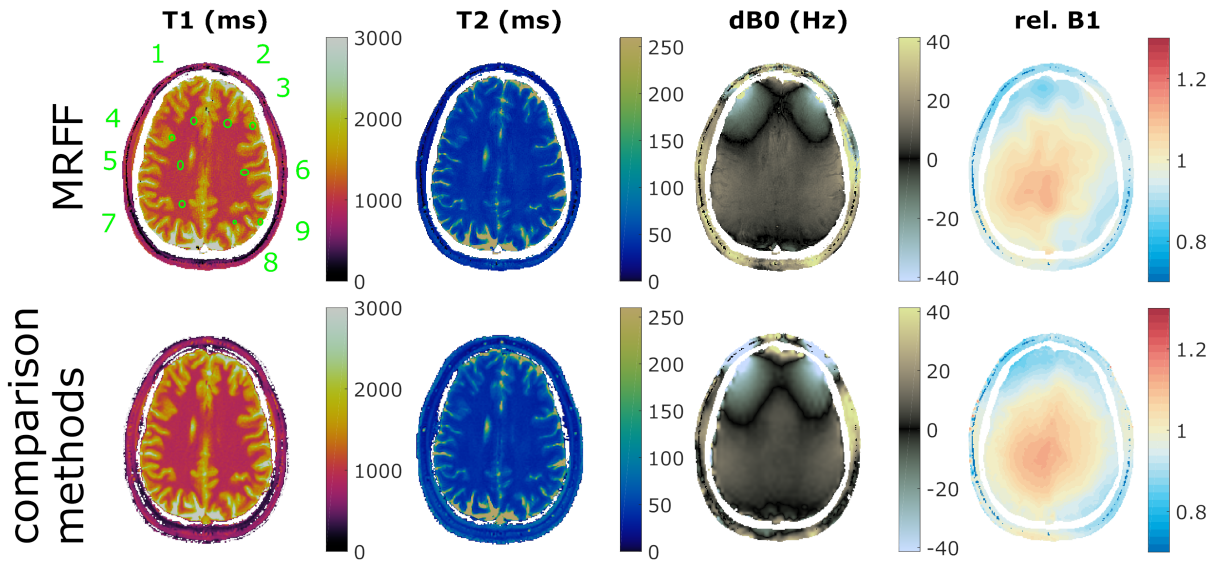

Figure 4.31: A comparison of T_1, T_2, B_0 and B_1^+ maps from an MRFF (in-plane resolution 0.9 mm, undersampling factor of 48, slice thickness 5 mm) scan and from a FISP-MRF (in-plane resolution 1.17 mm, undersampling factor of 48, slice thickness 5 mm) implementation with a B_1^+ prescan and a conventional B_1^+ and B_0 mapping method is shown. Nine ROIs were positioned on the maps as shown in the T_1 map. Corresponding values of T_1, T_2, B_0 and B_1^+ are displayed in table 4.1. Image taken from [Kör18c].

acquired images and subsequently the parameter maps can be substantially improved. A closer comparison of the blurred and deblurred parameter maps is shown in the bottom right of the Figure.

Figure 4.33 shows the results from MRFF scans on a volunteer with a cavernoma (undersampling factor of 48 resulting in an in-plane resolution of 1.17 mm, 5 mm slice thickness). The cavernoma itself is also shown zoomed-in. Higher T_1 values and lower T_2 values in the cavernoma compared to the surrounding white matter can be observed. Strong B_0 variations and intravoxel phase dispersion were also found in the cavernoma region.

The results of the high-resolution scans (undersampling factor of 90 resulting in an in-plane resolution of 0.76 mm) are displayed in Figure 4.34. T_1 and T_2 values are similar to the ones from acquisitions using an undersampling factor of 48 and exhibit no spatial biases.

MRFF results in the lower abdomen of a healthy volunteer are shown in Figure 4.35a) (undersampling factor 60, in-plane resolution of 1.03 mm, slice thickness 3.5 mm). The B_0 maps show the chemical shift between fat and water of 440 Hz at 3 Tesla. Detailed T_1 and T_2 maps of the prostate are shown in the bottom row. Increased T_1 ($\approx$ 2100 - 2600 ms) and T_2 ($\approx$ 140 - 260 ms) values in the peripheral zone can be observed compared to lower ones in the central zone (T_1: $\approx$ 1500 - 1700

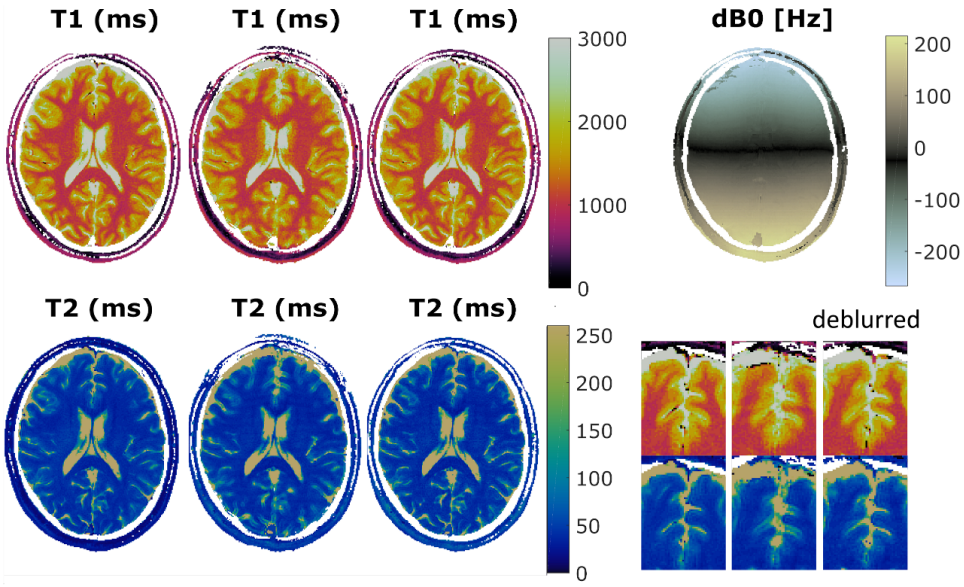

Figure 4.32: MRFF T_1 and T_2 maps in the human brain (in-plane resolution 0.9 mm, undersampling factor of 48, slice thickness 5 mm). On the left side, a comparison of T_1 and T_2 maps from an MRFF scan with and without an additional B_0 gradient in y-direction is shown. The maps on the left were reconstructed from a scan without an additional B_0 gradient. The ones in the middle are reconstructed from a scan with the additional gradient without using the integrated spiral deblurring and the ones on the right with using the integrated spiral deblurring. On the top right, the B_0 map with additional B_0 gradient from the MRFF reconstruction is depicted. Below, a zoomed comparison of the six parameter maps is shown. The effect can be best observed when regarding the thin CSF lines in the T_2 map. The resolution of the map without additional shim (left) is lost with employing the additional shim (middle) and recovered by deblurring (right). Image taken from [Kör18c].

ms, T_2: $\approx$ 45 - 55 ms). A comparison of T_1 and T_2 maps from using reconstructions with and without the deblurring step can be found on the right side of Figure 4.35b)."

4.3.3 Discussion

"A novel MRF method that is robust against varying spatial distributions of static and RF magnetic fields applied in an MR experiment is described in this chapter. Both magnetic fields can be simultaneously determined together with T_1 and T_2 relaxation parameters. T_1 and T_2 maps are subsequently less afflicted by errors resulting from inhomogeneities of the magnetic fields applied in MRI experiments which could be proven in phantom and in vivo experiments. In this work, the focus was to simultaneously quantify several parameters. Also possible would be the separate measurement of the parameters with dedicated sequences, which might result in shorter acquisition

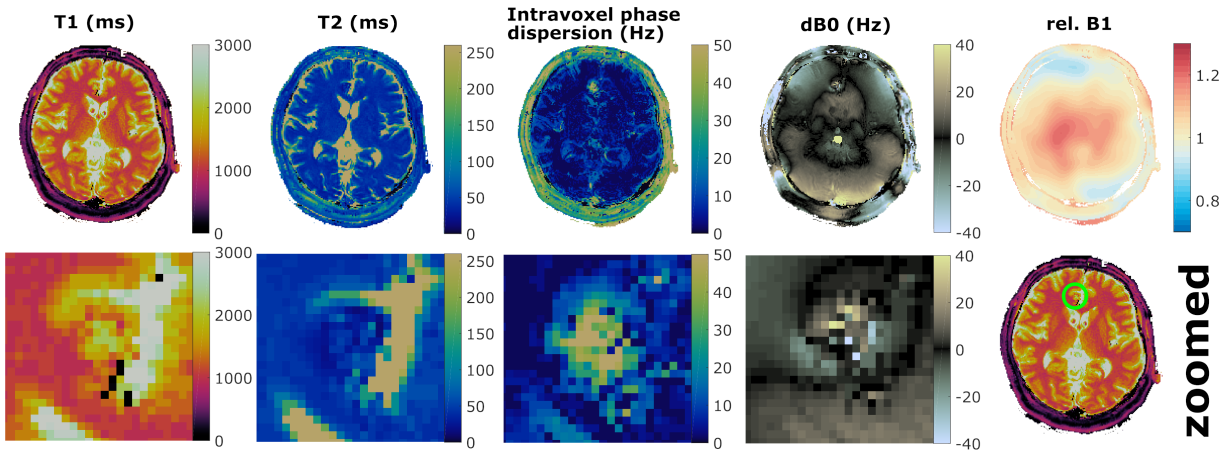

Figure 4.33: MRFF results in a volunteer's brain with a cavernoma (in-plane resolution 1.17 mm, undersampling factor of 48, slice thickness 5 mm). Besides T_1, T_2, B_0 and B_1^+ maps, the map of intravoxel phase dispersion is shown. The value of intravoxel phase dispersion corresponds to the FWHM in Hz of the Gaussian distribution of B_0 used to calculate a fingerprint that the measured signal matches best to. In the bottom row, zoomed maps of the cavernoma are depicted. Compared to normal-appearing white matter, T_1 is higher and T_2 is lower in the cavernoma. Besides that, high intravoxel phase dispersion and abrupt jumps in B_0 in the cavernoma and the surrounding tissue can be seen. Image taken from [Kör18c].

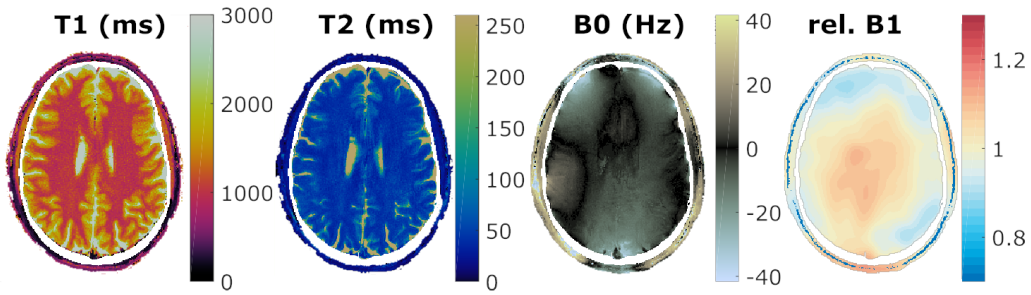

Figure 4.34: MRFF high-resolution T_1, T_2, B_0 and B_1^+ maps in the brain (in-plane resolution 0.76 mm, undersampling factor of 90, slice thickness 5 mm). Image taken from [Kör18c].

times. The downside of using dedicated, but separate, mapping sequences is a potential remaining dependency on other parameters than the one that is intended to be measured, e.g. a T_1 dependency in B_1^+ mapping methods [Chu10, Voi10]. With the MRF framework these interdependencies can be resolved by using a comprehensive signal model that tries to include relevant effects for all parameters that are supposed to be quantified. The in vivo comparison of parameter values reveals higher standard deviation in those generated by MRFF compared to the ones from MRF with a B_1^+ prescan. This is likely caused by a coarser dictionary resolution in MRFF and the higher spatial resolution. For both MRF implementations, T_1 and T_2 values in grey and white matter are

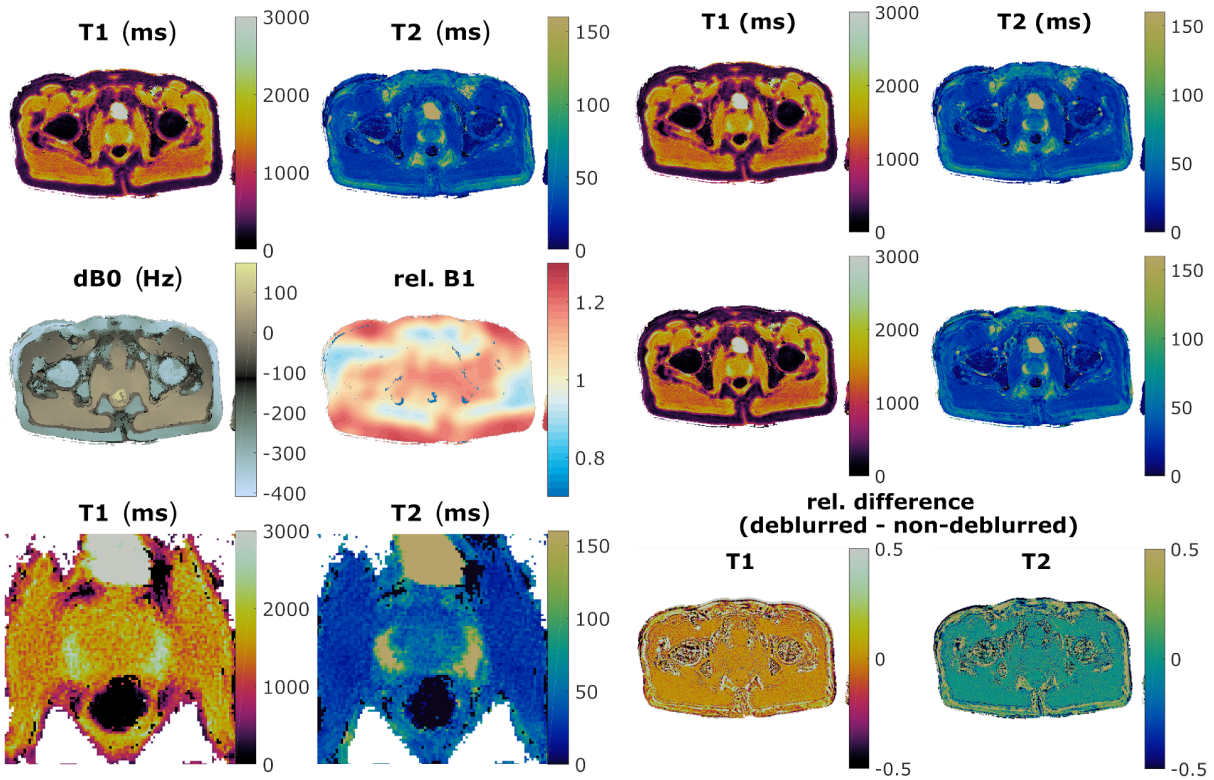

(a) MRFF (in-plane resolution 1.03 mm, undersampling factor of 60, slice thickness 3.5 mm, TBP 4) results in a volunteer's prostate. T_1, T_2, B_0 and B_1^+ maps as well as zoomed T_1 and T_2 maps of the prostate with fat masked out by off-resonance are shown.

(b) MRFF (in-plane resolution 1.03 mm, undersampling factor of 60, slice thickness 3.5 mm, TBP 4) results in a volunteer's prostate from the same experiment as shown in a). Besides the T_1, T_2 maps (top row) from using the reconstruction with the deblurring step the corresponding ones with omitting the deblurring step are shown in the middle row, as well as the relative difference in the bottom row.

Figure 4.35: MRFF results in a volunteer's prostate. Image taken from [Kör18c].

smaller than previously published ones generated with spin-echo based mapping techniques. For white matter, T_1 values in the range of 950 ms - 1050 ms and T_2 values of 36 ms - 44 ms were found in this work. In grey matter T_1 values range from 1350 ms to 1550 ms and T_2 values from 55 ms to 65 ms. Spin-echo based methods suggest a T_1 in white matter of 800 - 860 ms and a T_2 of 55 ms to 65 ms. In grey matter T_1 values from spin-echo based methods range from 1000 ms to 1500 ms and T_2 values from 59 ms to 74 ms [Lia17, BE15, Jia16a]. A collocation of relaxation times measured with various techniques can i.a. be found in [Wan99, Boj17].

The method presented here shares some similarities with methods that either also use a combination

of several sequence types for an MRF implementation [Clo16, Han17] or are able to quantify B_1^+ and B_0 simultaneously with relaxation parameters [Ye18]. As B_1^+ mostly influences T_2 in MRF [Ma17a], it is essential to simultaneously quantify them together, which is achieved with the method described here. A further distinctive characteristic of the implementation is the integration of TrueFISP parts which allows for quantification of B_0 and intravoxel phase dispersion with a single echo per TR.

The high-resolution B_0 maps that are generated by the method proposed here can be further utilized. One drawback of spirals is their sensitivity to off-resonance. B_0 maps can be employed to deblurr the measured data and thus to create sharper parameter maps. It should be noted that the B_0 map resulting from the here proposed method is calculated on the blurred data which also leads to a blurred B_0 map. A possible solution for refining the B_0 map would be to implement an iterative process. After each determination of the B_0 map, the images are deblurred and again a B_0 map is calculated. A similar process could be implemented for the estimation of the B_1^+ map. Since T_1 and T_2 values are influenced by B_1^+, several iterations of the 3. and 4. matching steps could be iterated several times to improve the accuracy of the estimates of T_1, T_2 and B_1^+. Since this process mainly affects estimates in CSF regions and deviations are possibly related to flow effects this approach was not further investigated in this study. As the measured B_0 and the phase dispersion in the voxel are associated with the susceptibility of the tissue, this information can potentially aid in diagnosis [Haa04]. This was exemplarily shown in a brain scan of a volunteer with a cavernoma, where the B_0 and phase dispersion maps hint susceptibility differences in the tissue [Cam10]. Another finding concerning intravoxel dephasing effects on MRF values was made. While a high intravoxel phase dispersion only scales the signal in FISP- and FLASH-based MRF, it can have a strong impact on TrueFISP signals [Ass17,Chi17]. A particularly strong impact can be observed on the TrueFISP signal when the stop band condition is met. By also matching the phase dispersion, this effect that is mostly influencing T_2 values can be alleviated. A Gaussian distribution was chosen for the intravoxel phase distribution, but also other distributions, such as a Lorentzian or a simple uniform distribution could be used [Mul15]. Since the phase distribution inside a voxel is generally unknown and depends on a lot of factors, the Gaussian distribution was chosen as a very general approach. Furthermore, the quality of the phase dispersion map might depend on the off-resonance in MRFF. The influence of intravoxel dispersion differs among off-resonances. A stronger effect in the TrueFISP bands will probably be better to identify than a smaller one where the stop band criterion is not met.

Even though the influence of spatial inhomogeneities of magnetic fields on MRF parameter maps can be substantially reduced, other effects have an impact on the results. In general, MRF as well

as other quantitative MRI methods are susceptible to quantification errors by all parameters that are not included in the signal model. A different strategy than including different parameters is to decrease the sensitivity to confounding factors. This can be done e.g. for B_1^+ by using adiabatic [Ham16] pulses that yield similar results over a broad range of B_1^+. A modification of this strategy is to limit a parameter dimension. By employing a constant TR, the B_0 range could be limited substantially in this study. In this work, it is also assumed that further physiologic effects such as diffusion [Hod18] and perfusion can be neglected.

The influence of motion on MRF experiments is ideally believed to be small [Ma13] since the pattern recognition approach is supposed to ”see through” artifacts arising from undersampling as well as from motion. However, spins moving in and out of the slice during the acquisition may still be a problem. For movement like the pulsation of CSF in the brain, it was observed that the resulting T_1 and T_2 values are not as stable as in solid parts of the brain [Jia15]. Several studies have also shown that especially through plane motion is able to alter MRF results [Yu17b, Kör18b, Cru18]. Another issue that is discussed in the context of MRF is magnetization transfer (MT) [Hil17]. The severity of this effect is correlated with RF power. In order to investigate potential effects, two different 'sinc'-shaped pulses with a TBP of 4 and 8, respectively, exhibiting different RF power at equivalent flip angles were compared. In the scope of the experiments with agarose filled tubes, no differences in T_1 and T_2 estimates from MRFF experiments using TBP 4 and TBP 8 were found. A future step will be a comparison of MT effects in vivo.

A distinct benefit of the MRF idea is that computationally demanding calculations can be carried out before the experiment. This yields the possibility to simulate MR signals - on a macroscopic level - with high detail. Dictionaries that have been used here have an uncompressed size of more than 100 GB, and the simulation process takes almost a week on a fast computer. While this is a time-consuming task, the matching process takes less than a minute with compressed data and FLANN [Cli17], a fast search algorithm. Maintaining reasonable reconstruction times with increased dictionary resolution could still become a challenge. Besides fast matching algorithms such as FLANN or FGM [Cau15], machine-learning-based methods [Hop17, Our, Fan17] could help in reducing the dictionary storage size and computational effort.

An attractive future step is the extension of the proposed method to a 3D implementation. As has been shown for the FISP version [Ma17b], undersampling in z-dimension can be employed to shorten acquisition times. A combination of MRFF with recently suggested methods for accelerating 3D MRF implementations like using a sliding window reconstruction [Lia17] or spiral projection [Cao18] could potentially lead to a significant speedup. Furthermore, the usage of iterative [Cli17, Pie16] or low-rank methods [Ass18, Zha15] could improve the quality and

robustness of the proposed technique. With such methods, the sequence duration might also be shortened without losing robustness. The flip angle pattern used here is very similar to the one used in FISP-MRF. The order of the sequence types in MRFF was chosen arbitrarily. However, since low flip angles are applied during the FLASH segments, the magnetization can relax during these periods. Therefore it is probably beneficial to distribute those segments throughout the sequence. The design of an optimal experiment for MRF has been targeted with optimization methods [Bo 16, Ham15b], which is computationally even more demanding with an increased number of degrees of freedom."

4.3.4 Conclusion

"With the proposed method, T_1, T_2, B_0 and B_1^+ maps can be simultaneously quantified with a single continuous MR experiment. Resulting B_0 maps can be utilized for integrated spiral deblurring and potentially also for diagnosis. The method was applied and evaluated in phantoms as well as in the human brain and lower abdomen. Results show that generated parameter maps are robust to B_0 and B_1^+ influences."

5. Reproducibility of Magnetic Resonance Fingerprinting

So far there is only little literature that investigated the reproducibility of quantitative MRI measurements. Reproducibility studies have been published for volumetric MRI in the brain [Jov13] or on diffusion [GS15] but rarely for relaxation parameter measurements. However, statistical data on reproducibility and repeatability of any quantitative method is essential for its clinical application. When associating a disease with certain tissue parameters or differentiating healthy from pathologic tissue parameters, the measurement uncertainty has to be taken into account. For FISP-MRF, a repeatability assessment of T_1 and T_2 values in the NIST system phantom has been performed in phantoms, which showed a high repeatability [Jia15].
In this work, the repeatability and reproducibility of a FISP-MRF implementation including several improvements that were developed in the previous chapters (acquiring a separate B_1^+ map, using an additional dephaser with an 8π dephasing moment over the slice, employing the STEP-11 reordering) were evaluated in vivo. The presented results might aid in estimating the feasibility of clinical applications that employ MRF in longitudinal or multicenter studies. The content of this chapter has previously been published as a journal article [Kör19a]. Verbatim copies of text passages are marked with quotation marks.

5.1 Methods

Sequence

"The study was performed using a prototype implementation of a 2D slice-selective FISP-MRF sequence that generates T_1 and T_2 maps by matching measured signals to a set of pre-simulated signals which is called a dictionary as previously described [Jia15]. After the application of an adiabatic inversion pulse, a series of 3000 echoes was acquired with both varying flip angles and repetition times. A dual-density spiral trajectory was designed for a field of view of 300mm, a matrix size of 256 and an undersampling factor of 24 in the center of k-space with a transition to 48 in the peripheral regions of k-space. The trajectories are corrected using a one-time calibration and a generalized eddy-current model by Tan and Meyer [Tan09]. Spiral trajectories were rotated

by 82.5° between successive repetition times as described in the previous chapter. In addition to the unbalanced gradient moment in slice selection direction, an additional gradient (8π dephasing moment) was applied at the end of each repetition time to mitigate local off-resonance effects as described in the previous chapter. Additional B_1^+ mapping [Chu10] was acquired to mitigate bias arising from B_1^+ inhomogeneities. The acquisition time for each slice was 41 seconds for MR Fingerprinting and 20 seconds for B_1^+ mapping of the whole examined volume.

Reconstruction

The dictionary consists of fingerprints with T_1 values from 10 ms to 4500 ms, T_2 values from 2 ms to 3000 ms and B_1^+ values (specified as relative to the nominal B_1^+ value) from 0.6 to 1.4 in 0.01 steps. Bloch simulations employed 200 isochromats for taking slice profile effects into account ('sinc'-shaped pulses with a time bandwidth product of 8, slice thickness of 5 mm). The dictionary was compressed using singular-value decomposition [McG14]. The relative B_1^+ value was used to voxel wise select the corresponding subset of the whole dictionary for the matching process. Relative proton density maps were derived from the measured signals' magnitude [Ma13].

Study Setup

Healthy volunteers were scanned on ten different 3-Tesla scanners (6x MAGNETOM Skyra, 2x MAGNETOM Prisma, 2x MAGNETOM Prisma^{fit}, Siemens Healthcare, Erlangen, Germany). Table 5.1 shows which volunteer was scanned at which scanner. Scans were performed between July 2017 and January 2018, each during 10 a.m. and 6 p.m. local time. All scans were performed using a 20 channel head coil.

Scanner Volunteer	**Erlangen Prisma^{fit}**	**Erlangen Skyra A**	**Erlangen Skyra B**	**Erlangen Prisma**	**Erlangen Skyra C**	**Vienna Prisma**	**Vienna Prisma^{fit}**	**Cleveland Sykra A**	**Cleveland Sykra B**	**Essen Skyra**
1	x		x	x	x					
2	x	x	x	x	x	x	x	x	x	x
3	x		x	x	x					
4	x	x	x	x	x	x	x	x	x	x
5		x	x	x	x	x	x			x
6		x	x	x	x	x	x			x
7		x	x	x	x					
8		x	x	x	x					
9		x	x	x	x					
10		x	x	x	x					

Table 5.1: Matrix indicating which volunteers were scanned on which scanner

The protocol was set up to cover seven slices with an in-plane resolution of 1.17 mm and 5mm thickness in a total scan time of 5:10 minutes including the B_1^+ prescan. Each measurement of this protocol was preceded by an Auto-Align Scout for automated, landmark-based slice positioning to

account for movement between the scans. Each volunteer was scanned four times on one scanner.

Evaluation

Reconstructed parameter maps were registered before further evaluation. The voxel-wise coefficients of variation (CoV) were calculated across all scanners and repetitions for skull-stripped proton density, T_1 and T_2 maps of all volunteers. Masks for compartments such as cerebrospinal fluid (CSF), grey matter white matter, and several structures were manually segmented on the parameter maps from a single scan per volunteer. The derived masks were applied to all corresponding scans. To account for potential spatial inhomogeneities in the parameter maps (described in a previous chapter) that could be averaged out in large compartments, four additional ROIs were confined to small contralateral white-matter regions of each slice. Figure 5.1 shows the positioning of these ROIs in seven representative slices. The mean value as well as the average standard deviation over volunteers in a segmented region and the standard deviation of the mean value across volunteers were calculated.

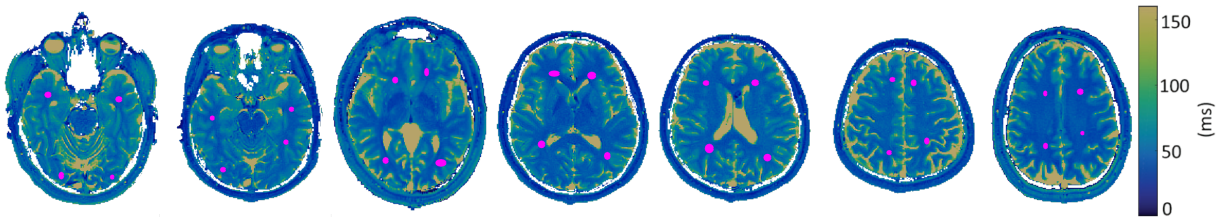

Figure 5.1: T_2 maps of seven slices of different volunteers with exemplary positioning of the ROIs in white matter. Image taken from [Kör19a].

Statistical Analysis

For each tissue compartment in every scan, mean, median and percentile as location parameters of the distribution were calculated for T_1 and T_2. To examine the deviation between these location parameters from different scanners (inter-scanner deviation), a mean value $\bar{X}_{i,j}$ of a location parameter was first calculated over each four repetitions on a scanner for one volunteer and one compartment. This was then compared to the corresponding mean $\bar{X}_i$ over all scanners yielding a data point that has a mean absolute value $\bar{X}_i$ and a relative deviation $Y_{i,j}$ as defined in equation 5.1. Here, i indexes a tissue compartment, i.e. running over volunteers and compartments in a volunteer, and j indexes the scanner.

$$Y_{i,j} = \frac{\bar{X}_{i,j} - \bar{X}_i}{\bar{X}_i} \tag{5.1}$$

The found inter-scanner deviation was used to estimate the required sample size n needed to detect a desired percentage difference δ with 90% power and an α error of .05 as described by Machin et al [Mac11]. With the formula:

$$n = f(\alpha, P) \cdot \sigma^2 \cdot 2/\delta^2 \tag{5.2}$$

the sample size was calculated, with P the study power and σ the inter-scanner standard deviation. The scanner-specific repeatability (intra-scanner deviation) was assessed similarly. For every scanner the relative deviation $Z_{i,j,k}$ of one compartment's value $X_{i,j,k}$ in one repetition was calculated against the corresponding mean $\bar{X}_{i,j}$ over the four repetitions (equation 3). The index k denotes the repetition.

$$Z_{i,j,k} = \frac{X_{i,j,k} - \bar{X}_{i,j}}{\bar{X}_{i,j}} \tag{5.3}$$

The calculation of the inter- and intra-scanner deviations is schematized in Figure 5.2. Confidence intervals were calculated per compartment and location parameter. Average values of T_1 and T_2 in solid tissue compartments were calculated for all MAGNETOM Skyra and Prisma scanners separately and compared."

5.2 Results

"Ten healthy volunteers (age 28.5±6.9 years, 8 men, 2 women) participated in the study. The mean T_1 and T_2 values in the segmented ROIs and their respective standard deviations are presented in Table 5.2. Standard deviations inside the ROIs are higher than the standard deviation of the mean value over volunteers. Maps of the CoVs for T_1 and T_2 in all scanned slices of all volunteers are displayed in Figure 5.3. The CoVs in regions containing cerebrospinal fluid (CSF) is much higher than in solid matter regions. On average, the CoV in brain tissue regions is twice as high for T_2 than for T_1. Boundary regions between different brain tissues exhibit higher CoV than large contiguous regions consisting of the same tissue. In one volunteer (No. 8), a spatial gradient in anterior - posterior direction can be observed in the T_2 CoV map. The map of the CoV of Proton density is displayed in Figure 5.4. The proton density maps exhibit high variation and were not analyzed in more detail.

Bland-Altman plots showing the reproducibility (inter-scanner variation) of the mean T_1 and

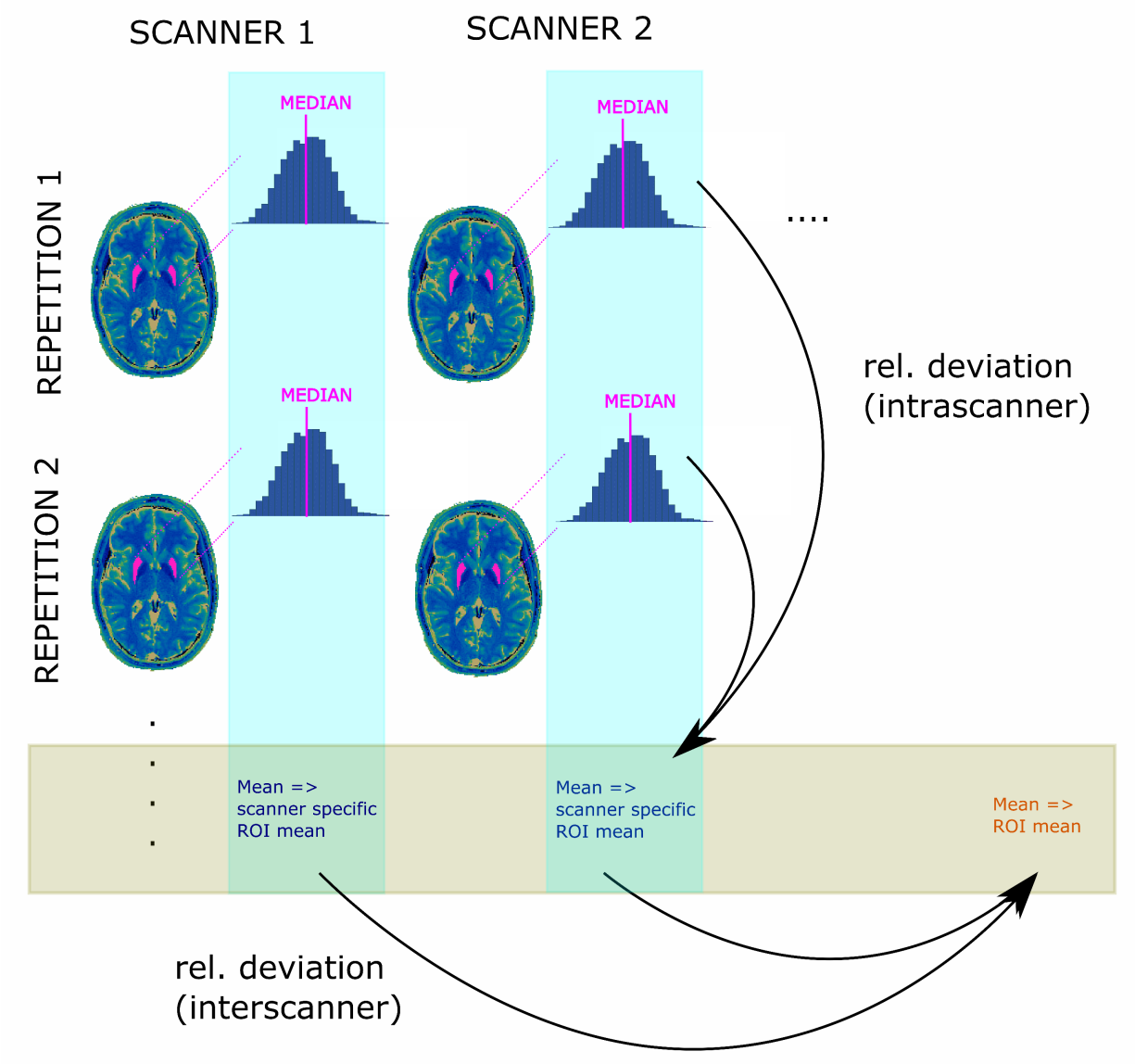

Figure 5.2: Schematic illustration of the process of calculating the relative deviations and means is exemplarily depicted for the median T_2 value in the putamen of one volunteer. The mean value of the median is calculated over four repetitions on one scanner. The mean of this average is likewise calculated over all scanners this volunteer was scanned on yielding a global mean of the median value of T_2 in the putamen of this volunteer. The relative deviation of the average median value on one scanner against the average median value over all scanners gives the inter-scanner variation. Likewise, the relative deviation of the median value from one repetition against the average median value over all repetitions on one scanner gives the intra-scanner variation. Image taken from [Kör19a].

T_2 values in different brain tissue compartments are depicted in Figure 5.5. These plots show

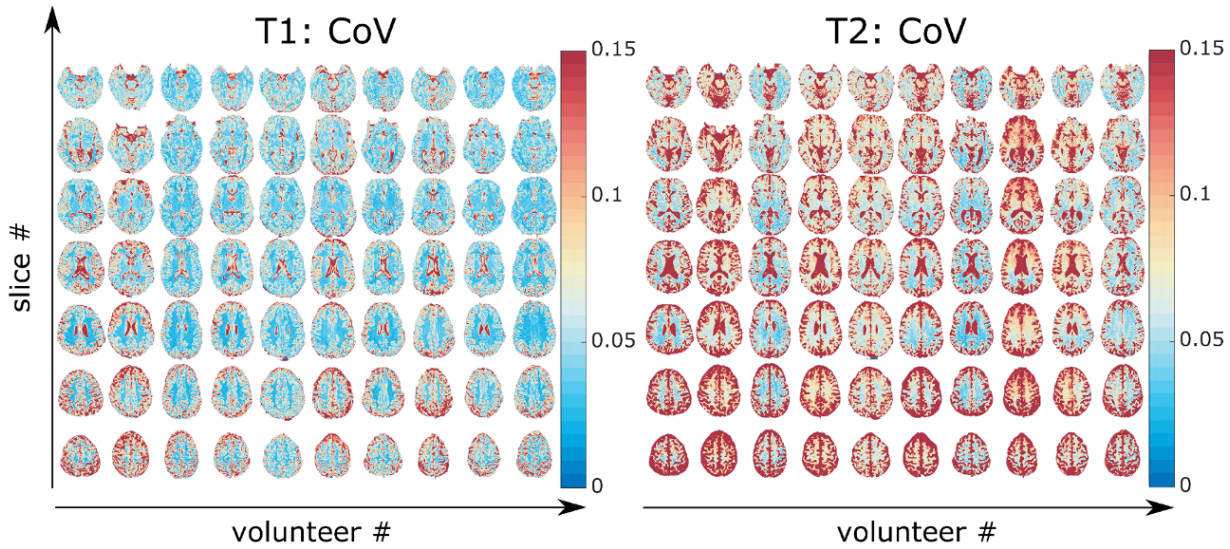

Figure 5.3: Coefficient of Variation of all scanned slices in this study for T_1 and T_2 (skull-stripped). Along the y axis different slices are shown and along the x axis the different volunteers. Image taken from [Kör19a].

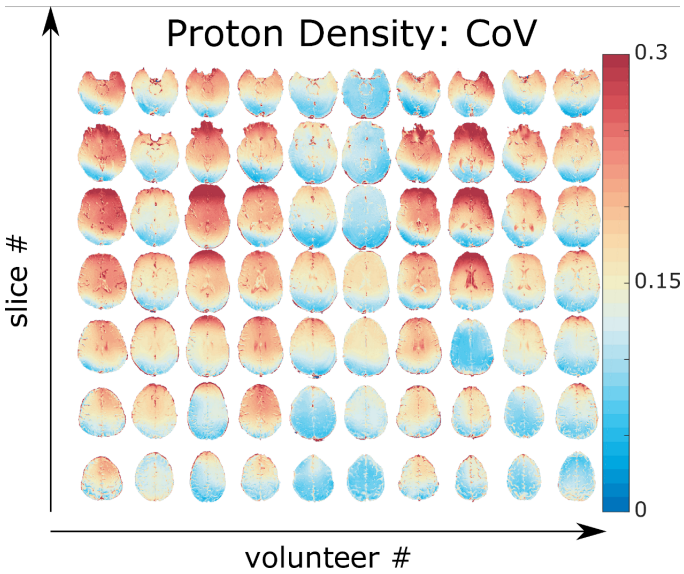

Figure 5.4: Coefficient of Variation of all scanned slices in this study for proton density (skull-stripped). Along the y axis different slices are shown and along the x axis the different volunteers. Image taken from [Kör19a].

both the distribution of the mean values of the different compartments as well as the deviations and their confidence intervals. Mean T_1 values range from 820 ms to 1450 ms with two clusters for white matter and grey matter regions. The confidence interval of the distribution of relative deviations to the mean has its boundaries at 3.4%. For T_2, the ROI values range from 25 ms

	$\overline{T_1}(ms)$	$\sigma_{\overline{T_1}}(ms)$	$\overline{\sigma_{T_1}}(ms)$	$\overline{T_2}(ms)$	$\sigma_{\overline{T_2}}$	$\overline{\sigma_{T_2}}(ms)$
GM	1372	12.5	144.6	52.7	0.7	9.0
Frontal GM	1385	22.1	146.5	55.6	1.2	8.5
Temporal GM	1397	13.2	147.8	53.2	0.9	8.5
Parietal GM	1360	26.9	148.2	51.1	0.7	9.2
Occipital GM	1368	17.3	161.3	53.6	0.8	12.0
Insula GM	1398	37.2	133.7	52.6	0.9	9.3
Thalamus	1286	26.3	77.7	45	2.4	3.6
Caudate Nucleus	1359	31.1	63.7	50.1	2.8	3.3
Putamen	1266	35.8	61.7	45	2.7	4.1
WM	954	15.4	64.4	38.7	0.9	3.1
Frontal WM	933	16.5	63.4	37.7	1.2	2.9
Temporal WM	954	16.7	65.5	38.7	1.1	2.6
Parietal WM	946	16	58.1	39.4	0.9	2.9
Occipital WM	980	18.5	66.8	39.9	0.7	2.9
Pallidum	1008	43.6	49.1	29.1	2.2	1.9
Corpus Callosum	871	21.2	44.0	33.9	0.9	3.0
CSF	2330	69.5	604.7	213.9	22.9	165.9

Table 5.2: Measured T_1 and T_2 values in the segmented tissue compartments. The mean value ($\overline{T_1}$ and $\overline{T_2}$), the standard deviation of the mean value over volunteers ($\sigma_{\overline{T_1}}$ and $\sigma_{\overline{T_2}}$) and the average standard deviation in an ROI ($\overline{\sigma_{T_1}}$and $\overline{\sigma_{T_2}}$) are displayed.

to 55 ms, also showing two clusters for white and grey matter compartments. The confidence interval has its boundaries at 8.0%. The half widths of the confidence intervals, mean values, median and percentiles for every compartment are shown in Table 5.3. To detect a 5 % change with 90% power and an α error of .05, a sample size of 14 is required for T_2 and 3 for T_1 using the interscanner standard deviation from figure 5.5.

Scanner-specific repeatability (intra-scanner variation) plots are displayed in Figure 5.6 for mean T_1 and T_2 values in solid tissue compartments. The scanner with the highest repeatability and the one with the lowest repeatability according to the confidence intervals for solid tissue T_1 and T_2 are shown. The half widths of the confidence intervals of the mean values in every compartment are shown in Table 5.4 for all scanners. Confidence interval boundaries for T_1 were lower than 5.2% in brain tissue regions for all scanners. For T_2, the confidence intervals were wider with half widths of up to 12.3%. High deviations could especially be observed in one particular scanner ("ERL Skyra A"). When not taking into account this scanner, the highest half width of a confidence interval in a solid matter compartment was 8.8%.

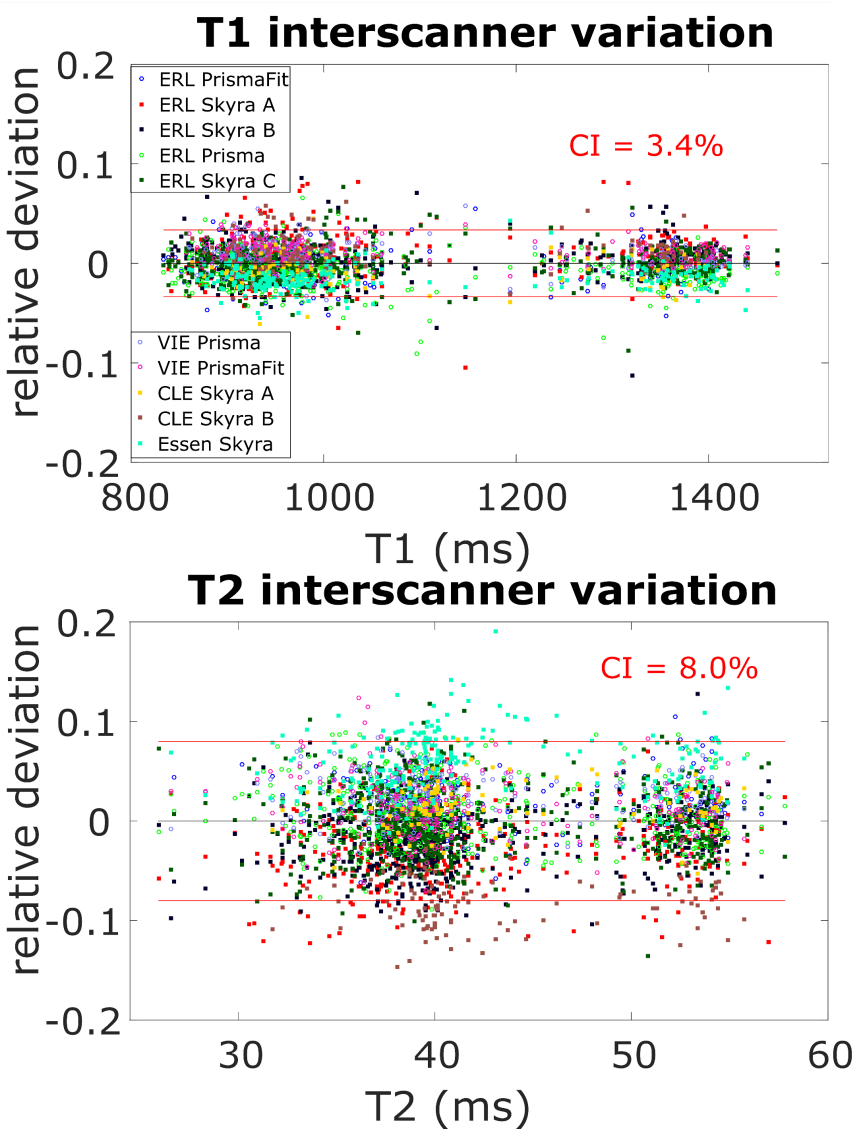

Figure 5.5: Inter-scanner variation of the mean T_1 and T_2 value in all solid matter compartments. Different colors are indicating different scanners. The symmetric confidence intervals which are located at 1.96 times the standard deviation of the distribution are additionally plotted in the graphs. For the T_1 mean value in solid tissue, the confidence intervals are $\pm 3.4\%$ and for T_2 $\pm 8.0\%$. Image taken from [Kör19a].

Results from MAGNETOM Skyra and MAGNETOM Prisma systems are compared in Figure 5.7. No offset exists for the relative deviations of T_1 values; for T_2 the MAGNETOM Prisma relative deviations had a mean relative deviation of 1.1% which implicates a mean offset of 2.3% between MAGNETOM Skyra and Prisma systems in solid tissue T_2 values."

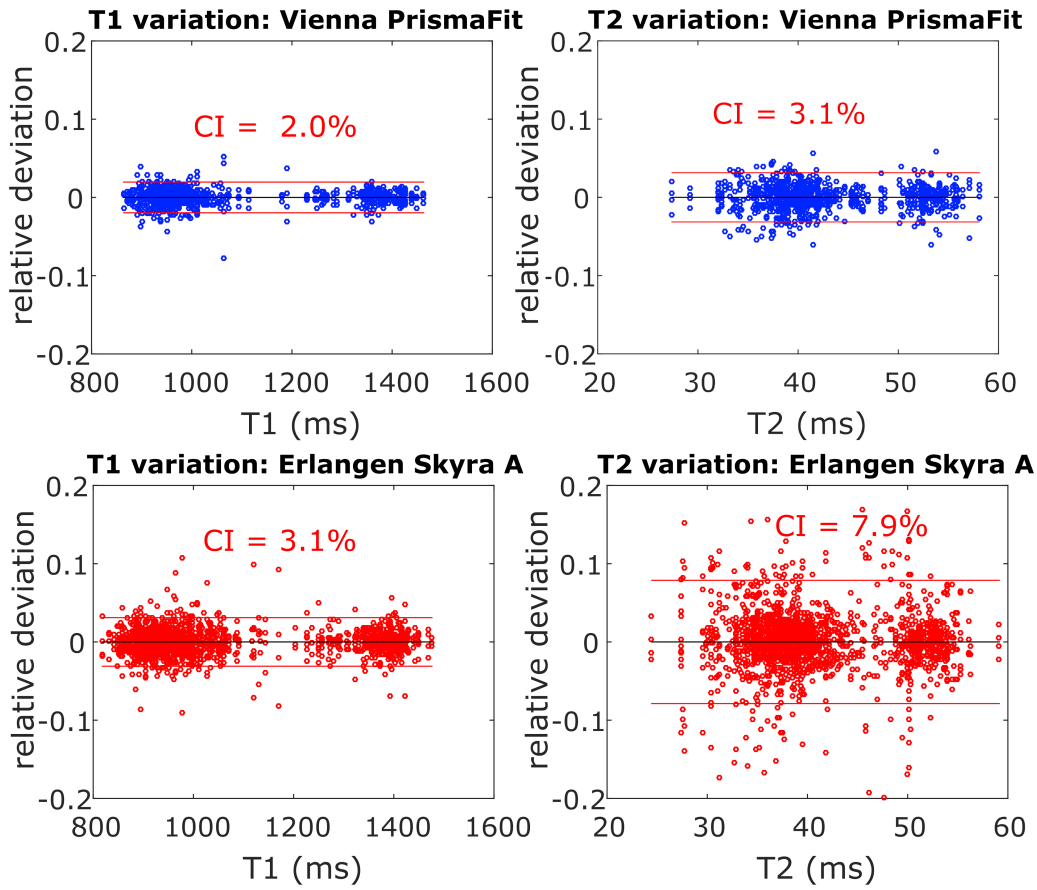

Figure 5.6: Intra-scanner variation of the mean T_1 and T_2 value in all solid matter compartments, for the scanner with the highest and smallest repeatability in this study. The symmetric confidence intervals which are located at 1.96 times the standard deviation of the distribution are additionally plotted in the graphs. In the scanner with the best repeatability, the confidence intervals for the T_1 mean value in solid tissue are located at $\pm 2.0\%$ and for T_2 at $\pm 3.1\%$. For the scanner with the worst repeatability, the confidence intervals for the T_1 mean value in solid tissue is located at $\pm 3.1\%$ and for T_2 at $\pm 7.9\%$. Image taken from [Kör19a].

5.3 Discussion

"The goal of this study was to estimate the in vivo repeatability and reproducibility of an MR Fingerprinting protocol under well-controlled conditions. The found precision can be used to estimate the significance of measured relaxation time differences in longitudinal or multicenter studies (e.g., to calculate the required sample size necessary to detect a clinically significant change

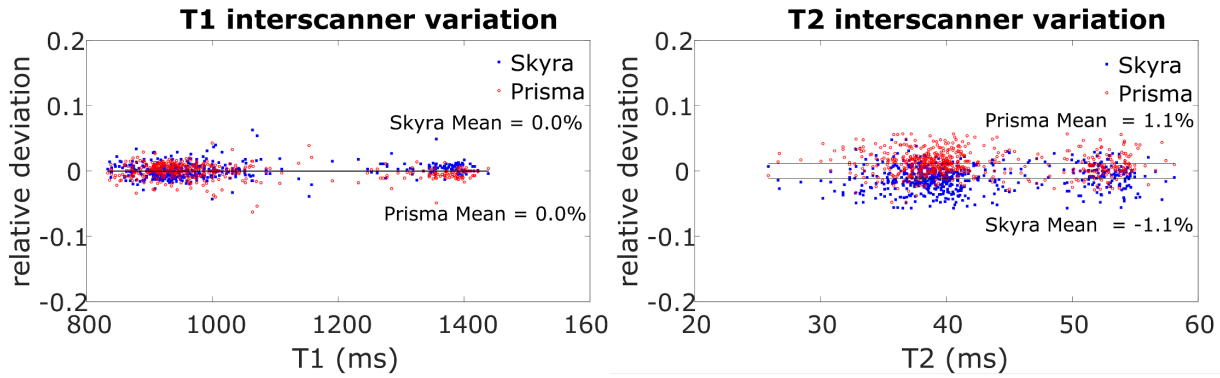

Figure 5.7: Difference of the mean T_1 and T_2 value between two scanner types in all solid matter ROIs. For the T_1 mean value in solid tissues no significant difference can be observed, while an average offset of 2.3% can be observed in T_2 (horizontal lines). Image taken from [Kör19a].

based on the precision) [Sym16]. Results suggest a reasonable repeatability and reproducibility of T_1 and T_2 relaxation times of volunteer brains generated with MR Fingerprinting. However, results differ substantially between solid compartments (interscanner variation $< \pm 8.0\%$) of the brain and CSF (interscanner variation $< \pm 18.2\%$). The voxel-wise coefficient of variation (CoV) of parameter maps show that the variation in both T_1 and T_2 is higher in CSF than in solid brain tissue. Average relaxation times as measured in this study are T_1 of 954 ms and T_2 of 39 ms in white matter and T_1 of 1372 ms and T_2 of 53 ms in grey matter. For T_1 values, no offset could be observed between measurements performed on MAGNETOM Skyra and Prisma systems. For T_2 values, an offset of 2.3 % was seen, likely caused by scanner imperfections related to certain system characteristics (eg, different eddy current behavior).

Similarly to the results of the repeatability study performed on the NIST/ISMRM phantom [Jia16b], in this study also a higher T_2 than T_1 variation was found. Overall, the variation found in the presented in vivo study is higher than in the phantom study. This is supposedly due to the more complex experiment of scanning a volunteer compared to a phantom. Also, relaxation times determined in vivo are highly dependent of the technique used for measurement. The best approximation of a ground truth can probably be performed with single spin echo measurements, since they are not contaminated with stimulated echo signals. However, these are highly time consuming and may still be affected by other effects than relaxation processes, depending on the applied sequence. Average T_1 values in this study in white matter and grey matter agree with spin-echo based measurements that suggest T_1 values of 800 to 860 ms in white matter and 1000 to 1500 ms in grey matter [Lia17, BE15, Jia]. The T_2 values found in white matter and grey matter are substantially shorter than in spin echo based T_2 mapping techniques, which suggest higher T_2

in white matter (55 to 65 ms) and grey matter (59 to 74 ms) [Lia17, BE15, Jia]. The comparison to spin echo based mapping literature values is summarized in the Table 5.4. Relaxation times found in CSF in the presented study are also within the previously reported range [Con87], but likely too short due to flow effects. An overview of literature T_1 and T_2 values measured in the brain with various methods has been covered in previous studies [Boj17].

Study limitations

The more thorough analysis was limited to brain tissue for several reasons. First of all, relaxation parameters in pure fluids are rarely used for clinical diagnosis. Second, the pulsation of CSF is not included in the signal model of the MR Fingerprinting implementation. Deviations in signal evolutions caused by pulsation or flow therefore lead to mismatches. Since these mismatches do not result in a constant bias, this hints that the fluid motion is different from scan to scan and thus manifests as high CoV in the results. Interestingly T_1 seems to be less afflicted by pulsation than T_2. This could be due to the inversion pulse that the MR Fingerprinting sequence begins with and leads to a high T_1 sensitivity restricted to a short amount of time after the pulse application. First work has been presented on signal models including flow effects [Fla18], which is an interesting approach not only for quantifying the motion of fluids but also for generating more stable results in fluids.

The inter-scanner variation found in this study was composed of both methodologic and physiologic causes. A variation of relaxation parameters over time in the brain can be suspected. A previous study showed that even in same-day measurements, physiological variations can manifest as statistically significant morphological changes in the brain [Aar17]. The scans for this study were carried out at slightly different times of the day but, more importantly, shortly after long travels. All the potential physiologic variation subsequently adds to the inter-scanner variation, which is not only caused by methodologic issues. Nonetheless, there are also differences in the results arising from the method itself. Potential causes for methodologic variations include spiral trajectory deviations and scanner adjustment differences caused by different patient positioning. Varying transmit power adjustments are addressed by the B_1^+-field correction. However, any hardware-induced drift of transmit or receive signals during the scan may affect results. Variations from repetitions on a single scanner are smaller than the variation between scanners. Physiologic variation can be ruled out as a statistically significant cause for deviations in relaxation parameters in this study due to the restricted time of each scan session. Consequently, the deviations are solely caused by movement between the scans and scanner imperfections. Since MR Fingerprinting results rely on the underlying signal model, every effect that is not included in the model potentially alters results. One of the effects intrinsic to MRI is motion. Substantial deviations can occur

with strong and abrupt motions as observed in CSF. Other studies have found that through-plane motion can alter the results, but MR Fingerprinting is robust to inplane motion [Yu17b].
Although substantial effort was spent to ensure scanning of exactly similar slices at each repetition and scan session at different scanners, residual positioning differences remain. By registering the maps, the errors can be minimized but not completely eliminated. The effect can be observed in the CoV maps, where higher deviations are present at boundaries between tissues. Grey matter regions are particularly more susceptible to such positioning errors since these grey matter areas are rather small compared to white matter.
Since the difference of relaxation times found in this study compared to literature is only observed in human tissue but not in phantom studies [Jia16b], its origin seems to be related to the complex tissue composition of the tissues in the brain, which affects T_2 mapping methods in different ways. This indicates the need for more elaborate signal models that could also generate more accurate measured relaxation times with MR Fingerprinting . For example, magnetization transfer [Hil17] and diffusion effects have been previously discussed, although another study [Hod18] has shown that the simulated impact of diffusion on T_2 is lower than the observed differences.
MR Fingerprinting may also provide proton density (PD) maps as a result of the pattern matching process. However, their reproducibility was not studied further, since the FISP-MRF method employed in this study is unable to provide an absolute measure for PD. Only a relative map can be derived, which scales linearly with PD but also with all other factors that influence the intensity of the raw signal (e.g., the coil sensitivity profiles). These PD maps vary considerably (e.g., depending on how the individual is placed in the coil) with the employed implementation of FISP-MRF. However, several calibration and computational methods exist to separate PD from coil sensitivity profiles (see eg. [Boj17] for a recent overview) that could be used for this implementation of FISP-MRF. Furthermore the PD maps can be normalized to a tissue with known PD to make measurements comparable."

T_1	Mean (%)	Median (%)	5% Percentile (%)	25% Percentile(%)	75% Percentile(%)	95% Percentile(%)
Solid Tissue	3.4	3.4	3.7	3.3	3.7	5.0
GM	2.6	2.6	3.5	2.6	2.8	4.1
Frontal GM	2.5	2.4	4.4	2.9	2.7	3.4
Temporal GM	1.8	1.9	2.7	2.0	2.0	2.5
Parietal GM	2.4	2.3	2.7	2.3	2.6	3.7
Occipital GM	2.4	2.5	3.8	2.9	2.3	3.5
Insula GM	2.9	3.1	4.0	3.1	3.2	3.7
Thalamus	3.0	3.1	3.4	3.2	3.2	3.6
Caudate Nucleus	2.8	2.8	3.5	3.0	2.9	3.0
Putamen	1.9	2.0	3.0	2.3	2.0	2.1
WM	2.0	2.0	2.5	2.0	2.1	3.8
Frontal WM	2.1	2.1	2.4	2.1	2.0	3.9
Temporal WM	2.0	1.9	2.5	2.0	2.1	4.1
Parietal WM	2.3	2.1	2.5	2.1	2.3	4.6
Occipital WM	2.6	2.1	2.2	2.2	3.0	7.0
Pallidum	2.5	2.7	3.8	2.8	2.5	3.0
Corpus Callosum	2.3	2.3	3.7	3.0	2.3	4.3
ROIs	4.1	4.2	4.2	4.0	4.7	6.0
CSF	5.5	5.9	7.5	5.1	7.2	6.1
T_2	Mean (%)	Median (%)	5% Percentile (%)	25% Percentile(%)	75% Percentile(%)	95% Percentile(%)
Solid Tissue	8.0	8.0	8.8	8.3	7.9	8.8
GM	7.3	6.9	7.9	7.2	7.2	10.7
Frontal GM	7.8	7.7	9.5	8.2	7.6	9.0
Temporal GM	5.3	5.4	6.5	5.7	5.2	5.6
Parietal GM	7.2	6.8	7.9	6.9	7.1	10.9
Occipital GM	5.5	5.3	6.0	5.4	5.5	9.2
Insula GM	7.4	7.3	8.4	7.8	7.2	9.1
Thalamus	7.2	6.9	8.0	7.0	7.2	8.2
Caudate Nucleus	9.0	9.0	9.6	9.3	8.7	9.1
Putamen	8.4	8.6	9.2	8.6	8.6	8.9
WM	7.7	7.7	9.1	8.2	7.4	7.3
Frontal WM	9.0	9.2	10.0	9.4	8.9	8.5
Temporal WM	6.2	6.3	7.0	6.5	6.0	6.1
Parietal WM	7.8	7.8	8.4	8.0	7.9	7.8
Occipital WM	6.3	6.2	7.2	6.4	6.2	7.4
Pallidum	8.9	9.0	10.3	9.8	8.3	8.5
Corpus Callosum	7.6	8.3	9.0	3.6	8.6	9.3
ROIs	8.5	8.6	9.2	8.7	8.5	8.9
CSF	18.2	18.7	16.0	16.3	20.9	20.3

Table 5.3: Inter-scanner confidence intervals (relative values (%)) for mean. median and percentile measurements of T_1 and T_2 in the segmented regions of interest.

T_1 **mean**	**Erlangen Prisma^{fit}**	**Erlangen Skyra A**	**Erlangen Skyra B**	**Erlangen Prisma**	**Erlangen Skyra C**	**Vienna Prisma**	**Vienna Prisma^{fit}**	**Cleveland Sykra A**	**Cleveland Sykra B**	**Essen Skyra**
Solid matter	2.4%	3.1%	2.4%	2.1%	2.7%	2.7%	2.0%	2.0%	2.1%	2.8%
GM	3.2%	2.7%	2.1%	1.6%	2.0%	2.3%	1.5%	1.8%	1.7%	2.3%
Frontal GM	1.5%	1.9%	1.7%	1.1%	1.6%	0.9%	1.2%	3.3%	2.8%	1.9%
Temporal GM	1.5%	1.9%	1.5%	1.5%	1.7%	1.6%	1.0%	1.1%	0.4%	2.5%
Parietal GM	2.2%	2.8%	1.9%	1.2%	1.3%	1.0%	1.1%	0.9%	1.2%	1.6%
Occipital GM	2.2%	2.1%	1.4%	1.6%	1.6%	1.9%	0.8%	1.0%	1.5%	1.9%
Insula GM	2.5%	2.8%	2.1%	1.4%	2.6%	2.1%	1.2%	0.8%	1.4%	3.2%
Thalamus	1.8%	2.2%	1.9%	1.9%	1.9%	1.9%	1.7%	3.3%	2.0%	2.0%
Caudate Nucleus	1.2%	2.7%	1.8%	1.4%	2.0%	1.8%	1.4%	2.3%	1.9%	2.1%
Putamen	1.0%	1.7%	1.8%	1.1%	1.8%	1.2%	1.4%	2.3%	1.5%	2.4%
WM	2.0%	2.1%	1.5%	1.1%	1.7%	2.0%	1.1%	1.3%	1.2%	2.0%
Frontal WM	1.5%	1.8%	1.4%	0.8%	1.4%	1.2%	1.1%	0.6%	0.7%	1.5%
Temporal WM	2.4%	1.8%	1.1%	0.8%	1.2%	2.4%	0.6%	1.3%	0.8%	1.7%
Parietal WM	2.8%	1.8%	1.6%	0.8%	1.2%	0.7%	0.9%	1.3%	1.2%	1.5%
Occipital WM	5.1%	2.5%	1.2%	0.9%	1.2%	4.3%	0.6%	1.8%	1.8%	1.3%
Pallidum	2.5%	1.8%	1.4%	1.2%	1.6%	1.5%	1.8%	1.8%	1.6%	3.5%
Corpus Callosum	2.3%	3.1%	1.5%	1.6%	1.9%	1.5%	1.2%	2.9%	1.6%	2.3%
ROIs	2.4%	3.8%	2.9%	2.6%	3.4%	3.3%	2.5%	2.3%	2.6%	3.3%
CSF	6.3%	8.3%	5.5%	5.5%	5.4%	5.8%	5.2%	6.5%	4.3%	7.6%
T_2 **mean**	**Erlangen Prisma^{fit}**	**Erlangen Skyra A**	**Erlangen Skyra B**	**Erlangen Prisma**	**Erlangen Skyra C**	**Vienna Prisma**	**Vienna Prisma^{fit}**	**Cleveland Sykra A**	**Cleveland Sykra B**	**Essen Skyra**
Solid matter	4.1 %	7.9%	4.0%	3.6%	5.1%	3.7%	3.1%	4.6%	4.4%	6.7%
GM	6.1%	10.1%	4.5%	3.7%	5.2%	4.5%	3.0%	4.1%	4.00%	6.7%
Frontal GM	2.9%	12.3%	4.4%	3.7%	5.6%	2.7%	4.1%	4.6%	3.2%	6.7%
Temporal GM	3.1%	6.4%	2.4%	2.8%	3.5%	3.4%	1.1%	4.0%	3.1%	5.4%
Parietal GM	7.4%	10.0%	4.5%	2.6%	3.6%	2.7%	2.0%	5.4%	1.4%	5.4%
Occipital GM	3.2%	7.6%	3.4%	2.3%	3.4%	7.1%	2.8%	3.1%	7.8%	4.0%
Insula GM	3.9%	10.4%	3.8%	3.5%	5.5%	3.0%	2.3%	5.5%	3.2%	5.5%
Thalamus	5.3%	7.1%	2.9%	3.6%	5.5%	4.4%	2.4%	2.7%	4.0%	7.9%
Caudate Nucleus	3.5%	8.8%	3.8%	3.8%	6.4%	3.2%	3.0%	6.2%	5.0%	7.0%
Putamen	4.2%	7.8%	2.6%	2.6%	4.8%	2.8%	1.8%	3.7%	4.4%	6.8%
WM	2.8%	6.5%	3.1%	2.8%	4.2%	2.7%	2.1%	4.4%	3.2%	6.4%
Frontal WM	2.2%	7.7%	3.1%	2.4%	4.3%	2.1%	1.9%	4.8%	2.6%	5.7%
Temporal WM	2.4%	4.6%	2.2%	1.6%	3.3%	2.3%	1.4%	4.7%	2.5%	6.2%
Parietal WM	2.5%	5.4%	2.9%	1.9%	3.5%	2.0%	1.9%	4.8%	1.7%	5.8%
Occipital WM	3.4%	5.0%	2.8%	1.8%	2.0%	2.9%	1.9%	4.7%	5.0%	5.3%
Pallidum	3.0%	7.2%	2.8%	3.4%	6.5%	4.6%	2.3%	4.5%	4.9%	9.1%
Corpus Callosum	3.9%	8.9%	3.3%	3.0%	4.8%	2.2%	1.8%	8.8%	4.7%	6.8%
ROIs	3.6%	7.6%	4.4%	3.9%	5.4%	3.7%	3.7%	4.7%	4.9%	7.0%
CSF	18.1%	36.2%	16.8%	13.6%	19.5%	13.6%	15.0%	15.5%	9.2%	27.1%

Table 5.4: Intra-scanner confidence intervals (relative values (%)) for mean values of T_1 and T_2 in the segmented regions of interest.

6. Discussion and Outlook

This work tried to commit to the developments in quantitative MRI and MRF in particular. The to date most popular MRF implementation FISP-MRF was examined on its susceptibility to magnetic field inhomogeneities and undersampling artifacts. Several claims of the original publication were investigated. First, the hypothesis that the very high undersampling factor in MRF produces artifacts in the time domain that do not affect the pattern match was investigated. It was found that the artifacts generated by different temporal variations of sampling patterns can have the same spectrum as the MR signal responses of tissues. In this case the pattern match can be severely affected. With the originally proposed temporal variation of the sampling pattern, high errors could be observed in the generated T_1 and T_2 maps. The reason for these errors could be linked to the undersampling artifacts. An optimal temporal variation of the undersampling pattern was designed which substantially decreased errors in the maps, even when applying advanced reconstruction techniques.

Second, the hypothesis that FISP-MRF is insensitive to inhomogeneneities of the static magnetic field B_0 and the oscillating magnetic field B_1^+ was examined. The technique exhibits a high sensitivity, to B_1^+ inhomogeneneities, which could be proven in phantom and in-vivo experiments. Strategies to counteract this dependency were implemented. With the use of FLASH signal segments or two pulses that are 90° phase shifted to each other, B_1^+-dependent information could be inserted into the signal. By taking the B_1^+ into account in the simulations and adding a B_1^+ dimension to the dictionary, the dependency could be resolved. Besides the T_1 and T_2 parameter maps, a B_1^+ map was generated by the pattern match. This solved the error arising from B_1^+ inhomogeneities in the T_1 or T_2 maps. The other strategy to deal with B_1^+ inhomogeneities investigated was the acquisition of a separate B_1^+ prescan. The information of this prescan was then used to select a sub-dictionary in B_1^+ dimension. This approach minimized potential errors of the pattern match by limiting the search space and also resolved the B_1^+ dependency of the relaxation parameters maps. On the downside, the B_1^+ map can have a T_1 or T_2 dependency that leads to potential B_1^+ misestimation. However, with the smoothness of the physical B_1^+ distributions and the rather low sensitivity of the employed B_1^+ mapping method to T_1 and T_2, this implementation constitutes a robust approach.

The FISP sequence in contrast to True-FISP is usually not considered to be particularly sensitive

to inhomogeneities of B_0. This assumption holds for conventional contrast-weighted MRI, where subtle contrast changes remain unnoticed. In FISP-MRF, it was found that a B_0 dependency exists, that can substantially alter T_1 and T_2 results. Although spin ensembles are not fully rephased before the onset of an RF pulse (as in TrueFlSP), the relative phase of the pulse to the spin ensemble influences the signal evolution. This leads to a periodic B_0 sensitivity of the signal evolutions and subsequently the T_1 and T_2 maps (depending on the employed TRs). Inserting an additional dephaser before the RF pulse, which dephases the spins, substantially decreases the B_0 dependency.

With the improvements made to the original FISP-MRF, this mature version was tested for its reproducibility. It used the improved spiral reordering, the prescan based B_1^+ correction and was B_0 insensitive due to an additionally employed 8π dephasing moment in each TR. Ten volunteers were scanned on ten different scanners at four different sites. Seven slices were scanned at the same anatomical positions. This allowed for the comparison of parameter values in different brain compartments. A high reproducibility of the T_1 and T_2 values could be shown. In solid brain tissues, parameter values differed less than $\pm 8\%$ across scanners.

Building on FISP-MRF as a basis, a completely novel MRF implementation termed Magnetic Resonance Field Fingerprinting (MRFF) was developed. The strategy of making parameter maps independent of homogeneous magnetic fields by integrating this information was employed here. Instead of trying to make the sequence insensitive to variations of the magnetic fields or measuring them using specialized techniques, the sequence was deliberately designed to be sensitive to B_0 and B_1^+. This was achieved by integrating both FLASH and TrueFISP into MRFF and reflecting this information in the dictionary. Higher undersampling factors and resolutions could be achieved compared to the original FISP-MRF implementation. By mapping B_0 and the intravoxel phase dispersion new clinical information was added. B_0 and intravoxel phase dispersion are caused by susceptibility differences of tissues which can reflect diseases.

This proof of concept shows the strengths and potential future directions of MRF. Instead of designing specific sequences that measure one parameter, multiple parameters can be measured simultaneously with MRF. This saves time and makes exams faster and on the other hand intrinsically resolves parameter interdependencies. First work has shown that i.a. diffusion, flow, chemical exchange or magnetization transfer can be simultaneously measured with specific MRF implementations.

This sounds promising but is subject to several limitations. Simulations can take a long time and computation time rises exponentially with every added dimension. Dictionaries can become very large when every included dimension covers a large range with high resolution. In turn,

pattern matching takes longer and might become more error prone, the bigger the search space is. Artificial intelligence can provide a solution to both the dictionary simulation and pattern match problem. Neural networks that process acquired signals and output parameter maps are much smaller than the corresponding dictionaries and much faster than the tedious comparison of an acquired signal with every dictionary entry. MRF also requires exact knowledge of the magnetic fields employed to manipulate the spins. The spiral trajectories that are employed in most MRF implementations are for example very sensitive to eddy currents and anisotropic delays of the system. These distort the trajectories that can result in hardly visible changes in individual images but causing substantial differences in the parameter maps. Like B_0 and B_1^+ imperfections, those trajectories could also be resolved by an MRF like approach. Slightly different trajectories could be used for the reconstruction and the "best" parameter maps automatically determined. For example, the homogeneity of parameter maps in certain structures could be used as a measure to evaluate what is the "best" reconstruction. Alternatively, simpler trajectories such as Cartesian could be used to make MRF results more stable across a variety of gradient systems without requiring thorough calibration.

Finally, a parameter that almost always affects MRI experiments is subject motion. Due to the long scan times in MRI in general, bulk motion, flow, pulsation or organ movement from breathing or the heartbeat must be accounted for. With the spiral MRF approach, highly time resolved images are acquired that can be used to track motion. Magnetic Resource Fingerprinting provides a multitude of possibilities for further technical and clinical research. Besides the mentioned issues the application of MRF in various body parts, all possessing their own challenges will be subject to further research. The method's success will to a high degree depend on the adoption of quantitative MRI into clinical routine. Promising directions are the characterization of tumors and differentiating other pathologies from tumors. Also, the response to treatment by applying e.g radiation therapy could be monitored with MRF.

BIBLIOGRAPHY

[Aar17] Chris I. Baker Aaron Trefler, Neda Sadeghi, Adam G. Thomas, Carlo Pierpaoli and Cibu Thomas. Impact of time-of-day on brain morphometric measures derived from T1 -weighted magnetic resonance imaging. 48(10):1119–1130, 2017.

[Ako93] S. Akoka, F. Franconi, F. Seguin, and A. Le Pape. Radiofrequency map of an NMR coil by imaging. *Magnetic Resonance Imaging*, 11(3):437–441, jan 1993.

[Ass17] Jakob Assländer, Steffen J. Glaser, and Jürgen Hennig. Pseudo Steady-State Free Precession for MR-Fingerprinting. *Magnetic Resonance in Medicine*, 77(3):1151–1161, 2017.

[Ass18] Jakob Assländer, Martijn A. Cloos, Florian Knoll, Daniel K. Sodickson, Jürgen Hennig, and Riccardo Lattanzi. Low rank alternating direction method of multipliers reconstruction for MR fingerprinting. *Magnetic Resonance in Medicine*, 79(1):83–96, mar 2018.

[Bad17] C Badve, A Yu, S Dastmalchian, M Rogers, D Ma, X Y Jiang, X S Margevicius, S Pahwa, Z Lu, M Schluchter, J Sunshine, M Griswold, A Sloan, and V Gulani. MR Fingerprinting of Adult Brain Tumors: Initial Experience. 2017.

[BE15] Noam Ben-Eliezer, Daniel K Sodickson, and Tobias Kai Block. Rapid and Accurate T2 Mapping from Multi Spin Echo Data Using Bloch-Simulation-Based Reconstruction, feb 2015.

[Ber04] X. J. Bernstein, M. A., King, K. F. & Zhou. *Handbook Of MRI Pulse Sequences*. Elsevier Academic Press, 2004.

[Bip18] Bhairav Bipin Mehta, Simone Coppo, Debra Frances McGivney, Jesse Ian Hamilton, Yong Chen, Yun Jiang, Dan Ma, Nicole Seiberlich, Vikas Gulani, and Mark Alan Griswold. Magnetic resonance fingerprinting: a technical review. *Magnetic Resonance in Medicine*, (August 2017):25–46, 2018.

[Blo46] F. Bloch. Nuclear induction. *Phys. Rev.*, 70:460–474, Oct 1946.

[Bo 16] Bo Bo Zhao, Justin P Haldar, Kawin Setsompop, and Lawrence L Wald. Optimal experiment design for magnetic resonance fingerprinting. *Conference proceedings : ... Annual International Conference of the IEEE Engineering in Medicine and Biology Society. IEEE Engineering in Medicine and Biology Society. Annual Conference*, 2016:453–456, 2016.

[Boj17] Jorge Zavala Bojorquez, Stéphanie Bricq, Clement Acquitter, François Brunotte, Paul M. Walker, and Alain Lalande. What are normal relaxation times of tissues at 3 T? *Magnetic Resonance Imaging*, 35:69–80, 2017.

[Boy11] Stephen Boyd, Neal Parikh, Eric Chu, Borja Peleato, Jonathan Eckstein, et al. Distributed optimization and statistical learning via the alternating direction method of multipliers. *Foundations and Trends® in Machine learning*, 3(1):1–122, 2011.

[Bro14] Robert Brown, Yu-Chung Cheng, Mark Haacke, Michael R. Thompson, and Ramesh Venkatesan. *Magnetic Resonance Imaging: Physical Principles and Sequence Design: Second Edition*. 01 2014.

[Buo16] Guido Buonincontri and Stephen J. Sawiak. MR fingerprinting with simultaneous B1 estimation. *Magnetic Resonance in Medicine*, 76(4):1127–1135, 2016.

[Buo17] Guido Buonincontri, Rolf F. Schulte, Mirco Cosottini, and Michela Tosetti. Spiral MR fingerprinting at 7 T with simultaneous B1 estimation. *Magnetic Resonance Imaging*, 41(0):1–6, apr 2017.

[Cam10] Peter G Campbell, Pascal Jabbour, Sanjay Yadla, and Issam A Awad. Emerging clinical imaging techniques for cerebral cavernous malformations: a systematic review. *Neurosurgical focus*, 29(3):E6–E6, sep 2010.

[Cao18] X Cao, C Liao, Q Li, H Ye, H He, and J Zhong. Fast 3D MR fingerprinting with spiral projection acquisition for whole brain quantification imaging. page 1017, 2018.

[Cau15] Stephen F. Cauley, Kawin Setsompop, Dan Ma, Yun Jiang, Huihui Ye, Elfar Adalsteinsson, Mark A. Griswold, and Lawrence L. Wald. Fast group matching for MR fingerprinting reconstruction. *Magnetic Resonance in Medicine*, 74(2):523–528, aug 2015.

[Che16] Yong Chen, Yun Jiang, Shivani Pahwa, Dan Ma, Lan Lu, Michael D. Twieg, Katherine L. Wright, Nicole Seiberlich, Mark A. Griswold, and Vikas Gulani.

MR Fingerprinting for Rapid Quantitative Abdominal Imaging. *Radiology*, 279(1):278–286, apr 2016.

[Che19] Yong Chen, Ananya Panda, Shivani Pahwa, Jesse I. Hamilton, Sara Dastmalchian, Debra F. McGivney, Dan Ma, Joshua Batesole, Nicole Seiberlich, Mark A. Griswold, Donna Plecha, and Vikas Gulani. Three-dimensional mr fingerprinting for quantitative breast imaging. *Radiology*, 290(1):33–40, 2019. PMID: 30375925.

[Chi17] Su Chin Chiu, Te Ming Lin, Jyh Miin Lin, Hsiao Wen Chung, Cheng Wen Ko, Martin Büchert, and Michael Bock. Effects of RF pulse profile and intra-voxel phase dispersion on MR fingerprinting with balanced SSFP readout. *Magnetic Resonance Imaging*, 41:80–86, sep 2017.

[Chr74] Kenner A Christensen, David M Grant, Edward M Schulman, and Cheves Walling. Optimal determination of relaxation times of fourier transform nuclear magnetic resonance. determination of spin-lattice relaxation times in chemically polarized species. *The Journal of Physical Chemistry*, 78(19):1971–1977, 1974.

[Chu10] Sohae Chung, Daniel Kim, Elodie Breton, and Leon Axel. Rapid B1+mapping using a preconditioning RF pulse with turboFLASH readout. *Magnetic Resonance in Medicine*, 64(2):439–446, 2010.

[Cli17] Christopher C. Cline, Xiao Chen, Boris Mailhe, Qiu Wang, Josef Pfeuffer, Mathias Nittka, Mark A. Griswold, Peter Speier, and Mariappan S. Nadar. AIR-MRF: Accelerated iterative reconstruction for magnetic resonance fingerprinting. *Magnetic Resonance Imaging*, 41:29–40, 2017.

[Clo16] Martijn A. Cloos, Florian Knoll, Tiejun Zhao, Kai T. Block, Mary Bruno, Graham C. Wiggins, and Daniel K. Sodickson. Multiparametric imaging with heterogeneous radiofrequency fields. *Nature Communications*, 7:12445, aug 2016.

[Con87] B Condon, J Patterson, Alistair Jenkins, D Wyper, D Hadley, Robert Grant, J Rowan, and Graham Teasdale. MR Relaxation Times of Cerebrospinal Fluid. *Journal of computer assisted tomography*, 11:203–207, 1987.

[Cru18] G. Cruz, O. Jaubert, S. Malik, T. Schneider, R. Botnar, and C. Prieto. Rigid motion corrected low rank magnetic resonance fingerprinting. In *Proceedings of the 26th Annual Meeting of ISMRM*, page 1173, 2018.

[CW16] Adrienne E. Campbell-Washburn, Hui Xue, Robert J. Lederman, Anthony Z. Faranesh, and Michael S. Hansen. Real-time distortion correction of spiral and echo planar images using the gradient system impulse response function. *Magnetic Resonance in Medicine*, 75(6):2278–2285, 2016.

[Dem05a] Wolfgang Demtröder. *Experimentalphysik 4: Kern-, Teilchen- und Astrophysik; 2nd ed.* Springer, Berlin, 2005.

[Dem05b] W. Demtröder. *Experimentalphysik 3: Atome, Moleküle und Festkörper*. Experimentalphysik / Wolfgang Demtröder. Springer, 2005.

[Deo03] Sean CL Deoni, Brian K Rutt, and Terry M Peters. Rapid combined t1 and t2 mapping using gradient recalled acquisition in the steady state. *Magnetic Resonance in Medicine: An Official Journal of the International Society for Magnetic Resonance in Medicine*, 49(3):515–526, 2003.

[Dyd00] Boesiger P. Dydak, U., Pruessmann K. P., Weiger M. The Spatial Response Function in SENSE-SI. In *Proceedings of the 8th Annual Meeting of ISMRM*, page 1848, 2000.

[Fan17] Zhenghan Fang, Yong Chen, Weili Lin, and Dinggang Shen. Quantification of relaxation times in MR Fingerprinting using deep learning. In *Proceedings of the 25th Annual Meeting of ISMRM Annual Meeting of ISMRM*, volume 25, apr 2017.

[Fei] Thorsten Feiweier. Method for determining the b1 field strength in mr measurements. Patent No. US 75064546 B2 granted, Patent No. DE10354941B4 granted.

[Fes03] J A Fessler and B P Sutton. Nonuniform fast Fourier transforms using min-max interpolation. *IEEE Transactions on Signal Processing*, 51(2):560–574, feb 2003.

[Fla18] Sebastian Flassbeck, Simon Schmidt, Peter Bachert, Mark E. Ladd, and Sebastian Schmitter. Flow MR fingerprinting. *Magnetic Resonance in Medicine*, (June 2018):2536–2550, 2018.

[Gao15] Ying Gao, Yong Chen, Dan Ma, Yun Jiang, Kelsey A. Herrmann, Jason A. Vincent, Katherine M. Dell, Mitchell L. Drumm, Susann M. Brady-Kalnay, Mark A. Griswold, Chris A. Flask, and Lan Lu. Preclinical MR fingerprinting (MRF) at 7 T: Effective quantitative imaging for rodent disease models. *NMR in Biomedicine*, 28(3):384–394, mar 2015.

[Gri02] Mark A. Griswold, Peter M. Jakob, Robin M. Heidemann, Mathias Nittka, Vladimir Jellus, Jianmin Wang, Berthold Kiefer, and Axel Haase. Generalized autocalibrating partially parallel acquisitions (grappa). *Magnetic Resonance in Medicine*, 47(6):1202–1210, 2002.

[GS15] Matthew Grech-Sollars, Patrick W. Hales, Keiko Miyazaki, Felix Raschke, Daniel Rodriguez, Martin Wilson, Simrandip K. Gill, Tina Banks, Dawn E. Saunders, Jonathan D. Clayden, Matt N. Gwilliam, Thomas R. Barrick, Paul S. Morgan, Nigel P. Davies, James Rossiter, Dorothee P. Auer, Richard Grundy, Martin O. Leach, Franklyn A. Howe, Andrew C. Peet, and Chris A. Clark. Multi-centre reproducibility of diffusion MRI parameters for clinical sequences in the brain. *NMR in Biomedicine*, 28(4):468–485, apr 2015.

[Haa04] E Mark Haacke, Yingbiao Xu, Yu Chung Norman Cheng, and Jürgen R Reichenbach. Susceptibility Weighted Imaging (SWI). *MRM*, 52:612–618, 2004.

[Hal07] JP Haldar, J Anderson, and SW Sun. Maximum likelihood estimation of t1 relaxation parameters using varpro. In *Proceedings of the 15th Annual Meeting of ISMRM, Berlin, Germany*, page 41, 2007.

[Ham15a] Jesse I Hamilton, Mark A Griswold, and Nicole Seiberlich. MR Fingerprinting with chemical exchange (MRF-X) to quantify subvoxel T1 and extracellular volume fraction. *Journal of Cardiovascular Magnetic Resonance*, 17(Suppl 1):W35, 2015.

[Ham15b] Sieberlich N. Hamilton JI, Wright KL, Jiang Y, Hernandez-Garcia L, Ma D, Griswold M. Pulse sequence optimization for improved MRF scan efficiency. In *Proceedings of the 23rd Annual Meeting of ISMRM*, page 3386, 2015.

[Ham16] Jesse I Hamilton, Yun Jiang, Dan Ma, Bhairav B Mehta, Wei-Ching Lo, Yong Chen, Mark A Griswold, and Nicole Seiberlich. Cardiac MR fingerprinting for T1 and T2 mapping in four heartbeats. *Journal of Cardiovascular Magnetic Resonance*, 18(Suppl 1):W1, 2016.

[Ham17] Jesse I. Hamilton, Yun Jiang, Yong Chen, Dan Ma, Wei Ching Lo, Mark Griswold, and Nicole Seiberlich. MR fingerprinting for rapid quantification of myocardial T1, T2, and proton spin density. *Magnetic Resonance in Medicine*, 77(4):1446–1458, apr 2017.

[Han17] D. Han, T. Hong, and D.-H. Kim. Development of Magnetic Resonance Fingerprinting (MRF) Combined with FISP and Multi-Echo SPGR Acquisition for Proton Density, T1, T2, T2* and Field Mapping. In *Proceedings of the 25th Annual Meeting of ISMRM Annual Meeting of ISMRM*, page 3711, 2017.

[HC17] Christian R Hamilton-Craig, Mark W Strudwick, and Graham J Galloway. T1 Mapping for Myocardial Fibrosis by Cardiac Magnetic Resonance Relaxometry—A Comprehensive Technical Review. *Frontiers in Cardiovascular Medicine*, 3:49, 2017.

[He13] Kaiming He, Jian Sun, and Xiaoou Tang. Guided image filtering. *IEEE Transactions on Pattern Analysis and Machine Intelligence*, 35(6):1397–1409, jun 2013.

[Hil17] Tom Hilbert, Tobias Kober, Tiejun Zhao, Tobias Kai Block, Zidan Yu, Jean-Philippe Thiran, Gunnar Krueger, Daniel K Sodickson, and Martijn Cloos. Mitigating the effect of magnetization transfer in magnetic resonance fingerprinting. In *Proc. Intl. Soc. Mag. Res. Med.*, page 0074, 2017.

[Hod18] S. Hodono, Y. Jiang, G. Körzdörfer, N. Nallapareddy, V. Gulani, and M. Griswold. Matching Error Evaluation in Magnetic Resonance Fingerprinting with a Fast Imaging with Steady Precession sequence using Bloch Equation Simulations with a Diffusion Propagator. In *Proceedings of the 26th Annual Meeting of ISMRM*, page 2891, 2018.

[Hop17] Elisabeth Hoppe, Gregor Körzdörfer, Tobias Würfl, Jens Wetzl, Felix Lugauer, Josef Pfeuffer, and Andreas Maier. Deep learning for magnetic resonance fingerprinting: A new approach for predicting quantitative parameter values from time series. In *Studies in Health Technology and Informatics*, volume 243, pages 202–206, 2017.

[IE92] Bolinger L Insko EK. B1 mapping. In *Proceedings of the 11th AnnualMeeting of SMRM*, page 4302, 1992.

[Jia] Yun Jiang, Dan Ma, Renate Jerecic, Jeffrey Duerk, Nicole Seiberlich, Vikas Gulani, and Mark A Griswold. MR fingerprinting using the quick echo splitting NMR imaging technique. *Magnetic Resonance in Medicine*, 77(3):979–988.

[Jia15] Yun Jiang, Dan Ma, Nicole Seiberlich, Vikas Gulani, and Mark A. Griswold. MR fingerprinting using fast imaging with steady state precession (FISP) with spiral readout. *Magnetic Resonance in Medicine*, 74(6):1621–1631, dec 2015.

[Jia16a] Yun Jiang, Jesse Hamilton, Katherine L Wright, Dan Ma, Nicole Seiberlich, Vikas Gulani, and Mark A Griswold. Simultaneous Quantification of T1, T2 and Diffusion with Diffusion-Weighted Drive-Equilibrium Prepared Magnetic Resonance Fingerprinting. In *Proceedings of the 24th Annual Meeting of ISMRM, Singapore*, page 4296, 2016.

[Jia16b] Yun Jiang, Dan Ma, Kathryn E. Keenan, Karl F. Stupic, Vikas Gulani, and Mark A. Griswold. Repeatability of magnetic resonance fingerprinting T ₁ and T ₂ estimates assessed using the ISMRM/NIST MRI system phantom. *Magnetic Resonance in Medicine*, oct 2016.

[Jia17] Yun Jiang, Dan Ma, Himanshu Bhat, Huihui Ye, Stephen F. Cauley, Lawrence L. Wald, Kawin Setsompop, and Mark A. Griswold. Use of pattern recognition for unaliasing simultaneously acquired slices in simultaneous multislice mr fingerprinting. *Magnetic Resonance in Medicine*, 78(5):1870–1876, 2017.

[Jov13] Jorge Jovicich, Moira Marizzoni, Roser Sala-Llonch, Beatriz Bosch, David Bartrés-Faz, Jennifer Arnold, Jens Benninghoff, Jens Wiltfang, Luca Roccatagliata, Flavio Nobili, Tilman Hensch, Anja Tränkner, Peter Schönknecht, Melanie Leroy, Renaud Lopes, Régis Bordet, Valérie Chanoine, Jean Philippe Ranjeva, Mira Didic, Hélène Gros-Dagnac, Pierre Payoux, Giada Zoccatelli, Franco Alessandrini, Alberto Beltramello, Núria Bargalló, Olivier Blin, and Giovanni B. Frisoni. Brain morphometry reproducibility in multi-center 3T MRI studies: A comparison of cross-sectional and longitudinal segmentations. *NeuroImage*, 83:472–484, 2013.

[Kör16] G. Körzdörfer, T. Feiweier, Y. Jiang, and M. Nittka. B1-Sensitive Encoding for Magnetic Resonance Fingerprinting. In *Proceedings of the 24th Annual Meeting of ISMRM*, page 3191, Singapore,Singapore, 2016.

[Kör17] G. Körzdörfer, D. Ma, J. Pfeuffer, B. Hensel, M. Griswold, and M. Nittka. Robust B1+ sensitive FISP Magnetic Resonance Fingerprinting in Brain and Abdomen. In *ESMRMB Congress 2017 – 34th Annual Scientific Meeting*, page 483, Barcelona,Spain, 2017.

[Kör18a] G. Körzdörfer, B. Guzek, Y. Jiang, J. Pfeuffer, B. Hensel, P. Speier, and M. Nittka. Description of the off-resonance dependency in slice-selective FISP MRF. In *Proceedings of the 26th Annual Meeting of ISMRM*, page 8085, 2018.

[Kör18b] G. Körzdörfer, P. Speier, S. Schröter, M. Schramm, J. Pfeuffer, B. Hensel, and M. Nittka. Evaluating the influence of motion on FISP-MRF. In *Proceedings of the 26th Annual Meeting of ISMRM*, page 4085, 2018.

[Kör18c] Gregor Körzdörfer, Yun Jiang, Peter Speier, Jianing Pang, Dan Ma, Josef Pfeuffer, Bernhard Hensel, Vikas Gulani, Mark Griswold, and Mathias Nittka. Magnetic resonance field fingerprinting, 2018.

[Kör19a] Gregor Körzdörfer, Rainer Kirsch, Kecheng Liu, Josef Pfeuffer, Bernhard Hensel, Yun Jiang, Dan Ma, Marcel Gratz, Peter Bäer, Wolfgang Bogner, Elisabeth Springer, Pedro Lima Cardoso, Lale Umutlu, Siegfried Trattnig, Mark Griswold, Vikas Gulani, and Mathias Nittka. Reproducibility and repeatability of Magnetic Resonance Fingerprinting relaxometry in the human brain. *Radiology*, 2019.

[Kör19b] Gregor Körzdörfer, Josef Pfeuffer, Thomas Kluge, Matthias Gebhardt, Bernhard Hensel, Craig H Meyer, and Mathias Nittka. Effect of spiral undersampling patterns on FISP MRF parameter maps. *Magnetic Resonance Imaging*, page #pagerange#, 2019.

[Lau73] P. C. Lauterbur. Image Formation by Induced Local Interactions: Examples Employing Nuclear Magnetic Resonance. *Nature*, 242:190–191, March 1973.

[Lia17] Congyu Liao, Berkin Bilgic, Mary Kate Manhard, Bo Zhao, Xiaozhi Cao, Jianhui Zhong, Lawrence L Wald, and Kawin Setsompop. 3D MR fingerprinting with accelerated stack-of-spirals and hybrid sliding-window and GRAPPA reconstruction. *NeuroImage*, 162:13–22, nov 2017.

[Lia18] Congyu Liao, Kang Wang, Xiaozhi Cao, Yueping Li, Dengchang Wu, Huihui Ye, Qiuping Ding, Hongjian He, and Jianhui Zhong. Detection of Lesions in Mesial Temporal Lobe Epilepsy by Using MR Fingerprinting. *Radiology*, 288(3):172131, sep 2018.

[Liu16] Li Liu, Bo Yin, Dao Ying Geng, Yi Ping Lu, and Wei Jun Peng. Changes of T2 relaxation time from neoadjuvant chemotherapy in breast cancer lesions. *Iranian Journal of Radiology*, 13(3):e24014, jul 2016.

[Loo70] D. C. Look and D. R. Locker. Time saving in measurement of nmr and epr relaxation times. *Review of Scientific Instruments*, 41(2):250–251, 1970.

[Ma13] Dan Ma, Vikas Gulani, Nicole Seiberlich, Kecheng Liu, Jeffrey L Sunshine, Jeffrey L Duerk, and Mark A Griswold. Magnetic resonance fingerprinting. *Nature*, 495(7440):187–92, mar 2013.

[Ma16] Dan Ma, Eric Y. Pierre, Yun Jiang, Mark D. Schluchter, Kawin Setsompop, Vikas Gulani, and Mark A. Griswold. Music-based magnetic resonance fingerprinting to improve patient comfort during MRI examinations. *Magnetic Resonance in Medicine*, 75(6):2303–2314, jun 2016.

[Ma17a] Dan Ma, Simone Coppo, Yong Chen, Debra F. McGivney, Yun Jiang, Shivani Pahwa, Vikas Gulani, and Mark A. Griswold. Slice profile and B1corrections in 2D magnetic resonance fingerprinting. *Magnetic Resonance in Medicine*, 78(5):1781–1789, jan 2017.

[Ma17b] Dan Ma, Yun Jiang, Yong Chen, Debra McGivney, Bhairav Mehta, Vikas Gulani, and Mark Griswold. Fast 3D magnetic resonance fingerprinting for a whole-brain coverage. *Magnetic Resonance in Medicine*, 2197:2190–2197, 2017.

[Mac09] A L MacKay, I M Vavasour, A Rauscher, S H Kolind, B Mädler, G R W Moore, A L Traboulsee, D K B Li, and C Laule. MR Relaxation in Multiple Sclerosis. *Neuroimaging Clinics of North America*, 19(1):1–26, 2009.

[Mac11] Tan Sh Machin, D, Campbell, MJ, Tan Sb. *Sample Size Tables for Clinical Studies, Third Edition*. Wiley-Blackwell, Chichester, England, 2011.

[Man73] P Mansfield and P K Grannell. Nmr “diffraction“ in solids? *Journal of Physics C: Solid State Physics*, 6(22):L422–L426, nov 1973.

[Mar12] Hai Ling Margaret Cheng, Nikola Stikov, Nilesh R. Ghugre, and Graham A. Wright. Practical medical applications of quantitative MR relaxometry, oct 2012.

[McG14] Debra F. McGivney, Eric Pierre, Dan Ma, Yun Jiang, Haris Saybasili, Vikas Gulani, and Mark A. Griswold. SVD compression for magnetic resonance fingerprinting in the time domain. *IEEE Transactions on Medical Imaging*, 33(12):2311–2322, dec 2014.

[Mey11] Craig H. Meyer, Li Zhao, Miki Lustig, and Et al. Dual-density and parallel spiral ASL for motion artifact reduction (PDF Download Available). In *Proceedings of the 19th Annual Meeting of ISMRM*, page 3986, 2011.

[Mor08] Glen R. Morrell. A phase-sensitive method of flip angle mapping. *Magnetic Resonance in Medicine*, 60(4):889–894, 2008.

[Muj09] Marius Muja. FAST APPROXIMATE NEAREST NEIGHBORS WITH AUTOMATIC ALGORITHM CONFIGURATION. In *Proceedings of the Fourth International Conference on Computer Vision Theory and Applications*, pages 331–340, 2009.

[Muj14] Marius Muja and David G Lowe. Scalable nearest neighbor algorithms for high dimensional data. *IEEE Transactions on Pattern Analysis and Machine Intelligence*, 36(11):2227–2240, 2014.

[Mul15] Robert V Mulkern, Mukund Balasubramanian, and Dimitrios Mitsouras. On the lorentzian versus Gaussian character of time-domain spin-echo signals from the brain as sampled by means of gradient-echoes: Implications for quantitative transverse relaxation studies. *Magnetic Resonance in Medicine*, 74(1):51–62, jul 2015.

[Nol92] Douglas C Noll, John M Pauly, Craig H Meyer, Dwight G Nishimura, and Albert Macovskj. Deblurring for non-2D fourier transform magnetic resonance imaging. *Magnetic Resonance in Medicine*, 25(2):319–333, 1992.

[Ost17] Jason Ostenson, Ryan K. Robison, Nicholas R. Zwart, and E. Brian Welch. Multi-frequency interpolation in spiral magnetic resonance fingerprinting for correction of off-resonance blurring. *Magnetic Resonance Imaging*, 41:63–72, sep 2017.

[Ots97] Kimio Otsuka and Tatsuo Togawa. Hippocratic thermography. *Physiological Measurement*, 18(3):227–232, aug 1997.

[Our] Cohen Ouri, Zhu Bo, and Rosen Matthew S. MR fingerprinting Deep RecOnstruction NEtwork (DRONE). *Magnetic Resonance in Medicine*, 80(3):885–894.

[Pan18] Shen Pan, Xiao Qi Wang, and Qi Yong Guo. Quantitative assessment of hepatic fibrosis in chronic hepatitis B and C: T1 mapping on Gd-EOB-DTPA-enhanced liver magnetic resonance imaging clinical trials study. *World Journal of Gastroenterology*, 24(18):2024–2035, may 2018.

[Pie10] Carlo Pierpaoli. Quantitative Brain MRI. *Topics in Magnetic Resonance Imaging*, 21(2):3–4, 2010.

[Pie16] Eric Y. Pierre, Dan Ma, Yong Chen, Chaitra Badve, and Mark A. Griswold. Multiscale reconstruction for MR fingerprinting. *Magnetic Resonance in Medicine*, 75(6):2481–2492, jun 2016.

[Pru99] Klaas P. Pruessmann, Markus Weiger, Markus B. Scheidegger, and Peter Boesiger. Sense: Sensitivity encoding for fast mri. *Magnetic Resonance in Medicine*, 42(5):952–962, 1999.

[Pur46] E. M. Purcell, H. C. Torrey, and R. V. Pound. Resonance absorption by nuclear magnetic moments in a solid. *Phys. Rev.*, 69:37–38, Jan 1946.

[Rab38] I. I. Rabi, J. R. Zacharias, S. Millman, and P. Kusch. A new method of measuring nuclear magnetic moment. *Phys. Rev.*, 53:318–318, Feb 1938.

[Rec98] M P Recht and D Resnick. Magnetic resonance imaging of articular cartilage: an overview. *Top.Magn Reson.Imaging*, 9(0899-3459):328–336, dec 1998.

[RÖN96] W. C. RÖNTGEN. On a new kind of rays. *Science*, 3(59):227–231, 1896.

[Sac10] Laura I. Sacolick, Florian Wiesinger, Ileana Hancu, and Mika W. Vogel. B1 mapping by bloch-siegert shift. *Magnetic Resonance in Medicine*, 63(5):1315–1322, 2010.

[Sli79] Charles Slichter. Principles of magnetic resonance / c. p. slichter. *SERBIULA (sistema Librum 2.0)*, 56, 01 1979.

[Som17] K. Sommer, T. Amthor, M. Doneva, P. Koken, J. Meineke, and P. Börnert. Towards predicting the encoding capability of mr fingerprinting sequences. *Magnetic Resonance Imaging*, 41:7 – 14, 2017.

[Sto88] R Stollberger, P Wach, G McKinnon, E Justich, and F. Ebner. Rf-field mapping in vivo. In *Proceedings of the 7th Annual Meeting of SMRM*, page 106, 1988.

[Su17] Pan Su, Deng Mao, Peiying Liu, Yang Li, Marco C. Pinho, Babu G. Welch, and Hanzhang Lu. Multiparametric estimation of brain hemodynamics with mr fingerprinting asl. *Magnetic Resonance in Medicine*, 78(5):1812–1823, 2017.

[Sym16] Rolf Symons, Justin Z Morris, Colin O Wu, Amir Pourmorteza, Mark A Ahlman, João A C Lima, Marcus Y Chen, Marissa Mallek, Veit Sandfort, and David A Bluemke. Coronary CT Angiography: Variability of CT Scanners and Readers in Measurement of Plaque Volume. *Radiology*, 281(3):737–748, 2016.

[Tan09] Hao Tan and Craig H. Meyer. Estimation of k-space trajectories in spiral MRI. *Magnetic Resonance in Medicine*, 61(6):1396–1404, jun 2009.

[Tsa06] Jeffrey Tsao, Peter Boesiger, and Klaas P. Pruessmann. Lattice permutation for reducing motion artifacts in radial and spiral dynamic imaging. *Magnetic Resonance in Medicine*, 55(1):116–125, jan 2006.

[Van13] Signe J. Vannesjo, Maximilan Haeberlin, Lars Kasper, Matteo Pavan, Bertram J. Wilm, Christoph Barmet, and Klaas P. Pruessmann. Gradient system characterization by impulse response measurements with a dynamic field camera. *Magnetic Resonance in Medicine*, 69(2):583–593, 2013.

[Van16] S. Johanna Vannesjo, Nadine N. Graedel, Lars Kasper, Simon Gross, Julia Busch, Maximilian Haeberlin, Christoph Barmet, and Klaas P. Pruessmann. Image reconstruction using a gradient impulse response model for trajectory prediction. *Magnetic Resonance in Medicine*, 76(1):45–58, 2016.

[Vau01] J. T. Vaughan, M. Garwood, C. M. Collins, W. Liu, L. Delabarre, G. Adriany, P. Andersen, H. Merkle, R. Goebel, M. B. Smith, and K. Ugurbil. 7T vs. 4T: RF power, homogeneity, and signal-to-noise comparison in head images. *Magnetic Resonance in Medicine*, 46(1):24–30, jul 2001.

[Vla03] M.T. Vlaardingerbroek, A. Luiten, J.A. Boer, and F. Knoet. *Magnetic Resonance Imaging: Theory and Practice*. Physics and astronomy online library. Springer, 2003.

[Voi10] Tobias Voigt, Kay Nehrke, Olaf Doessel, and Ulrich Katscher. T1 corrected B1 mapping using multi-TR gradient echo sequences. *Magnetic Resonance in Medicine*, 64(3):725–733, 2010.

[Wan99] Janaka P. Wansapura, Scott K. Holland, R. Scott Dunn, and William S. Ball. NMR relaxation times in the human brain at 3.0 Tesla. *Journal of Magnetic Resonance Imaging*, 9(4):531–538, apr 1999.

[Wei15] Matthias Weigel. Extended phase graphs: Dephasing, RF pulses, and echoes - Pure and simple, feb 2015.

[Wel08] Goetz H. Welsch, Tallal C. Mamisch, Stephan E. Domayer, Ronald Dorotka, Florian Kutscha-Lissberg, Stefan Marlovits, Lawrence M. White, and Siegfried Trattnig. Cartilage T2 Assessment at 3-T MR Imaging: In Vivo Differentiation

of Normal Hyaline Cartilage from Reparative Tissue after Two Cartilage Repair Procedures—Initial Experience. *Radiology*, 247(1):154–161, apr 2008.

[Yar07] Vasily L. Yarnykh. Actual flip-angle imaging in the pulsed steady state: A method for rapid three-dimensional mapping of the transmitted radiofrequency field. *Magnetic Resonance in Medicine*, 57(1):192–200, 2007.

[Ye18] H. Ye, Q. Li, X. Cao, Q. Ding, H. He, H. Liu, and J. Zhong. MR Fingerprinting (MRF) incorporating simultaneous detection of RF transmit field and B0 inhomogeneity. In *Proceedings of the 26th Annual Meeting of ISMRM*, page 0172, 2018.

[Yu17a] Alice C. Yu, Chaitra Badve, Lee E. Ponsky, Shivani Pahwa, Sara Dastmalchian, Matthew Rogers, Yun Jiang, Seunghee Margevicius, Mark Schluchter, William Tabayoyong, Robert Abouassaly, Debra McGivney, Mark A. Griswold, and Vikas Gulani. Development of a combined mr fingerprinting and diffusion examination for prostate cancer. *Radiology*, 283(3):729–738, 2017. PMID: 28187264.

[Yu17b] Z. Yu, T. Zhao, J. Assländer, R. Lattanzi, D. Sodickson, and M. Cloos. Exploring the Sensitivity of Magnetic Resonance Fingerprinting to Different Types of Motion and Possible Correction Mechanisms. In *Proceedings of the 25th Annual Meeting of ISMRM Annual Meeting of ISMRM*, page 3938, 2017.

[Zha15] Bo Zhao, Wenmiao Lu, T Kevin Hitchens, Fan Lam, Chien Ho, and Zhi Pei Liang. Accelerated MR parameter mapping with low-rank and sparsity constraints. *Magnetic Resonance in Medicine*, 74(2):489–498, aug 2015.

[Zha16] Bo Zhao, Kawin Setsompop, Huihui Ye, Stephen F. Cauley, and Lawrence L. Wald. Maximum Likelihood Reconstruction for Magnetic Resonance Fingerprinting. *IEEE Transactions on Medical Imaging*, 35(8):1812–1823, aug 2016.

[Zur91] Y. Zur, M. L. Wood, and L. J. Neuringer. Spoiling of transverse magnetization in steady-state sequences. *Magnetic Resonance in Medicine*, 21(2):251–263, oct 1991.

Own Publications

Journal Publications

- **Gregor Körzdörfer**, Yun Jiang, Peter Speier, Jianing Pang, Dan Ma, Josef Pfeuffer, Bernhard Hensel, Vikas Gulani, Mark Griswold, and Mathias Nittka. Magnetic resonance field fingerprinting. *Magnetic Resonance in Medicine*, 2018

- **Gregor Körzdörfer**, Josef Pfeuffer, Thomas Kluge, Matthias Gebhardt, Bernhard Hensel, Craig H Meyer, and Mathias Nittka. Effect of spiral undersampling patterns on FISP MRF parameter maps. *Magnetic Resonance Imaging*, 2019

- **Gregor Körzdörfer**, Rainer Kirsch, Kecheng Liu, Josef Pfeuffer, Bernhard Hensel, Yun Jiang, Dan Ma, Marcel Gratz, Peter Bär, Wolfgang Bogner, Elisabeth Springer, Pedro Lima Cardoso, Lale Umutlu, Siegfried Trattnig, Mark Griswold, Vikas Gulani, and Mathias Nittka. Reproducibility and Repeatability of MR Fingerprinting Relaxometry in the Human Brain. *Radiology*, 292(2):429–437, 2019. PMID: 31210615

- Shinji Naganawa, Toshiki Nakane, Hisashi Kawai, Toshiaki Taoka, Hirokazu Kawaguchi, Katsuya Maruyama, Katsutoshi Murata, **Gregor Körzdörfer**, Josef Pfeuffer, Mathias Nittka, and Michihiko Sone. Detection of IV-gadolinium Leakage from the Cortical Veins into the CSF Using MR Fingerprinting. *Magnetic Resonance in Medical Sciences*, advpub, 2019

- Yutaka Kato, Kazushige Ichikawa, Kuniyasu Okudaira, Toshiaki Taoka, Hirokazu Kawaguchi, Katsutoshi Murata, Katsuya Maruyama, **Gregor Körzdörfer**, Josef Pfeuffer, Mathias Nittka, and Shinji Naganawa. Comprehensive Evaluation of B_1^+-corrected FISP-based Magnetic Resonance Fingerprinting: Accuracy, Repeatability and Reproducibility of T_1 and T_2 Relaxation Times for ISMRM/NIST System Phantom and Volunteers. *Magnetic Resonance in Medical Sciences*, advpub, 2019

Conference Publications

- **Körzdörfer, G.**, T. Feiweier, Y. Jiang, and M. Nittka. B1-Sensitive Encoding for Magnetic Resonance Fingerprinting. In *Proceedings of the 24th Annual Meeting of ISMRM*, page 3191, Singapore,Singapore, 2016

- **Körzdörfer, G.**, M. Griswold, D. Ma, Y. Jiang, J. Pfeuffer, T. Feiweier, T. Kluge, and M. Nittka. Contrast and Resolution Mixing for Magnetic Resonance Fingerprinting. In *Proceedings of the 25th Annual Meeting of ISMRM*, page 1404, Hawaii,USA, 2017

- **Körzdörfer, G.**, T. Kluge, M. Pfeuffer, J. Gebhardt, D. Ma, Y. Jiang, M. Griswold, and M. Nittka. Spatial Biases in Magnetic Resonance Fingerprinting Parameter Maps Arising from Undersampling Patterns. In *Proceedings of the 25th Annual Meeting of ISMRM*, page 3956, Hawaii,USA, 2017

- **Körzdörfer, G.**, B. Guzek, Y. Jiang, J. Pfeuffer, B. Hensel, P. Speier, and M. Nittka. Description of the off-resonance dependency in slice-selective FISP MRF. In *Proceedings of the 26th Annual Meeting of ISMRM*, page 4232, Paris,France, 2018

- **Körzdörfer, G.**, P. Speier, S. Schröter, M. Schramm, J. Pfeuffer, B. Hensel, and M. Nittka. Evaluating the influence of motion on FISP-MRF. In *Proceedings of the 26th Annual Meeting of ISMRM*, page 4085, Paris,France, 2018

- **Körzdörfer, G.**, Y. Jiang, P. Speier, J. Pfeuffer, D. Ma, B. Guzek, B. Hensel, V. Gulani, M. Griswold, and M. Nittka. Magnetic Field Fingerprinting (MFF). In *Proceedings of the 26th Annual Meeting of ISMRM*, page 1018, Paris,France, 2018

- **Körzdörfer, G.**, R. Kirsch, K. Liu, J. Pfeuffer, B. Hensel, Y. Jiang, D. Ma, M. Griswold, V. Gulani, and M. Nittka. Multicenter and multiscanner reproducibility of Magnetic Resonance Fingerprinting relaxometry in the brain. In *Proceedings of the 26th Annual Meeting of ISMRM*, page 0798, Paris,France, 2018

- **Körzdörfer, G.**, M. Bacher, T. Kluge, R. Kroeker, D. Paul, J. Pfeuffer, B. Hensel, and M. Nittka. Prospective motion correction for 2D slice-selective FISP-MRF in the brain using an in-bore camera system. In *Proceedings of the 27th Annual Meeting of ISMRM*, page 4437, Montreal,Canada, 2019

- **Körzdörfer, G.**, D. Ma, J. Pfeuffer, B. Hensel, M. Griswold, and M. Nittka. Robust B1+ sensitive FISP Magnetic Resonance Fingerprinting in Brain and Abdomen. In *ESMRMB Congress 2017 34th Annual Scientific Meeting*, page 483, Barcelona,Spain, 2017

- **Körzdörfer, G.**, D. Ma, J. Pfeuffer, B. Hensel, M. Griswold, and M. Nittka. Robust B1+ sensitive FISP Magnetic Resonance Fingerprinting in Brain and Abdomen. In *ISMRM Workshop on Magnetic Resonance Fingerprinting*, Cleveland,USA, 2017

- **Körzdörfer, G.**, R. Kirsch, and M. Nittka. Cross-scanner reproducibility results on brain MRF . In *ISMRM Workshop on Magnetic Resonance Fingerprinting*, Cleveland,USA, 2017

- J. Pfeuffer, A. Kechagias, C. Meyer, **Körzdörfer, G.**, and M. Nittka. Mitigation of Spiral Undersampling Artifacts in Magnetic Resonance Fingerprinting (MRF) by Adapted Interleave Reordering. In *Proceedings of the 25th Annual Meeting of ISMRM*, page 0133, Hawaii,USA, 2017

- M. Berzl, A. Pfeil, C. Meyer, A. Campbell-Washburn, **Körzdörfer, G.**, M. Nittka, A. Maier, and J. Pfeuffer. Improved Spiral Trajectory Correction Using the Gradient Impulse Response Function (GIRF) with Application to MR Fingerprinting. In *Proceedings of the 25th Annual Meeting of ISMRM*, page 0933, Hawaii,USA, 2017

- J. Grinstead, **Körzdörfer, G.**, G. Laub, W. Rooney, and M. Nittka. An Image Simulation Tool for 3D TSE Including Flow Effects. In *Proceedings of the 25th Annual Meeting of ISMRM*, page 3956, Hawaii,USA, 2017

- L. Umutlu, J. Jaeger, M. Nittka, S. Kannengieer, J. Pfeuffer, **Körzdörfer, G.**, R. Kirsch, F. Meise, H. Quick, V. Gulani, M. Griswold, K. Herrmann, M. Gratz, and M. Forsting. Multi-Parametric 11C-Methionine-PET/MRI for Brain Tumor Imaging Utilizing MR Fingerprinting. In *Proceedings of the 25th Annual Meeting of ISMRM*, page 3587, Hawaii,USA, 2017

- M. Gratz, J. Jaeger, M. Nittka, S. Kannengieer, J. Pfeuffer, **Körzdörfer, G.**, R. Kirsch, F. Meise, H. Quick, V. Gulani, M. Griswold, M. Forsting, and L. Umutlu. From phantoms to patients: Paving the way for MRF in clinical practice. In *Proceedings of the 26th Annual Meeting of ISMRM*, page 4250, Paris,France, 2018

- E. Hoppe, **Körzdörfer, G.**, M. Nittka, and J Pfeuffer. Deep Learning for Magnetic Resonance Fingerprinting: Accelerating the Reconstruction of Quantitative Relaxation Maps. In *Proceedings of the 26th Annual Meeting of ISMRM*, page 2791, Paris,France, 2018

- S. Hodono, Y. Jiang, **Körzdörfer, G.**, N. Nallapareddy, V. Gulani, and M. Griswold. Matching Error Evaluation in Magnetic Resonance Fingerprinting with a Fast Imaging with Steady Precession sequence using Bloch Equation Simulations with a Diffusion Propagator. In *Proceedings of the 26th Annual Meeting of ISMRM*, page 2891, Paris,France, 2018

- M. Gratz, J. Jaeger, M. Nittka, S. Kannengieer, J. Pfeuffer, **Körzdörfer, G.**, R. Kirsch, F. Meise, H. Quick, V. Gulani, M. Griswold, M. Forsting, and L. Umutlu. From phantoms to patients: Paving the way for MRF in clinical practice. In *Proceedings of the 26th Annual Meeting of ISMRM*, page 4250, Paris,France, 2018

- Y. Jiang, K. Wright, J. Hamilton, W.-C. Lo, A. Panda, **Körzdörfer, G.**, S. Hodono, M. Boss, N. Seiberlich, V. Gulani, and M. Griswold. Rapid and Simultaneous T1, T2 and Diffusion Quantification using MR Fingerprinting in the Breast. In *Proceedings of the 26th Annual Meeting of ISMRM*, page 4250, Paris,France, 2018

- Y. Kato, K. Ichikawa, T. Taoka, H. Kawaguchi, K. Murata, K. Maruyama, **Koerzdoerfer, G.**, J. Pfeuffer, M. Nittka, and S. Naganawa. The impact of shorter acquisition time in MRF: Long term repeatability and reproducibility study on ISMRM/NIST phantom and volunteers. In *Proceedings of the 27th Annual Meeting of ISMRM*, page 4451, Montreal,Canada, 2019

- E. Hoppe, J. Wetzl, C. Forman, **Körzdörfer, G.**, M. Schneider, P. Speier, M. Schmidt, and A. Maier. Free-Breathing, Self-Navigated and Dynamic 3-D Multi-Contrast Cardiac CINE Imaging Using Cartesian Sampling and Compressed Sensing. In *Proceedings of the 27th Annual Meeting of ISMRM*, page 2129, Montreal,Canada, 2019

- Y. Jiang, **Körzdörfer, G.**, J. Hamilton, B. Zhao, L. Wald, V. Seiberlich, N. abd Gulani, M. Nittka, and M. Griswold. Fast 3D MR Fingerprinting with Pseudorandom Cartesian Sampling. In *Proceedings of the 27th Annual Meeting of ISMRM*, page 1108, Montreal,Canada, 2019

- K. Okudaira, Y. Kato, K. Ichikawa, T. Taoka, H. Kawaguchi, K. Murata, K. Maruyama, **Koerzdoerfer, G.**, J. Pfeuffer, M. Nittka, and S. Naganawa. Reproducibility of T1 and T2 relaxation times measured by magnetic resonance fingerprinting (MRF): ISMRM/NIST MRI System phantom study. In *The 46th Annual Meeting of the Japanese Society for Magnetic Resonance in Medicine*, page 042, Kanazawa,Japan, 2018

- K. Okudaira, Y. Kato, K. Ichikawa, T. Taoka, H. Kawaguchi, K. Murata, K. Maruyama, **Koerzdoerfer, G.**, J. Pfeuffer, M. Nittka, and S. Naganawa. Reproducibility of T1 and T2 relaxation times measured by magnetic resonance fingerprinting (MRF): a volunteer study. In *The 46th Annual Meeting of the Japanese Society for Magnetic Resonance in Medicine*, page 043, Kanazawa,Japan, 2018

- T. Taoka, H. Kawai, T. Nakane, H. Kawaguchi, K. Maruyama, K. Murata, **Koerzdoerfer, G.**, J. Pfeuffer, M. Nittka, and S. Naganawa. Tissue correlation time mapping by MR fingerprinting: Evaluation in normal brain. In *The 46th Annual Meeting of the Japanese Society for Magnetic Resonance in Medicine*, page 044, Kanazawa,Japan, 2018

- T. Okada, K. Fujimoto, Y. Fushimi, A. Yamaoto, A. Yamaoto, S. Nakajima, **Koerzdoerfer, G.**, J. Pfeuffer, M. Nittka, T. Isa, and K. Togashi. Preliminary results on precision of MR fingerprinting (MRF) measurements: A comparative study of 32-channel and 20-channel receive array coils. In *The 46th Annual Meeting of the Japanese Society for Magnetic Resonance in Medicine*, page 136, Kanazawa,Japan, 2018

- K. Ichikawa, Y. Kato, K. Okudaira, T. Taoka, K. Murata, K. Maruyama, **Koerzdoerfer, G.**, J. Pfeuffer, M. Nittka, and S. Naganawa. Accuracy of T1 and T2 relaxation times measured by magnetic resonance fingerprinting(MRF): ISMRM/NIST MRI System phantom study. In *The 46th An-*

nual Meeting of the Japanese Society for Magnetic Resonance in Medicine, page 041, Kanazawa,Japan, 2018

- Elisabeth Hoppe, **Körzdörfer, Gregor**, Mathias Nittka, Tobias Wür, Jens Wetzl, Felix Lugauer, and Manuel Schneider. Deep Learning for Magnetic Resonance Fingerprinting: Accelerating the Reconstruction of Quantitative Relaxation Maps. In *German Medical Data Sciences: Visions and Bridges (62. Jahrestagung der GMDS)*, pages 202–206, Oldenburg,Germany, 2017

- Elisabeth Hoppe, Florian Thamm, **Körzdörfer, Gregor**, Christopher Syben, Franziska Schirrmacher, Mathias Nittka, Josef Pfeuffer, Heiko Meyer, and Andreas Maier. RinQ Fingerprinting: Recurrence-informed Quantile Networks for Magnetic Resonance Fingerprinting. *arXiv e-prints*, page arXiv:1907.05277, July 2019

Patents

- **Körzdörfer, G.**, T. Feiweier, and M. Nittka. MRF with improved B1 encoding. US patent no. 15/211,313 filed, US patent no. 2018/0017646 published on 18.01.2018

- **Körzdörfer, G.**, T. Kluge, and M. Nittka. Analyse und Optimierung von Abtastschemata für MR-Fingerprinting. US patent no. 15/699,935 and EP patent no. 17165569.9 filed, US patent no. 2018/0074145 published on 15.03.2018 and EP patent no. published on 21.03.2018

- **Körzdörfer, G.**, J. Pfeuffer, and M. Nittka. MR Fingerprinting Verfahren mit integriertem Spiral-Deblurring. DE patent no. 10 2018 209 584.1 filed

- **Körzdörfer, G.** and M. Nittka. Erzeugung quantitativer Suszeptibilitätskarten mit MR Fingerprinting. CN patent no. 201910265076.X and EP patent no. 18166126.5 and US patent no. 16/376,180 filed

- **Körzdörfer, G.**, P. Speier, J. Pang, and M. Nittka. MR Fingerprinting mit Dictionary Rekompression. US patent no. 62/675,893 filed

- **Körzdörfer, G.**, P. Speier, J. Wetzl, and M. Nittka. MRF schnelles Dictionary Matching durch Kombination mehrerer Elemente. EP patent no. 18197267.0 filed

- **Körzdörfer, G.**, P. Speier, T. Kluge, and M. Nittka. MR Fingerprinting with reduced Off-resonance sensitivity. EP patent no. 18174359.2 filed

- **Körzdörfer, G.**, M. Griswold, P. Speier, Y. Jiang, and M. Nittka. MR Fingerprinting Verfahren zur gleichzeitigen Bestimmung von T1, T2, B1 und B0. US patent no. 62/653,737 filed

- **Körzdörfer, G.**, P. Speier, J. Pang, and M. Nittka. Simultaner Match von Phasendispersion und T2. US patent no. 62/688,013 filed

- **Körzdörfer, G.**, P. Speier, and M. Nittka. Vorteilhafte Ausgestaltung von MRF bei niedrigen Feldstärken. EP patent no. 18197190.4 filed
- **Körzdörfer, G.** and M. Nittka. Bewegungsdetektion für Magnetic Resonance Fingerprinting. EP patent no. 19167028.0 filed
- **Körzdörfer, G.** and M. Nittka. Prospektive Bewegungskorrektur für Magnetic Resonance Fingerprinting. EP patent no. 19167020.7 filed
- M. Nittka, P. Speier, S. Kannengießer, T. Kluge, **Körzdörfer, G.**, and J. Pfeuffer. 2D-MRF-Implementierung. DE patent no. 10 2019 206 827.8 filed